Development and application of computational methods for the investigation of the structures of metal nanoparticles

Cesare Roncaglia

Supervisor: Prof. R. Ferrando

Physics Department
University of Genoa

Ph.D. in Physics and Nanosciences - curriculum Physics
XXXVI Cycle

List of publications

1. Diana Nelli, Cesare Roncaglia, Riccardo Ferrando, and Chloé Minnai, *The Journal of Physical Chemistry Letters*, 2021, *12* (19), 4609-4615.
   DOI: 10.1021/acs.jpclett.1c00787

2. Cesare Roncaglia, Daniele Rapetti and Riccardo Ferrando, *Physical Chemistry Chemical Physics*, 2021, *23* (40), 23325-23335.
   DOI: 10.1039/d1cp02143e

3. Diana Nelli, Cesare Roncaglia, Samuel Ahearn, Marcel di Vece, Riccardo Ferrando and Chloé Minnai, *Catalysts*, 2021, *11* (6), 718.
   DOI: 10.3390/catal11060718

4. Diana Nelli, Cesare Roncaglia and Chloé Minnai, *Advances in Physics: X*, 2023, *8* (1), 2127330.
   DOI: 10.1080/23746149.2022.2127330

5. El yakout El koraychy, Cesare Roncaglia, Diana Nelli, Manuella Cerbelaud and Riccardo Ferrando, *Nanoscale Horizons*, 2022, *7* (8), 883-889.
   DOI: 10.1039/d1nh00599e

6. El yakout El koraychy, Diana Nelli, Cesare Roncaglia, Chloé Minnai and Riccardo Ferrando, *European Physical Journal Applied Physics*, 2022, *97* (28).
   DOI: 10.1051/epjap/2022210297

7. Cesare Roncaglia, *European Physical Journal Applied Physics*, 2022, *97* (11).
   DOI: 10.1051/epjap/2022210262

8. Cesare Roncaglia and Riccardo Ferrando, *Journal of Chemical Information and Modeling*, 2023, *63* (2), 459-473.
   DOI: 10.1021/acs.jcim.2c01203

9. Cesare Roncaglia, Swathi Swaminathan, Riccardo Farris and El yakout El koraychy, *Chemical Communications*, 2023, *59*, 3331-3338.
DOI: 10.1039/d3cc90068a

10. Damien Alloyeau et al., *Faraday Discussions*, 2023, *242*, 106-128.
DOI: 10.1039/d2fd90085h

11. Christine M. Aikens et al., *Faraday Discussions*, 2023, *242*, 389-417.
DOI: 10.1039/d2fd90087d

12. Daniele Rapetti, Cesare Roncaglia and Riccardo Ferrando, *Advanced Theory and Simulations*, 2023, *6* (9), 2300268.
DOI: 10.1002/adts.202300268

13. Manoj Settem, Cesare Roncaglia, Riccardo Ferrando and Alberto Giacomello, *The Journal of Chemical Physics*, 2023, *159* (9), 094303.
DOI: 10.1063/5.0159257

14. Malcolm Dearg, Cesare Roncaglia, Diana Nelli, El yakout El koraychy, Riccardo Ferrando, Thomas J. A. Slater and Richard E. Palmer, *Nanoscale Horizons*, 2024, *9*, 143-147.
DOI: 10.1039/d3nh00291h

15. Diana Nelli, Cesare Roncaglia, Riccardo Ferrando, Zeinab Kataya, Yves Garreau, Alessandro Coati, Caroline Andreazza-Vignolle and Pascal Andreazza, *Nanoscale*, 2023, *15*, 18891-18900.
DOI: 10.1039/D3NR04530G

16. Cesare Roncaglia and Riccardo Ferrando, *The Journal of Physical Chemistry A*, 2024, *128* (1), 89-96.
DOI: 10.1021/acs.jpca.3c06033

Table of contents

Introduction

Nanoparticles (NPs) are aggregates of atoms. The number of atoms contained in a nanoparticle may vary from a few atoms to a million atoms, and so the size of a nanoparticle, which spans the range $1 \sim 100$ nm [1, 2]. Single-element nanoparticles are known as pure or elemental nanoparticles, whereas bi- or multicomponents nanoparticles are known as nanoalloys [3].

Metallic nanoparticles can be produced in different experimental settings and environments, depending on the specific needs. When a low contamination is needed during production, synthesis in the gas phase is preferred. This kind of synthesis guarantees a high level of purity in the production of nanoparticles, at the price of a generally low amount of output. Gas-phase synthesis is typically done under vacuum conditions in a few steps. First, in the vaporization stage, a solid metal target is heated or bombed to produce a metallic vapour. Then, during nucleation stage, the vapour is cooled down by a inert gas flux (usually helium or argon) so that atoms can aggregate in small nuclei, since re-evaporation is now less favourable. Finally these metallic nuclei can grow by the addition of further atoms or small aggregates. In a later stage, large aggregates may also collide with each other and coalesce to form even larger units. There are several types of sources for gas-phase growth. A well known example is the magnetron sputtering source, for which a schematic representation is given in Fig. I1. Inert gas ions (typically Ar^+) are accelerated and fired against the target material (for example a metal or a mixture of metals), which sputters single atoms and small aggregates. These products are then cooled down by a inert gas flow to start nucleation and growth; when aggregation is in process the nanoparticles are drifted away from the target by a pressure difference. Subsequently, a mass filter may select only certain nanoparticles. Finally these selected nanoparticles enter the deposition chamber, which is allowed to rotate to achieve a more homogeneous deposition on the substrate.

On the other hand, when a more abundant production of nanoparticles is needed, synthesis in the liquid phase is preferred. In this case, metallic nanoparticles are in many cases let to aggregate in an aqueous solution. In liquid-phase synthesis, the price to pay for having a high yield is given by the unavoidable contamination from the other molecules participating to the

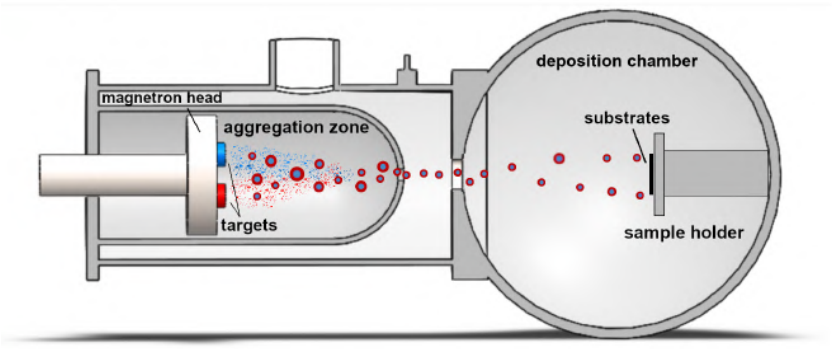

Fig. I1 Schematic representation of bimetallic nanoalloys synthesis by magnetron sputtering. Reprinted with permission from [4]. Copyright 2020 American Chemical Society.

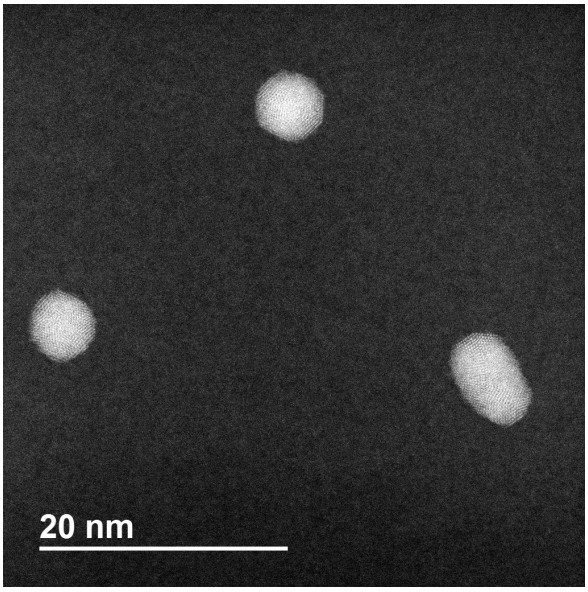

Fig. I2 STEM image of AuPd nanoparticles. Courtesy of Dr. Chloé Minnai.

synthesis - the use of which is very often necessary to protect the produced nanoparticles from massive agglomeration and coalescence.

Once produced, either in the gas or the liquid phase, the structural properties of nanoparticles must be characterized. Electron microscopy is the most widely used technique for this purpose. In particular, TEM (Transmission Electron Microscopy) and STEM (Scanning TEM) are used most frequently. Recently, also grazing incidence X-ray diffraction has been used to analyze growing nanoparticles on substrates [5]. An example of a STEM image of some AuPd nanoparticles is give in Fig. I2.

Nanoparticles exhibit physical and chemical properties that considerably differ from those of the bulk metals. For this reason, they are gaining increasing importance in a

significant number of different scientific areas for their many applications. These applications include for example catalysis, data storage, plasmonics, nanomedicine, water purification and many others. Consequently, nanoparticles have been extensively studied in recent years. Very often, the determination of the properties of nanoparticles has been possible thanks to a combined experimental-theoretical investigation (see for example Refs. [6–9]). Therefore, the theoretical study of metal nanoparticles is of utter importance. In fact, laying the basis for the understanding of these nanoscale systems is a fundamental step towards the comprehension and interpretation of experimental observations as well as the design of new ones. However, these finite nano-sized systems are very difficult to model by means of analytical techniques only, since the explicit solution of the quantum problem of a system of many atoms is a very difficult - if not impossible - task. As a consequence, considerable effort has been put in the development of numerical techniques aimed at overcoming this obstacle. As we shall see in a following chapter, these techniques - that may take into account either explicitly or implicitly the quantum nature of the system - allow to study at atomic level the structure and temporal evolution of metal nanoparticles, a very powerful feature that is at present quite limited in experimental techniques. On the other hand, due to computational costs, numerical simulations cannot often achieve such large sizes and/or long time scales as those of experiments. As a result, only the cooperation between theoretical and experimental analysis is a winning strategy for the successful exploitation of nanoparticles properties.

This Ph.D. thesis is dedicated to the development and application of computational techniques for the study of metallic and bi-metallic nanoparticles.

The first methodological development treated in this thesis regards the analysis of nanoparticles structures and their partition into groups sharing specific features. Very often, as we shall see in later chapters, many NPs structures are produced in the output of different numerical simulations. At the beginning of this project, the state of the art of this field was actually missing a method for a meaningful and automatic partition of these outputs. In the post-processing stage of the analysis of these numerical simulations, the application of other algorithms may require such subdivision of the output into different groups of structures that share some features. One of the main motivation behind this work was to fill this gap. The results obtained for the development of a technique specifically designed for this purpose are reported in Chapter 3, in which a more detailed discussion about the need of such procedure and its benefits is given.

Another development of a computational technique which is discussed in this thesis is about the problem of global optimization. This problem, which is well known for its numerous applications, has also found very soon its use in the field of metal nanoparticles. In fact, as it will be described more in detail in Chapters 2 and 4, the search of the lowest-energy

structures for a given fixed number of atoms of some metal (or metals) is a very important topic, because it determines in principle what could be the most probable structures found in experiments that produce nanoparticles at low-temperature thermodynamic equilibrium. In Chapter 4, two new algorithms for the global optimization of single and multi-metallic nanoparticles are presented; it is shown in particular that these algorithms preform better than those already present in the existing literature.

Applications of computational methods are treated in Chapters 5 and 6.

In Chapter 5, we demonstrate that a specific geometrical structure of tetrahedral symmetry, which is generally unusual for pure metal NPs, becomes more stable thanks to the alloying of two metals. These tetrahedral clusters correspond to a new series of magic numbers. The specific nanoalloy system considered here is PtPd.

In Chapter 6, the results of a collaboration with the experimental group of Prof. Andreazza at the University of Orléans, France, about the study of the growth of silver nanoparticles are discussed. The growth of these clusters is within the icosahedral motifs, but the growth mechanisms revealed by our simulations are quite complex.

The remaining parts of this thesis are organized as follows. In Chapter 1 a general description of the geometrical and chemical features of metal nanoparticles and nanoalloys is given. In Chapter 2 the computational models and methods used in this thesis are described. A summary of all results of the thesis is given in the last chapter, where we also draw the conclusions. The results presented in Chapter 3 are based on papers 2 and 8 given in the List of publications. Chapter 4 is based on the content of paper 12 in the same list, whereas for Chapters 5 and 6 the material of papers 16 and 15 respectively, was used.

Chapter 1

Geometric structures and chemical ordering of nanoparticles and nanoalloys

Nanoparticles can occur in a large variety of different shapes. For this reason, these systems have found many applications in different fields. It has been shown, in fact, that numerous physical and chemical properties of metal nanoparticles strongly depend on their geometric structures. For example, we recall optical and catalytic properties [10–12], that may be tuned by properly selecting the shape of NPs, a procedure which is possible with present experimental setups. In the case of bi- or multi-metallic nanoalloys, the various possible arrangements of atoms of different chemical species increases even more the number of available structures. The pattern in which all different elements are arranged is known as *chemical ordering*. In this chapter we will describe the most common geometric structures and chemical orderings that appear in nanoparticles and nanoalloys, as well as other less common that are relevant for the discussion of the thesis. A more exhaustive discussion can be found in Refs. [3, 13, 14].

1.1 Geometric structures

All geometric structures of nanoalloys can be divided in two large classes: *crystalline* and *noncrystalline* structures. The first class includes structures that can be derived as fragments of the bulk crystal, such as face-centered cubic (fcc), body-centered cubic (bcc) and hexagonal close-packed (hcp). For these geometrical shapes, we expect interatomic distances in the NP to be similar to those in the bulk. The second class includes structures that cannot be derived as fragments of any crystal lattice. Such possibility in finite systems is due to the absence of translational invariance needed instead for an infinite periodic crystal lattice.

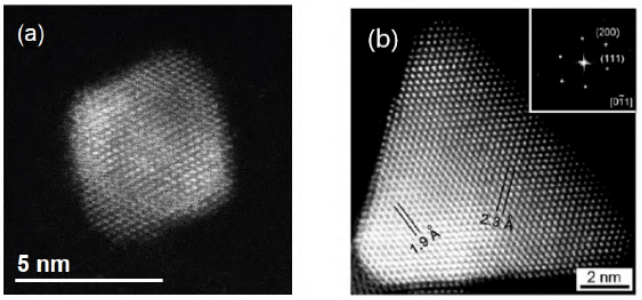

Fig. 1.1 (a) PdPt octahedral nanoparticle, courtesy of Dr. Chloé Minnai. (b) HAADF-STEM image of a Pd truncated tetrahedron. Adapted with permission from [15]. Copyright 2013 American Chemical Society.

1.1.1 Crystalline structures

In the following discussion we examine only nanoparticles crystalline structures that can be obtained from the fcc lattice, since all the metals considered in this thesis possess this symmetry in their bulk structure. The two most commonly known regular structures that can be obtained directly from the fcc stacking are the regular tetrahedron and the regular octahedron. Nanoparticles showing these structures were obtained in several growth experiments. One example in given in Fig. 1.1. The regular tetrahedron (Th) has four facets that are equilateral triangles, six edges and four vertices. Let n be the number of atoms in each edge; the tetrahedron can be constructed by stacking equilateral triangles of decreasing edge length from the base to the vertex. Then, the total number of atoms N_{Th} in the regular tetrahedron can be computed to be:

$$N_{\mathrm{Th}} = \frac{1}{6}n(n+1)(n+2), \tag{1.1}$$

which gives the series of numbers: $N_{\mathrm{Th}} = 1,4,10,20,35,56,\ldots$ for $n = 1,2,3,4,5,6,\ldots$ and so on.

The regular octahedron (Oh) has 8 facets that are equilateral triangles, twelve edges and six vertices. It can be thought as two regular pyramids joined together, sharing a common square base. Hence, the number of atoms of a regular octahedron N_{Oh}, having n atoms in each edge is

$$N_{\mathrm{Oh}} = \frac{1}{3}(2n^3 + n), \tag{1.2}$$

which gives the series of numbers: $N_{\mathrm{Oh}} = 1,6,19,44,55,\ldots$ for $n = 1,2,3,4,5,\ldots$ and so on. The two regular shapes are shown in two views in Fig. 1.2.

Both regular tetrahedra and octahedra are cutted from the fcc lattice so that they expose only (111) facets - the ones having the lowest surface energy possible, at least for the metals

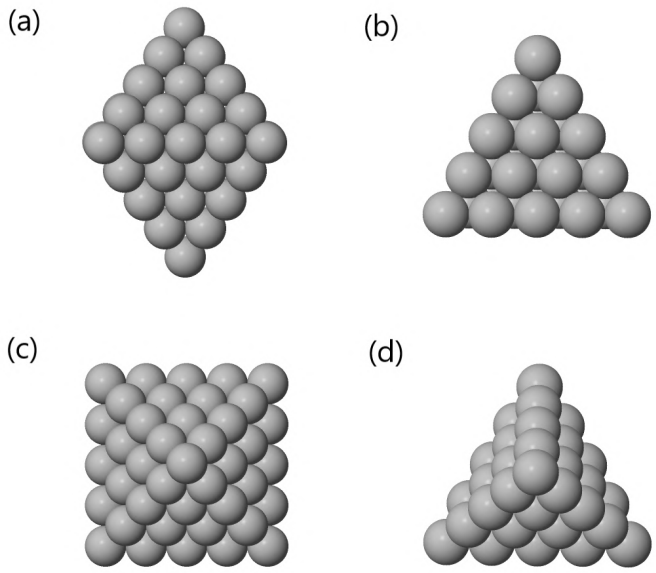

Fig. 1.2 (a) Side and (c) top view of a regular octahedron, (b) side and (d) top view of a regular tetrahedron. For both, $n = 5$.

considered in this thesis. However, due to the large surface-to-volume ratio, these structures cannot be expected to be favorable from an energetic point of view. An improvement can be obtained by making some truncations at the vertices, in order to create more compact structures. For example, a truncated octahedron is built by making truncations all over the six vertices. Such truncations create six (100) square facets, that have a higher surface energy than (111) - an energetic cost that is assisted by the lowering of the surface-to-volume ration. The deepness of the best truncation is usually the one for which the remaining (111) facets become regular hexagons. Let n_{cut} be the number of layers cutted at each vertex. The number of atoms of the truncated octahedron (TO) is therefore

$$N_{\mathrm{TO}} = \frac{1}{3}(2n^3 + n) - 2n_{cut}^3 - 3n_{cut}^2 - n_{cut}. \tag{1.3}$$

Regular truncated octahedron is obtained when $n_{cut} = (n-1)/3$. In this case, the number of atoms is:

$$N_{\mathrm{TO}}^{\mathrm{reg}} = \frac{1}{27}(16n^3 - 3n^2 + 12n + 2), \tag{1.4}$$

which gives the series of numbers: $N_{\mathrm{TO}}^{\mathrm{reg}} = 38, 201, 586, 1289, \ldots$ for $n = 4, 7, 10, 13, \ldots$ and so on. Some regular and irregular truncated octahedra are shown in Fig. 1.3 from two different views.

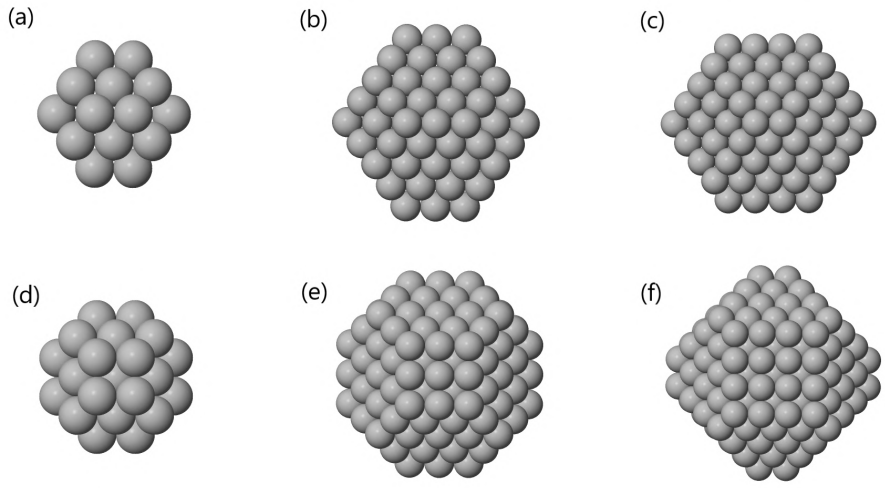

Fig. 1.3 (a) Side and (d) top view of a regular truncated octahedron with $N_{\mathrm{TO}}^{\mathrm{reg}} = 38$ atoms, (b) side and (e) top view of another regular truncated octahedron wit $N_{\mathrm{TO}}^{\mathrm{reg}} = 201$ atoms, (c) side and (f) top view for an irregular truncated octahedron with $N_{\mathrm{TO}} = 260$ atoms. For the first two structures, $n = 4$ and 7, and $n_{cut} = 1$ and 2, respectively. For the last one $n = 8$ and $n_{cut} = 3$.

1.1.2 Noncrystalline structures

Noncrystalline structures are geometrical shapes that must break the symmetry of the fcc lattice at some point inside the nanoparticle. Very often, such nanoparticles are composed of different fcc subunits joined together through some shared atomic planes. These planes, also known as *twin planes*, are the place where the symmetry of the lattice is broken. Usually, twin planes are also local mirror planes. The simplest case is that of a single twin plane, but nanoparticles structures having more than one, known as *multiply twinned* structures, are also possible. Two examples are shown in Fig. 1.4.

The most common multiply twinned nanoparticles are Decahedra (Dh) and Icosahedra (Ih), that can be constructed by joining five and twenty tetrahedral subunits, respectively. When tetrahedral subunits are organized to build these shapes, some interstices remain between them. In order to fill these gaps, tetrahedral subunits are distorted and, as a consequence, interatomic distances are non-ideal. Therefore, these structures are *strained* structures. Decahedra and Icosahedra are frequently found in experiments [16–18]. An example of AuPd nanoparticles observed by High-Angle Annular Dark-Field - Scanning Transmission Electron Microscope (HAADF-STEM) is shown in Fig. 1.5.

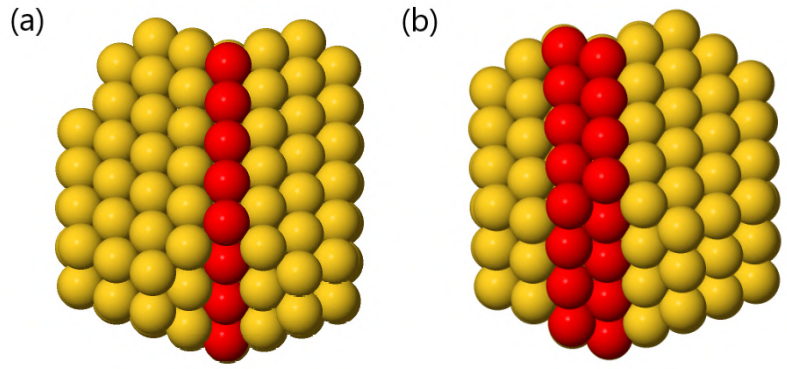

Fig. 1.4 (a) Au_{309} nanoparticle with a single twin plane and (b) Au_{294} nanoparticle with two consecutive twin planes, forming a local hcp zone. Twin planes are highlighted in red.

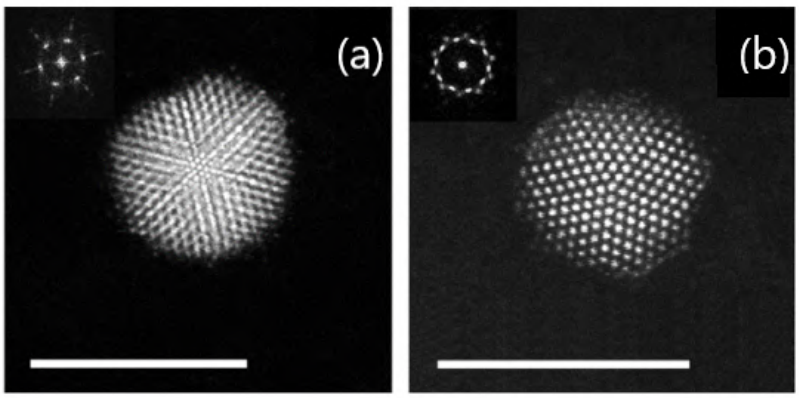

Fig. 1.5 HAADF-STEM images of AuPd noncrystalline nanoparticles. (a) Icosahedron and (b) decahedron. Scale bar 5 nm. Adapted with permission from [19]. Copyright 2021 American Chemical Society.

Regular decahedra are made of two pentagonal pyramids sharing their base, as can be seen in Fig. 1.6 (a). The five tetrahedra subunits have an edge in common, which is the central fivefold symmetry axis of the nanoparticle.

The regular decahedron has ten close-packed (111) triangular facets, ten edges and seven vertices. Again, due to the large surface-to-volume ratio, the structure can be improved and made more stable. A first proposal was made by Ino [20], in which the atoms of the perimeter of the common base are eliminated, such as in in Fig. 1.6 (b). The Ino decahedron has five (100) facets, that are less favorable in terms of surface energy but help in making the nanoparticle more spherical, as in the case of the truncated octahedron. A further improvement can be made by constructing the Marks decahedron [21], which can be obtained from the Ino decahedron by removing other atoms in order to create some re-entrances, as shown in Fig. 1.6 (c). A Marks decahedron can be identified by three integers (m,n,p), where m and n are the number of atoms of the (100) facets, perpendicular and parallel to the fivefold axis, respectively; p is the depth of the re-entrance, where $p = 1$ means no re-entrance, i.e. a regular or Ino decahedron. The number of atoms of a Marks decahedron described by (m,n,p) is:

$$\begin{aligned} N_{\text{Marks}} = & \frac{1}{6}(30p^3 - 135p^2 + 207 - 102) + \\ & + \frac{1}{6}\{5m^3 + (30p-45)m^2 + [60(p^2-3p) + 136]m\} + \\ & + \frac{1}{6}\{n[15m^2 + (60p-75)m + 3(10p^2-30p) + 66]\} - 1. \end{aligned} \tag{1.5}$$

The number of atoms for any Ino decahedron can be recovered simply putting $p = 1$. In that case:

$$N_{\text{Ino}} = \frac{1}{6}[5m^3 - 15m^2 + 16m + n(15m^2 - 15m + 6)] - 1. \tag{1.6}$$

Finally, the number of atoms of a regular decahedron is obtained when $n = 1$, that is when there are no (100) facets:

$$N_{\text{Dh}} = \frac{1}{6}(5m^3 + m). \tag{1.7}$$

The regular Mackay icosahedron [22] has twenty (111) triangular facets, thirty edges and twelve vertices. Each pair of opposite vertices lie on a fivefold axis. The twenty tetrahedral subunits forming a regular icosahedron share a vertex. A regular icosahedron is composed of concentric atomic shells. If the number of layers is k, the number of atoms of the relative icosahedral structure is given by

$$N = \frac{1}{3}(10k^3 - 15k^2 + 11k - 3), \tag{1.8}$$

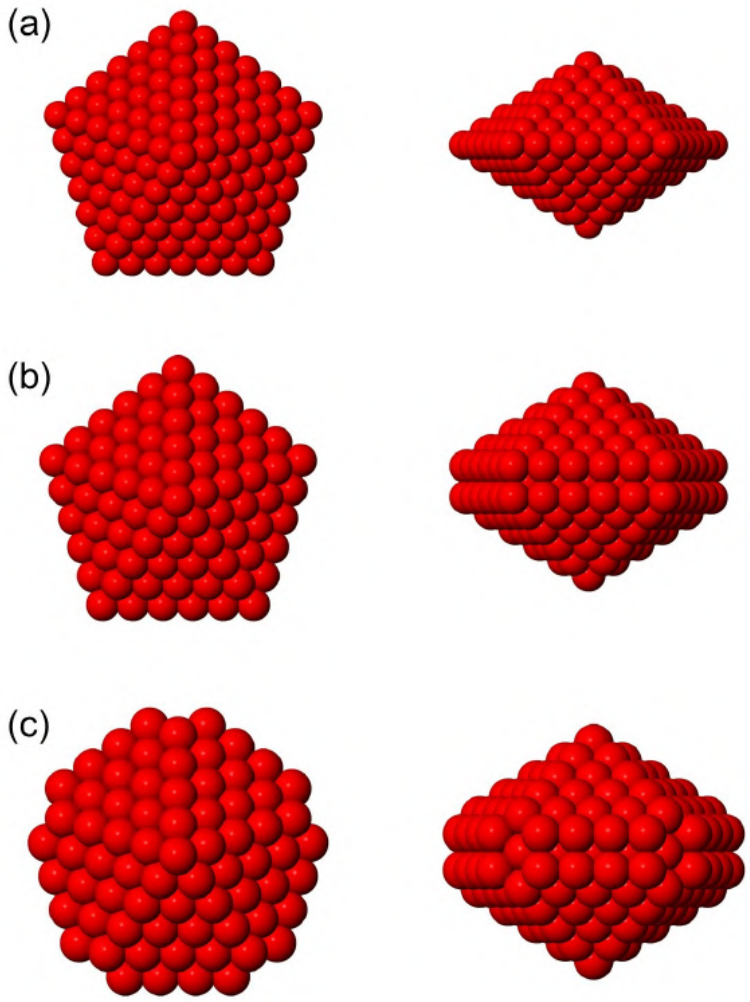

Fig. 1.6 Different types of decahedral structures in two different views. (a) Regular decahedron with $(m,n,p) = (7,1,1)$ containing 287 atoms, (b) Ino decahedron with $(m,n,p) = (6,2,1)$ containing 257 atoms, i.e. by removing 30 atoms of the perimeter of the base from the structure in (a) and (c) Marks decahedron with $(m,n,p) = (4,2,2)$ containing 247 atoms, i.e. by removing 10 atoms more from the structure in (b) to create re-entrances.

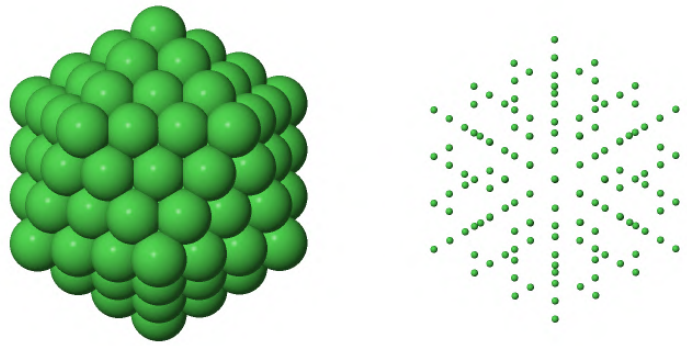

Fig. 1.7 Mackay Icosahedron with $k = 4$ atomic layers and 147 atoms.

which gives the series of numbers 1, 13, 55, 147, 309, ... for $k = 1,2,3,4,5,...$ and so on. An example of icosahedral structure is shown in Fig. 1.7. The Mackay regular icosahedron is already a spherical structure and does not need truncations to be improved. However, there exist some variation of the icosahedral theme that are worth to be discussed, for their particular symmetric patterns. In the anti-Mackay icosahedron [23], atoms of the surface occupy hcp-like sites on the underlying layer rather than fcc-like sites as in the regular Mackay icosahedron. An example is shown in Fig. 1.8 (b). Another variation is the chiral icosahedron, that can be obtained by applying a chiral distortion to the surface of the anti-Mackay icosahedron, as shown in Fig. 1.8 (c). In anti-Mackay and chiral icosahedra, surface atoms are less-densely packed than in Mackay icosahedron. Therefore, these structures are typically less favorable than the regular ones, with the exeption of some bi-metallic systems [24]. Nevertheless, some surface reconstruction of the Mackay icosahedron that are favorable do exist. A notable example is that of *rosettes* [25]. In this reconstruction pattern, a vertex atom enters the cluster surface and forms a hexagonal ring together with its former five surface neighbours. Multiple rosette reconstructions may be present, as shown in Fig. 1.9. It was found that for some Au and Pt nanoparticles, this kind of reconstruction is energetically favorable [25].

1.2 Chemical ordering

Chemical ordering is the way in which atoms of different species take place inside a nanoalloy. In general, chemical orderings can be divided in two main classes: *mixing patterns* and *nonmixing* or *phase-separated* patterns, that are also the most common arrangements found in NPs. Some systems, nonetheless, exhibit unusual behaviours that assume both chemical

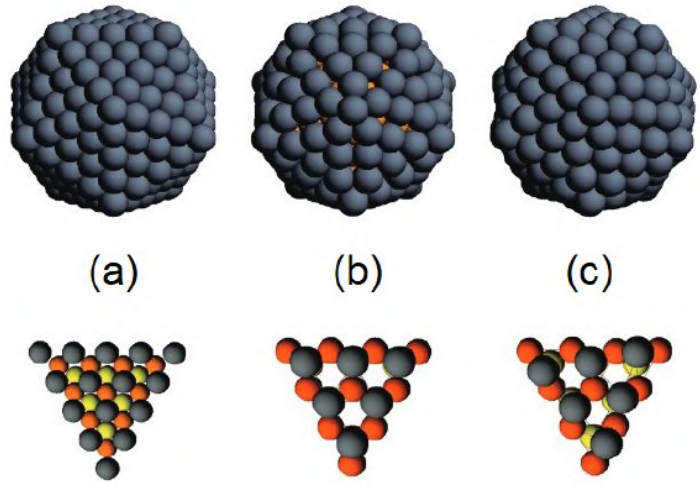

Fig. 1.8 (a) Mackay (b) anti-Mackay and (c) chiral icosahedra. For each structure, the surface (top row) and the stacking of the three outer surface layers (bottom row) are shown. Reprinted with permission from [24]. Copyright 2010 American Chemical Society.

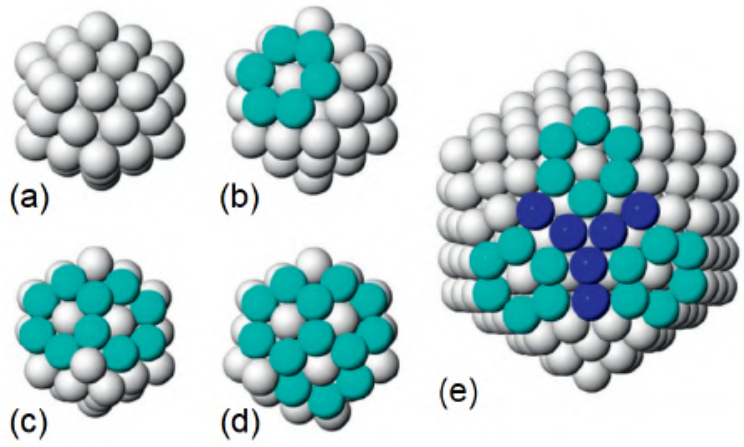

Fig. 1.9 Rosette reconstruction on the surface of icosahedral structures. Icosahedron of 55 atoms with (a) no rosettes, (b) one rosette, (c) two rosettes and (d) three rosettes. (e) Icosahedron of 309 atoms with three rosettes. Hexagonal rings are highlighted in cyan, whereas in (d) further edge atoms in the reconstructed region are highlighted in blue. Reproduced from [13]. Copyright Elsevier 2016.

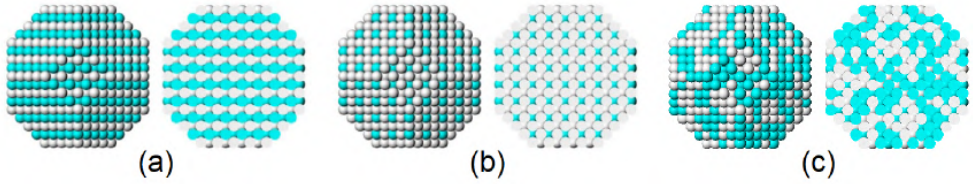

Fig. 1.10 Mixing patterns in crystalline bimetallic nanoparticles. Two different colours (grey and cyan) are used to highlight atoms of the two different species. In all cases both the nanoparticle surface (left) and a cross-section (right) are shown. (a) $L1_0$ phase at 1:1 composition, with alternating (100) atomic planes of the two elements. (b) $L1_2$ phase at 3:1 composition; the two alternating (100) atomic planes are made of: (i) the most abundant element, and (ii) both elements arranged in a chessboard. (c) Randomly intermixed chemical ordering at 1:1 composition. Adapted from [13]. Copyright Elsevier 2016.

orderings in different parts of their structure. A notable example is that of AgPd, in which in the core of the NPs there is a mixed pattern, but a segregation of silver on the surface is observed [26]. Similar behaviours were observed for AgPt and CoPt nanoparticles [27, 28]. In mixed patterns, the two or more different chemical species occupy alternate positions. In a random mixing pattern, as shown in Fig. 1.10 (c), atoms form a solid solution. Ordered mixing patterns are possible. Some examples, typical of bulk ordered phases, are shown in Fig. 1.10 (a) and (b), for 1:1 and 1:3 compositions, respectively. In these patterns, atoms of different chemical species are arranged in alternate planes. The main driving force for mixing patterns is the tendency towards intermixing in the corresponding bulk system. However, other factors may play a role in the final chemical ordering of a nanoparticles, such as geometry constraints, surface energy and atomic size differences. Mixing patterns are observed, for example, in CoPt, FePt, AuCu, AuPd, AgPd and AgAu bimetallic nanoparticles.

In nonmixing patterns, the two or more metals segregate in different parts inside the nanoparticle. Several examples are displayed in Fig. 1.11. The most common is the *core-shell* arrangement, shown in Fig. 1.11 (a), in which the core of the nanoparticles is entirely made of atoms of type A and the outer shell of the nanoparticles is entirely made of atoms of type B. For NPs displaying such chemical ordering, the notation A@B is often used. Multi-shell arrangements are also possible, such as the three-shell A@B@A arrangement, shown in Fig. 1.11 (b). Core-shell arrangements can also be asymmetric or incomplete, as in Fig. 1.11 (c). In Janus NPs, Fig. 1.11 (d) the two elements are simply separated in opposite sides; in quasi-Janus arrangements, a similar arrangements occurs, with the only difference that the surface layer is entirely made of one of the two elements, as depicted in Fig. 1.11 (e). Phase-separated patterns are common in AgCu, AgNi, AuCo, AgCo and AuPt nanoalloys.

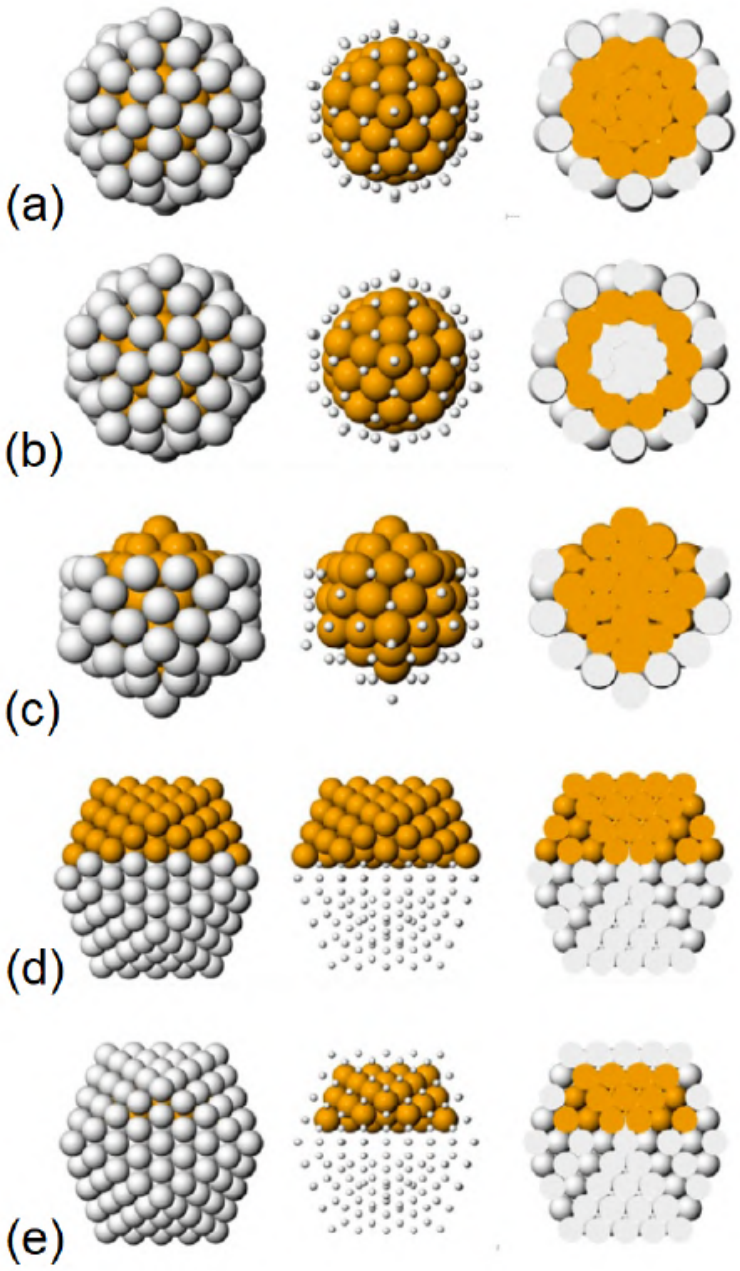

Fig. 1.11 Nonmixing patterns in bimetallic nanoparticles with icosahedral geometric structure. A and B atoms are shown in orange and grey, respectively. In all cases the nanoparticle is shown in three different views. Left column: nanoparticle surface. Middle column: B atoms are shown as small spheres. Right column: cross-section of the nanoparticle. (a) Core-shell A@B; (b) three-shell A@B@A; (c) core-shell A@B with incomplete B shell; (d) Janus; (e) quasi-Janus with B surface layer. Reproduced from [13]. Copyright Elsevier 2016.

Chapter 2

Theoretical models and computational techniques

The investigation of metal nanoparticles properties is usually made by a combination of theoretical and experimental methods. However, due to the intrinsically hard nature of the many-body quantum problem that should be solved in order to predict the chemical and physical properties of interest, these investigations are usually undertaken numerically, very often by means of computer simulations. In the last decades, numerical approaches have exploited their absolute importance. Nowadays, they represent a solid bridge between the experimental and theoretical communities, for their ability to examine such systems with atomic-level precision and at very short time scales that are not accessible at present by any experimental apparatus. Thus, computational methods are a fundamental tool not only to understand experimental findings in great detail, but also to suggest new experiments whose results have not yet been observed.

In this chapter, we will describe the three main methodologies that have been used throughout the thesis. The first kind of methods includes tools for efficiently explore the energy landscape of the system, i.e. its potential energy as a function of the atomic coordinates. In the examples treated in this thesis, which deals with nanoparticles containing a relatively large number of atoms, the energy landscape is described by an atomistic potential, in which electronic degrees of freedom do not appear explicitly bu are taken into account effectively. The methods of this type are Global Optimizations and Molecular Dynamics. The former is used to search for the lowest-energy geometric structure and chemical ordering. Such structures are of great importance since they represent the most stable structures - i.e. those at thermodynamic equilibrium - at low temperatures, a situation that is often met in experiment. The latter is instead adopted for studying the temporal evolution at constant temperature or constant energy, growth phenomena and coalescence.

The second type of methodology - Density Functional Theory (DFT) - is an *ab initio* approach, in which the potential energy of the system is calculated directly by solving numerically the quantum problem of a system of electrons in the external field of fixed nuclei. This method is usually more accurate than those that rely on approximated form of the potential energy, such as atomistic potentials, but on the other hand is much more computationally expensive. This approach is used especially in situations in which a great precision is needed to draw conclusions about some properties of a system, e.g. a particular nanoparticle's site adsorption energy.

Finally, the third kind of methods is related to Machine Learning algorithms, and specifically to *unsupervised* learning - the branch that deal with grouping data automatically. These methods are very powerful and they can be used, as we shall see in the next chapter, for separating nanoparticles structures into different groups that share some features. Global optimizations, Molecular Dynamics and Density Functional Theory have been widely used in the past to study nanoparticles and nanoalloys, whereas Machine Learning techniques related to this field have become popular only in the last years. Here we will describe generally all the above-mentioned methodologies and we will also describe some adaptations to apply these methods to the case of nanoparticles and nanoalloys.

2.1 Global Optimization and Molecular Dynamics: the need of an atomistic approach

The first class of methods deals with the exploration of the potential energy function – the energy landscape. In particular, let $\{\mathbf{R}\} = (\mathbf{R}_1, \mathbf{R}_2, ..., \mathbf{R}_N)$ be the set of coordinates of the N atoms of a nanoparticle or a nanoalloy. The potential energy that describe the system is a function $U(\{\mathbf{R}\})$ of all the atomic coordinates. In *atomistic* approaches, the potential energy function is given by analytical formulas or can be given as a numerical table. Electrons are not explicitly taken into account, rather their contribution to the overall interaction is buried beneath the force field form. In the following, we will describe an atomistic potential which can be derived as a second-moment approximation to the tight-binding model, and that is commonly referred to as SMATB potential, or Gupta potential or Rosato-Guillopé-Legrand (RGL) potential [29–31]. The derivation of the potential can be found in Refs. [32]. The exploration of the energy landscape by the methods described in the following can be in principle be made by ab-initio methods, such as DFT. However DFT is so computationally expensive that a thorought exploration of the landscape is feasible only for nanoparticles containing up to a few ten atoms.

2.1.1 Atomistic potential

In Gupta potential, the potential energy of a nanoparticle $U(\{\mathbf{R}\})$ is given as a sum of single atomic contribution E_i, each depending on the relative distances $r_{ij} = |\mathbf{R}_i - \mathbf{R}_j|$ between atom i and all other atoms j:

$$U(\{\mathbf{R}\}) = \sum_{i=1}^{N} E_i, \tag{2.1}$$

where

$$E_i = \sum_{j, r_{ij} \leq r^c_{\alpha\beta}} A_{\alpha\beta} \exp\left[-p_{\alpha\beta}\left(\frac{r_{ij}}{r^0_{\alpha\beta}} - 1\right)\right] - \sqrt{\sum_{j, r_{ij} \leq r^c_{\alpha\beta}} \xi^2_{\alpha\beta} \exp\left[-2q_{\alpha\beta}\left(\frac{r_{ij}}{r^0_{\alpha\beta}} - 1\right)\right]}. \tag{2.2}$$

The first term is a repulsive term, which is a sum of pair contributions, in the form of a Born-Mayer ion-ion repulsion; the second term is insted a many-body attractive term, which cannot be written as a sum of pair contributions. In this formula, α and β are the chemical species of atoms i and j respectively. The parameter $r^0_{\alpha\beta}$ is usually chosen as the equilibrium distance in the bulk crystal for the case $\alpha = \beta$ and as the average of the two equilibrium distances for the other case. The parameters $p_{\alpha\beta}, q_{\alpha\beta}, A_{\alpha\beta}$ and $\xi_{\alpha\beta}$ are fitted on some physical properties of the bulk metals and alloys [30, 31, 33, 34]. In the formula, for a given atom i, the sum of interactions is not extended to all the other atoms j, but only to those that are within a distance given by the cutoff $r^c_{\alpha\beta}$. The cutoff distance can be chosen for example as the second or third-neighbour distance in the bulk crystal. The cutoff distance is important for modeling crystals with periodic boundary conditions as well as to speed up calculations, however, it introduces discontinuities in the potential energy function, and so to its derivatives. In this thesis, we used an implementation of the Gupta potential that addresses this problem by adding a new cutoff distance $r^e_{\alpha\beta}$ and by imposing the continuity of the potential energy through a fifth-order polynomial that links it smoothly to zero from $r^c_{\alpha\beta}$ to $r^e_{\alpha\beta}$. The form of the polynomial is $p(r) = a_{3,\alpha\beta}(r - r^e_{\alpha\beta})^3 + a_{4,\alpha\beta}(r - r^e_{\alpha\beta})^4 + a_{5,\alpha\beta}(r - r^e_{\alpha\beta})^5$, where $a_{3,\alpha\beta}, a_{4,\alpha\beta}$ and $a_{5,\alpha\beta}$ are coefficients needed to match the potential energy function and its first and second derivatives in $r = r^c_{\alpha\beta}$.

Forces acting on each atom can be calculated as the gradient of the Gupta potential energy. By taking into consideration the polynomial link, the derivation gives the following result, for the force acting on the k-th atom:

$$\mathbf{F}_k = \sum_{i, r_{ik} \leq r^c_{\alpha\beta}} \mathbf{F}^{pot}_{ki} + \sum_{i, r^c_{\alpha\beta} < r_{ik} \leq r^e_{\alpha\beta}} \mathbf{F}^{pol}_{ki}, \tag{2.3}$$

where $\mathbf{F}_{ki}^{pot}$ is the the part of the force acting on the k-th atom due to the i-th atom, coming from the derivation of the Gupta potential, as given in eq. (2.2), and $\mathbf{F}_{ki}^{pot}$ the term derived from the polynomial link. The first term reads:

$$\begin{aligned}\mathbf{F}_{ki}^{pot} = \Bigg((D_k + D_i) q_{\alpha\beta} \xi_{\alpha\beta} \exp\left[-q_{\alpha\beta} \left(\frac{r_{ik}}{r^0_{\alpha\beta}} - 1 \right) \right] + \\ - 2 p_{\alpha\beta} A_{\alpha\beta} \exp\left[-p_{\alpha\beta} \left(\frac{r_{ik}}{r^0_{\alpha\beta}} - 1 \right) \right] \Bigg) \frac{1}{r^0_{\alpha\beta}} \frac{\mathbf{r}_{ik}}{r_{ik}},\end{aligned} \tag{2.4}$$

where

$$D_i = \frac{1}{\sqrt{\sum_{j, r_{ij} \leq r^c_{\alpha\beta}} \xi^2_{\alpha\beta} \exp\left[-2 q_{\alpha\beta} \left(\frac{r_{ij}}{r^0_{\alpha\beta}} - 1 \right) \right]}}. \tag{2.5}$$

The second one is:

$$\begin{aligned}\mathbf{F}_{ki}^{pol} = -\Big[(D_k + D_i)(a_{3,\alpha\beta} dr^3 + a_{4,\alpha\beta} dr^4 + a_{5,\alpha\beta} dr^5)(3a_{3,\alpha\beta} dr^2 + 4a_{4,\alpha\beta} dr^3 + 5a_{5,\alpha\beta} dr^4) + \\ - 2(3a_{3,\alpha\beta} dr^2 + 4a_{4,\alpha\beta} dr^3 + 5a_{5,\alpha\beta} dr^4) \Big] \frac{\mathbf{r}_{ik}}{r_{ik}},\end{aligned} \tag{2.6}$$

where $dr = r_{ik} - r^e_{\alpha\beta}$.

In the past years the SMATB potential has been used successfully for transition and noble metals. Its accuracy has been verified by comparing its results with experimental data as well as DFT calculations.

2.1.2 Global optimization and basin hopping

Once the potential energy of a system of N atoms is specified, such as in the case of the Gupta potential, the search of the lowest-energy structure (which include its optimal chemical ordering) can be looked for by a procedure known as *global optimization*, which aims at finding the global minimum of the potential energy function $U(\{\mathbf{R}\})$. The solution, then, will be a set of atomic coordinates $\{\mathbf{R}^*\} = (\mathbf{R}^*_1, \mathbf{R}^*_2, ..., \mathbf{R}^*_N)$. As anticipated, such procedure is a very important tool for computational studies of NPs, since the determination of this particular atomic configuration is a crucial step for a direct comparison with experimental results at low temperatures. In fact, excluding zero-point energy, the global minimum of the potential energy coincides with the structure adopted at thermal equilibrium in the limit $T \to 0$. Very often, this structure remains the most stable even at higher temperatures -

sometimes even up to room temperature - and calculations that include temperature effects recover these results.

The problem of global optimization is very difficult and challenging, since it involves the determination of the global minimum of a function of many variables. An analytical minimization of the potential energy function is of course impossible. Similarly, the selection of the global minimum by inspection of all the local minima is unfeasible for sizes larger than a few atoms; it has been demonstrated that the number of local minima for a NP of approximately 50 atoms can exceed 10^{12} [35, 36]. Thus, one is left with the possibility of exploring only a finite amount of the domain where the potential energy function is defined. In this case, a successful global optimization algorithm must be very efficient in scanning as much as possible the $3N-$dimensional space, especially in the relevant part of it in which the value of the potential energy is low. A lot of effort has been put in the realization of an efficient global optimization scheme and indeed several proposals have been made through the years, for nanoparticles only [37–41], and also for more general purpose, including different methods such as basin hopping and evolutionary-based algorithms [42–45], lattice Monte Carlo [46], mirror-rotation optimization algorithms [47], curvilinear coordinate [48] and biminima optimizations [49, 50]. Here we will describe the *basin hopping* (BH) algorithm [51, 52] and some adaptations for the optimization of nanoparticles structures.

In the basin hopping scheme, an initial configuration $\{\mathbf{R}^0\} = (\mathbf{R}_1^0, \mathbf{R}_2^0, ..., \mathbf{R}_N^0)$ is randomly chosen in a given box, and locally minimized. Different algorithms for the local optimization are available; in this thesis we used the L-BFGS algorithm [53]. The minimization produces a configuration $\{\mathbf{R}^0\}'$, with potential energy $U'(\{\mathbf{R}^0\}')$. Then, a new configuration $\{\mathbf{R}^1\}$ is build by applying some transformation to the set of atomic coordinates $\{\mathbf{R}^0\}'$, and locally minimized as well, to produce $\{\mathbf{R}^1\}'$, with energy $U'(\{\mathbf{R}^1\}')$. At this point, the Metropolis-Hastings rule based on the locally-minimized energy difference $\Delta U' = U'(\{\mathbf{R}^1\}') - U'(\{\mathbf{R}^0\}')$ is used as an acceptance rule to select or reject the new configuration [36, 54]. This criterion chooses whether to accept or not with probability

$$p = \min[1, \exp(-\Delta U'/k_B T)], \tag{2.7}$$

that is, if $\Delta U' < 0$ the new structure is accepted and is taken as the new starting configuration. If otherwise, a random number r, uniformly distributed in $(0,1]$, is generated. If $r \leq \exp(-\Delta U'/k_B T)$, then the new configuration is accepted. The parameter T has the dimension of a temperature, but it does not represent a real physical quantity. It must be tuned by noting that a bigger value will increase the probability of accepting high energy configurations. In this respect, T should be reasonably high to ensure that the basin hopping algorithm explores different parts of the potential energy landscape, so that the simulation does not

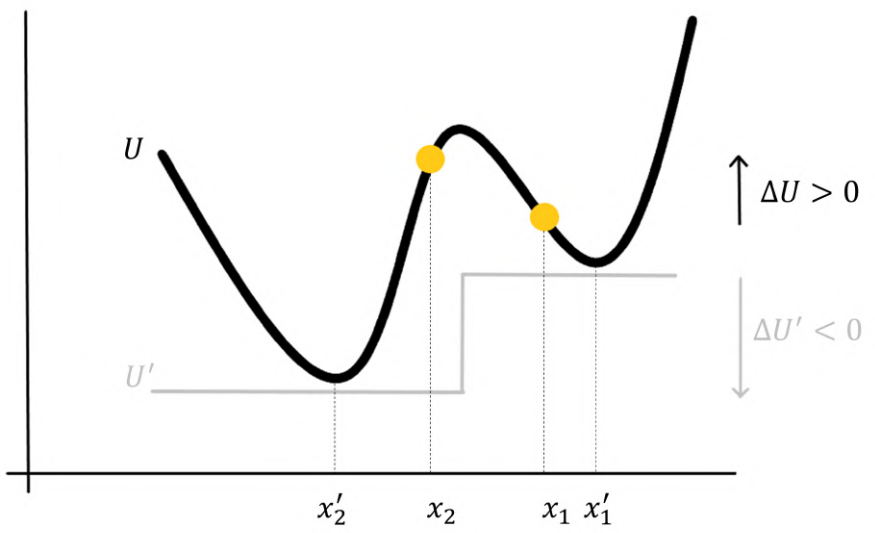

Fig. 2.1 One-dimensional potential energy curve, in black, and its local minimization in grey. Transformation of coordinates from one configuration x_1 to another x_2 (yellow dots), both with and without local minimizations.

get trapped into some local minimum. Likewise, it should not be too high, or it would be difficult to get into the low-energy minima. The advantage of using the acceptance rule on the locally minimized potential energy is clarified in Fig. 2.1. Considering this example, if a transformation of coordinates mapped x_1 to x_2 on the original potential energy curve, we would accept the new configuration with a probability smaller than 1, since $\Delta U > 0$. On the other hand, at the price of a local minimization, the new configuration is accepted with probability 1, since $\Delta U' < 0$. Thus, in this way, it is easier to explore nearby minima of the potential energy surface. It is of primary importance the choice of an appropriate set of atomic coordinate transformations. These transformations are usually referred to as *moves*. Implementing inappropriate moves would badly affect the efficiency of the global optimization algorithms, possibly deviating the exploration of the potential energy surface into the wrong direction. For this reason, different moves - specifically tailored for the global optimization of metal nanoparticles - have been proposed. Here we discuss three types: *shake*, *Brownian* and *exchange moves*.

- shake move

  In a *shake move* each atom is displaced randomly inside a sphere, or a cube, centered around its present position. Depending on the size of the sphere (or cube) the displacement can produce configurations that differ a lot from the initial one. In each case, every atom cannot be displaced more than some distance R_{max} from its position. The

value of R_{max} shall not be too small, otherwise the new configuration will be almost identical to the previous one and the move will not make any improvement in the exploration of the energy landscape, but not too big also, otherwise the new configuration will probably have an energy which is too big to be accepted. Typically, in metal clusters, R_{max} is chosen as half the nearest-neighbour distance of the bulk lattice. However, other choices are possible. For example, R_{max} can be chosen differently for atoms that are in the inner or outer part of the nanoparticle.

- Brownian move

  In a *Brownian move* each atom is displaced along a trajectory derived by the calculation of the forces that act on it (see section 2.1.3). This approach should mimic the natural evolution occurring in the nanoparticle when it is in vacuum at a given temperature, which is a parameter of the move. Usually, this temperature is high - between 1500 and 2500 K - and the system is let to evolve for no more than a few picoseconds.

- exchange move

  In a *exchange move*, defined for nanoalloys only, two atoms of different chemical species are swapped. The two atoms can be chosen at random or not, for example by assigning them different probabilities to be chosen depending on their position. This strategy could be particularly helpful in the case in which, for example, a general chemical ordering of the nanoparticle must be recovered for some reason, i.e. some previous theoretical knowledge or as suggested by experimental results.

Shake moves and Brownian moves are used for optimizing the geometric shape of the nanoparticle, whereas exchange moves are used, at fixed geometry, to optimize its chemical ordering. In general, these moves are accepted by the Metropolis-Hastings rule at different temperatures. It was shown that for shake and Brownian moves, the optimal acceptance temperature range is 1000-2000 K, being 100-300 K for exchange moves instead [13, 55]. Notably, it was also demonstrated that an efficient recipe for the global optimization of nanoalloys is to optimize together the geometry and the chemical ordering, by using both kind of moves - with different proportion - accepted at temperatures in the range as given above.

2.1.3 Molecular Dynamics

Molecular Dynamics (MD) is a series of computational methods that aim at solving numerically the equations of motion for a generic system under investigation. In classical Molecular Dynamics, Newton's equations are solved for a given force field. In quantum Molecular

Dynamics, *ab initio* methods are used to solve the electronic Schrödinger equation at fixed nuclei in order to calculate energies and forces, and then classical integration of the equations of motion is performed. In this thesis, only classical Molecular Dynamics was used. Forces were calculated from the Gupta potential as described in section 2.1.1.

The numerical integration of the Newton's equations of motion goes through the discretization of time in small time steps and the use of some algorithm for the propagation of the trajectories. In this thesis the velocity-Verlet algorithm was used [56]. In this scheme, the equations of motion are integrated as follows:

$$\mathbf{r}_i(t+\delta t) = \mathbf{r}_i(t) + \mathbf{v}_i(t)\delta t + \frac{1}{2}\mathbf{a}_i(t)\delta t^2 \tag{2.8}$$

$$\mathbf{v}_i(t+\delta t) = \mathbf{v}_i(t) + \frac{1}{2}\left[\mathbf{a}_i(t) + \mathbf{a}_i(t+\delta t)\right]\delta t \tag{2.9}$$

where $\mathbf{r}_i(t)$, $\mathbf{v}_i(t)$ and $\mathbf{a}_i(t)$ are the position, velocity and acceleration of atom i, respectively, and δt is the time step. As in all numerical integrations, the precision is directly connected to the size of the step used. In MD simulations then, the precision is controlled by the size of the time step. In general, the time step must be chosen small enough so that a good sampling of the motions of atoms at their typical time scale is guaranteed. Nevertheless, the time step cannot be chosen arbitrarily small, for it may take too long for a simulation to finish in a reasonable time. For metal nanoparticles the time scale of atomic vibrations is around some picoseconds, so that the time step is usually set to a few femtoseconds. In this thesis we always used a time step of 5 femtoseconds. The solution of the Newton's equations of motion for each atom, $\mathbf{F}_k = m_k\mathbf{a}_k$, should lead in principle to a trajectory in phase space in which - numerical errors apart - energy is conserved. However, in all experiments the physical quantity which is kept constant is the temperature. Molecular dynamics simulations at constant temperature are also possible. For this kind of simulations, an algorithmic artifact - a *thermostat* - is implemented to force atom trajectories to follow those expected at the canonical equilibrium distribution at the chosen temperature. In this thesis the Andersen thermostat [56, 57] was employed. The stabilization of temperature works as follows. Each atom can artificially collide with the thermostat with some given frequency. If this is the case, its velocity is extracted from the Maxwell distribution at the desired temperature. The collision frequency is another parameter of the simulation, and must be selected noting that a small frequency would not let the system to be stably thermalized and that a large frequency would perturb atom trajectories too strongly to avoid unphysical effects. A typical value for noble metal NPs that was used in this thesis is $5 \cdot 10^{11}$ s^{-1} [58].

2.2 Density Functional Theory

In Density Functional Theory, the potential energy of a nanoparticle $U(\{\mathbf{R}\})$ is calculated by solving the quantum electronic problem for the fixed positions of nuclei $\{\mathbf{R}\}$. The hamiltonian of a nanoparticle having N atoms for a total of m electrons, is, in Hartree atomic units:

$$H = -\frac{1}{2}\sum_i \nabla_i^2 - \frac{1}{2}\sum_I \frac{\nabla_I^2}{M_I} + \frac{1}{2}\sum_{i\neq j}\frac{1}{|\mathbf{r}_i - \mathbf{r}_j|} - \sum_{i,I}\frac{Z_I}{|\mathbf{r}_i - \mathbf{R}_I|} + \frac{1}{2}\sum_{I\neq J}\frac{Z_I Z_J}{|\mathbf{R}_I - \mathbf{R}_J|}, \tag{2.10}$$

where the first two terms represent the kinetic energy operators of electrons and nuclei respectively, the third term represents electron-electron interactions, the fourth electron-nuclei interactions and the last one represents the interactions between nuclei, each with a positive charge Z_I. In the Born-Oppenheimer approximation [59], the large difference between the electron mass and that of nuclei is exploited to treat separately the motion of both. Then, for a fixed position of the N nuclei $\{\mathbf{R}\}$, we can consider the motion of electrons as interacting particles in the external field of nuclei. The hamiltonian for electrons only is

$$H_{el} = -\frac{1}{2}\sum_i \nabla_i^2 + \frac{1}{2}\sum_{i\neq j}\frac{1}{|\mathbf{r}_i - \mathbf{r}_j|} - \sum_{i,I}\frac{Z_I}{|\mathbf{r}_i - \mathbf{R}_I|} \tag{2.11}$$

and the associated time-independent Schrödinger equation is

$$H_{el}\psi_k(\{\mathbf{R}\};\{\mathbf{r}\}) = E_k(\{\mathbf{R}\})\psi_k(\{\mathbf{R}\};\{\mathbf{r}\}), \tag{2.12}$$

where $\psi_k(\{\mathbf{R}\};\{\mathbf{r}\})$ are eigenstates of electrons, in which fixed position of nuclei play the role of parameters, being the positions of the electrons $\{\mathbf{r}\}$ the only variable. The ground state energy of the system of electrons is taken as the potential energy of nuclei, that is we make the following identification: $U(\{\mathbf{R}\}) = E_0(\{\mathbf{R}\})$. In *ab initio* methods, a numerical approach is devoted to the solution of eq. (2.12). It is clear that the accuracy achieved by this methods must be paid in terms of computational cost. In quantum Molecular Dynamics, for example, at each time step the ground state of the system of electrons must be computed in order to estimate the forces that act on nuclei. Therefore, this technique is reserved only for small systems and for few time steps. A major issue is the complexity of the problem given by the $3m$-dimensional variable $\{\mathbf{r}\}$ for the positions of electrons. Some *ab initio* methods, such as Hartree [60, 61] or Hartree-Fock [62, 63], try to overcome this problem by taking a simplified wavefunction for the electrons, such as a Hartree product or a Slater determinant, respectively, and varying some coefficients to get an estimate for the ground state.

The drawback is that the choice of the form of the wavefunction constitutes a remarkable constraint for the solution of the problem. In Density Functional Theory, the electron density $n(\mathbf{r})$ is used as a variable in place of $\{\mathbf{r}\}$, for solving the quantum electronic problem of eq. (2.12). Therefore, the problem is three-dimensional instead of $3m$-dimensional, which is an outstanding simplification. Moreover, no guess is made for the wavefunction of electrons. The possibility of using $n(\mathbf{r})$ as a variable is due to Hohenberg and Kohn, who demonstrated two fundamental theorems in the mid-sixties [64, 65] that still lay the foundations of DFT. For a state ψ, the electron density is defined as

$$n(\mathbf{r}) = \langle\psi| \sum_{i=1}^{m} \delta(\mathbf{r}-\mathbf{r}_i)|\psi\rangle \tag{2.13}$$

The theorems state that it is possible for any system to define an energy functional of the electron density $E[n]$, that the ground state energy of the system is the global minimum of $E[n]$ and that the ground state density $n_0(\mathbf{r})$ is the one that minimizes $E[n]$, where $n_0(\mathbf{r})$ is the electron density associated with the ground state ψ_0. Therefore, it is in principle possible to determine the potential energy $U(\{\mathbf{R}\})$ by searching for the global minimum of the energy functional. In practice, this is equivalent to solving the variational problem

$$\frac{\delta}{\delta n}\left\{E[n] - \lambda\left[\int d\mathbf{r}\, n(\mathbf{r}) - m\right]\right\} = 0, \tag{2.14}$$

where λ is a Lagrange multiplier due to the normalization of the electron density to the total number of electrons m. The energy functional for a state ψ is given by

$$E[n] = \langle\psi|H_{el}|\psi\rangle, \tag{2.15}$$

which can be written as

$$E[n] = F[n] + \int d\mathbf{r}\, n(\mathbf{r}) V_{ext}(\mathbf{r}), \tag{2.16}$$

where $V_{ext}(\mathbf{r}) = -\sum_I Z_I/|\mathbf{r}-\mathbf{R}_I|$ is the external field of nuclei and $F[n]$ is a universal functional of the electron density, including kinetic energy and electron-electron interactions:

$$F[n] = T[n] + \int\int d\mathbf{r} d\mathbf{r}' \frac{n^{(2)}(\mathbf{r},\mathbf{r}')}{|\mathbf{r}-\mathbf{r}'|}. \tag{2.17}$$

In the last equation, $T[n]$ is the kinetic energy functional, and $n^{(2)}(\mathbf{r},\mathbf{r}')$ is the two-particle density. The analytical form of the latter is not known, but it can be decomposed in two parts: $n^{(2)}(\mathbf{r},\mathbf{r}') = n(\mathbf{r})n(\mathbf{r}') + \Delta n^{(2)}(\mathbf{r},\mathbf{r}')$, in which the first term is the product of densities, which

would correspond to $n^{(2)}(\mathbf{r},\mathbf{r}')$ for a system of uncorrelated particles, and the last term is a correction needed for the correlated electrons. Thus

$$F[n] = T[n] + \int\int d\mathbf{r}d\mathbf{r}' \frac{n(\mathbf{r})n(\mathbf{r}')}{|\mathbf{r}-\mathbf{r}'|} + \Delta E \tag{2.18}$$

A similar decomposition can be done for the kinetic energy. For a system of non interacting particles, a wavefunction can be chosen in the form of a Slater determinant. In this case, the kinetic energy functional can be written simply as

$$T[n] = -\frac{1}{2}\sum_i \int d\mathbf{r}\, \phi_i^*(\mathbf{r})\nabla^2\phi_i(\mathbf{r}), \tag{2.19}$$

where $\phi_i(\mathbf{r})$ are the single-particle orbitals used for building the Slater determinant. For a system of interacting electrons, then:

$$F[n] = -\frac{1}{2}\sum_i \int d\mathbf{r}\, \phi_i^*(\mathbf{r})\nabla^2\phi_i(\mathbf{r}) + \int\int d\mathbf{r}d\mathbf{r}' \frac{n(\mathbf{r})n(\mathbf{r}')}{|\mathbf{r}-\mathbf{r}'|} + \Delta E + \Delta T, \tag{2.20}$$

where ΔT is the correction needed to recover the true kinetic energy of the system. Putting all together, we have

$$E[n] = -\frac{1}{2}\sum_i \int d\mathbf{r}\, \phi_i^*(\mathbf{r})\nabla^2\phi_i(\mathbf{r}) + \int\int d\mathbf{r}d\mathbf{r}' \frac{n(\mathbf{r})n(\mathbf{r}')}{|\mathbf{r}-\mathbf{r}'|} + \int d\mathbf{r} n(\mathbf{r})V_{ext}(\mathbf{r}) + E_{xc}, \tag{2.21}$$

where we defined the exchange-correlation functional $E_{xc} = \Delta E + \Delta T$ that incorporates every part of the energy functional which is due to interactions between electrons. In principle, this expression for the energy functional could be put in eq. (2.14) for solving the problem. However, the expression of $E[n]$ contains both the electron density $n(\mathbf{r})$ and the free-particles orbitals. To overcome this problem, Kohn and Sham proposed an *ansatz* that postulate the existence of a system of non interacting electrons having the same density $n(\mathbf{r})$ of the interacting system. In this case, the density of the non interacting system can be easily derived from the Slater determinant. It turns out that it can be written as $n(\mathbf{r}) = \sum_i |\phi_i(\mathbf{r})|^2$, and substituted in eqs. (2.21) and (2.14), in which the normalization condition for the density is replaced by a normalization condition for the orbitals: $\sum_i \varepsilon_i(\langle\phi_i|\phi_i\rangle - 1)$. By using the chain rule, one can take the variation with respect to $\phi_i^*(\mathbf{r})$, and obtain the Kohn-Sham equations:

$$\left[-\frac{1}{2}\nabla^2 + V_{eff}\right]\phi_i(\mathbf{r}) = \varepsilon_i\phi_i(\mathbf{r}), \tag{2.22}$$

where we defined the effective potential

$$V_{eff}(\mathbf{r}) = V_{ext}(\mathbf{r}) + \int d\mathbf{r}' \frac{n(\mathbf{r}')}{|\mathbf{r}-\mathbf{r}'|} + \frac{\delta E_{xc}}{\delta n(\mathbf{r})}. \tag{2.23}$$

Theese equations must be solved self-consistently, since the electron density $n(\mathbf{r})$ - and so the orbitals - affects the effective potential V_{eff} itself. The form of E_{xc} is not known. Several approximations have been proposed in the literature, such as Local Density Approximation (LDA) [66], Perdew–Burke-Ernzerhof [67, 68] and many others. Once the Kohn-Sham equations are solved, the physical quantities of interest can be extracted either from the orbitals or from the electron density. For example, some given nanoparticles structures could be locally minimized to compare their energies, in order to gain knowledge about their stability at low temperature by means of a more precise method. More on this will be shown in the next chapters. Another possible employment of DFT is to calculate adsorption energies of single atoms or molecules on NPs surfaces, especially for chemical species that would be hard to describe with atomistic potentials. Many other applications are of course possible, including for example band-structure [69], optical properties [70, 71] and so on. A lot of other details should be explained to fully appreciate how the solution of these equations is actually put into practice. However, it is out of the scope of this thesis. Very good references are for example the excellent books of Engel and Dreizler [72], Kaxiras [73], Thijssen [74] and references therein.

2.3 Machine Learning

Machine Learning (ML) is a large set of techniques that are based on the training of some models on data [75–77]. In general, these techniques are divided in two classes: *supervised* and *unsupervised learning* algorithms.

In supervised learning, input data of some space X and output data of some space Y are given, and a function that best describes the relation between them is looked for, by minimizing a loss function that measures the error of the model. In the statistical learning approach, special attention is devoted to the ability of the model, which is fitted on training data, to generalize well on unseen data - the *test* data. This task is usually achieved by constraining the model not to fit at best the training data, in order to keep some flexibility for good extrapolations. In unsupervised learning, only input data from some space X are given. The hypothesis is that there is some underlying, unknown subdivision of points of input data in some groups that must be discovered. Therefore, the aim of any unsupervised learning algorithm is to find to which group each point belongs to, that is to assign a label to

each point. In the following we will describe two very popular algorithms that were used for this purpose in this thesis: K-Means [75, 78] and Gaussian Mixture Model (GMM) [75, 79, 80]. For both cases, the input data consists in a set τ of n points sampled from a space $X \subseteq \mathbb{R}^d$. We will then discuss some methods to infer the optimal number of groups in the data set as well as a popular technique that is frequently used for reducing the dimension d of the problem.

2.3.1 K-Means

The objective of the algorithm is to divide τ in k groups, where k is a fixed integer. This algorithm is based on a geometric approach. We are interested in finding the Voronoi tessellation of the set, with k cells. Let m_j be the unknown centroids of the cells C_j that need to be found for constructing the tessellation. Each cell C_j contains the points x of τ that are closer to it than any other cell C_i, i.e. they satisfy the following condition:

$$C_j = \{x \in X \mid D(x,m_j) \leq D(x,m_i) \;\; i \neq j\}, \tag{2.24}$$

where $D(\cdot,\cdot)$ is the distance defined in X. In this thesis we only used the Euclidean distance. For solving this problem, a penalty function L that measures how far each point is to its closest cell is defined,

$$L(m_1,...,m_k) = \sum_{i=1}^{n} \min_{j=1,...,k} ||x_i - m_j||^2 \tag{2.25}$$

so that the problem can be stated as a minimization of the penalty function all over the centroids m_j:

$$\min_{m_1,...,m_k} L(m_1,...,m_k) = \min_{m_1,...,m_k} \sum_{i=1}^{n} \min_{j=1,...,k} ||x_i - m_j||^2. \tag{2.26}$$

The Voronoi tessellation is given by the set $(m_1^*,...,m_k^*)$ that minimizes L. An iterative solution was proposed by Lloyd [81]. It consists in solving the two minimizations of eq. (2.26) iteratively. The steps are the following:

- Random initialization of centroids:

  $$m_1^0,...,m_k^0, \;\; C_j^0 = \emptyset.$$

  Other schemes for the initialization of centroids have been proposed, such as in K-Means++ [82].

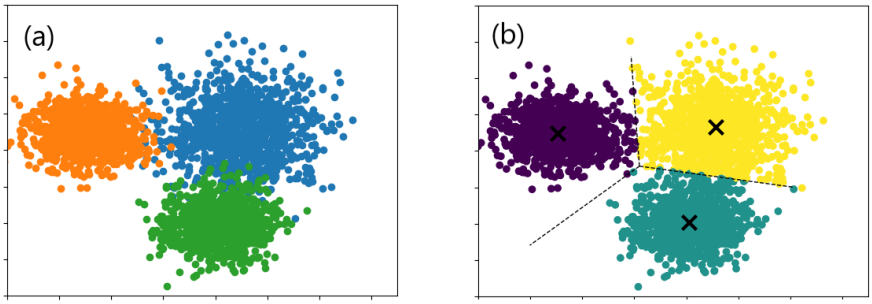

Fig. 2.2 (a) Original data set generated with Gaussian distributions, each already colored differently for comparison with (b) the Voronoi tessellation as found by K-Means for $k = 3$.

- Assignment of points to their closest cell:

$$j(i) = \underset{j=1,\dots,k}{\arg\min} ||x_i - m_j^0||^2, \quad i = 1,\dots,n.$$

$$C_{j(i)}^1 = C_{j(i)}^0 \cup \{i\}.$$

- Update of centroids based on the points inside the cell:

$$m_j^1 = \frac{1}{\#C_j^1} \sum_{i \in C_j^1} x_i, \quad j = 1,\dots,k.$$

where we denote by $\#C_j$ the number of element of the j-th class. The steps are repeated until some convergence criterion on the penalty function are met, or when a maximum number of steps has been reached. It can be shown that this procedure never increases L, but also that the solution could be a local minimum [75]. An example of a K-Means performance is shown in Fig. 2.2.

K-Means owns its popularity for its ease of implementation and low computational costs. However, for its lack of flexibility, it is not well suited for cases in which input data are expected to be clustered in non-trivial shapes. For this purpose, the next algorithm that is discussed may be preferred.

2.3.2 Gaussian Mixture Model

Gaussian Mixture Model is an unsupervised learning algorithm that is instead based on a probabilistic approach. The basic assumption is that each point x_i in τ has been generated according to a mixture of k Gaussian probability distributions with unknown parameters. These parameters include the weights of the mixture, as well as centers and covariance

matrices of the normal distributions. The goal of the algorithm is to find all these parameters by maximizing the log-likelihood of the model:

$$\ell = \sum_{i=1}^{n} \log \left(\sum_{j=1}^{k} \frac{\pi_j}{\sqrt{(2\pi)^d |\Sigma_j|}} e^{-(x_i-\mu_j)^T \Sigma_j^{-1} (x_i-\mu_j)} \right), \tag{2.27}$$

where π_j are the weights of each distribution in the mixture, μ_j and Σ_j are the centers and covariance matrices of the distributions, respectively. We denote by $|\Sigma_j|$ the determinant of Σ_j. The solution is found again by an iterative two-step approach [79, 80]:

- Random initialization of all parameters:

$$\theta^0 = (\pi_1^0, ..., \pi_k^0, \mu_1^0, ..., \mu_k^0, \Sigma_1^0, ..., \Sigma_k^0)$$

- Calculation of posterior probabilities:

$$\gamma_i^0(j) = \frac{\pi_j^0 N(x_i|\mu_j^0, \Sigma_j^0)}{\sum_{j=1}^{k} \pi_j^0 N(x_i|\mu_j^0, \Sigma_j^0)} \quad i = 1, ..., n \quad \text{and} \quad j = 1, ..., k.$$

  In this expression $N(x_i|\mu_j^0, \Sigma_j^0)$ is the normal distribution

$$N(x_i|\mu_j^0, \Sigma_j^0) = \frac{1}{\sqrt{(2\pi)^d |\Sigma_j^0|}} e^{-(x_i-\mu_j^0)^T (\Sigma_j^0)^{-1} (x_i-\mu_j^0)}.$$

- Update of mixture model parameters:

$$\mu_j^1 = \frac{\sum_{i=1}^{n} \gamma_i^0(j) x_i}{\sum_{i=1}^{n} \gamma_i^0(j)},$$

$$\Sigma_j^1 = \frac{\sum_{i=1}^{n} \gamma_i^0(j)(x_i - \mu_j^1)(x_1 - \mu_j^1)^T}{\sum_{i=1}^{n} \gamma_i^0(j)} \quad \text{and}$$

$$\pi_j^1 = \frac{\sum_{i=1}^{n} \gamma_i^0(j)}{n}.$$

As in the previous case, the iteration is terminated after a prefixed number or steps of until some convergence criterion on the maximum likelihood is met. Finally, each point x_i is assigned to the j-th distribution that is more likely to have generated it, i.e. the one with highest $\gamma_i(j)$. This model is more flexible than K-Means for the greater number of parameters that are used to fit all the distributions. Therefore, it is recommended for cases in which it

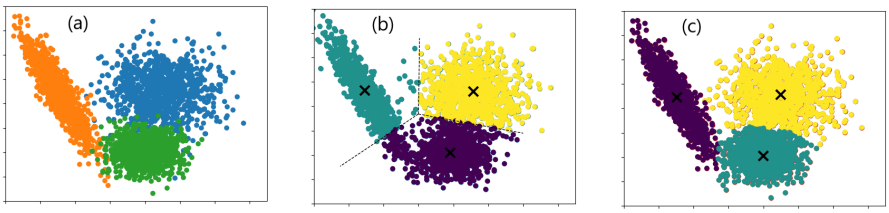

Fig. 2.3 (a) Original data set generated with Gaussian distributions, each already colored differently for comparison with (b) the Voronoi tessellation as found by K-Means for $k = 3$ and (c) the subdivision found by GMM for $k = 3$.

is expected that points in the input data set are divided in groups with different shapes. An example of this is shown if Fig. 2.3. However, it has cubic complexity with respect to the dimension d, whereas K-Means scales linearly. For this reason, for high-dimensional data sets it is generally slower. In this thesis, as will be described in the next chapter, we only used up to $d = 4$, so the difference in calculation times due to this factor has never been so great.

2.3.3 Determination of the number of cluster k

In the previous discussion, k has been as a fixed integer. That is, the number of clusters was predetermined. However, in general, the number of clusters cannot be guessed if there is no particular knowledge about the system under investigation. Therefore, a recipe for estimating the optimal k must be followed, in order to unbias the application of clustering algorithms. The usual recipes assign a score to every k, and then the k value corresponding to the best score is selected as the optimal number of clusters. We describe the three types of scores that were used in this thesis.

A very simple score is the silhouette score [83, 84], which is calculated as the average of silhouette coefficients s_i of each point x_i. The silhouette coefficients are defined as

$$s_i = \frac{b_i - a_i}{\max(a_i, b_i)}, \tag{2.28}$$

where a_i is the average distance from x_i to other points in its cluster and b_i is the smallest average distance from x_i to other points of other clusters. The silhouette coefficient ranges from -1 to 1. For a point that is well classified, the intra-cluster average distance a_i will be small, and the smallest inter-cluster average distance b_i will be in general large, resulting in a coefficient near 1. For a badly classified point, the opposite holds and the coefficient will be near -1. The optimal number of clusters k is thus the one that maximizes the silhouette score.

Another score that was used for GMM only is the Bayesian Information Criterion (Bic) [85], defined as

$$\mathrm{Bic}(k) = m(k)\log(n) - 2\ell, \tag{2.29}$$

where $m(k)$ is the number of parameters of the k-components mixture model, n the number of points and ℓ the log-likelihood as defined in eq. (2.27). The optimal number of cluster is the number k that minimizes the Bic score. The minimization realizes the tradeoff between a highly accurate model (high value of ℓ, which is favored) and an easy model (few parameters, which is also favored). In fact, a small number of distributions k has few parameters but in general a poor log-likelihood value, while a large value of k will lower the log-likelihood - for it is easier to fit with many functions - but a greater number of parameters.

The third score is the gap statistic [86], defined as

$$\mathrm{Gap}(k) = \mathbb{E}_n^*[\log(W_k)] - \log(W_k), \tag{2.30}$$

where

$$W_k = \sum_{r=1}^{k} \frac{1}{2n_r} D'_r, \quad n_r = \#C_r, \tag{2.31}$$

being C_r the r-th cluster, $\#C_r$ the number of elements in that cluster and

$$D'_r = \sum_{i,j \in C_r} D(x_i, x_j). \tag{2.32}$$

The expectation is taken under a null reference distribution. The optimal number of cluster is selected using the "1-standard error" rule, i.e. the smallest k satisfying

$$\mathrm{Gap}(k) \geq \mathrm{Gap}(k+1) - s_{k+1}, \tag{2.33}$$

where s_{k+1} is an error calculated from the values of $\log(W_k)$ used for the estimation of the expectation. More details can be found in Ref. [86].

2.3.4 Principal Component Analysis

As mentioned before, unsupervised learning algorithms may scale differently with the dimension d, so that it would be useful to map the problem into a simplified version in which d is diminished. Moreover, high-dimensional data sets are hard to visualize, and even more are the results of any unsupervised learning algorithm. Principal Component Analysis (PCA) [87], is probably the most well-known algorithm for the general problem of dimensionality reduction. This problem is about searching for a map which transforms a high-dimension

data set into a low-dimension version of the same data set, still preserving the most of its properties. In particular, the aim of PCA is to look for a set of p vectors in the original space X, with $p \ll d$, along which the variance of the projected data set is maximum. If, as usually, the input data set τ consists of n observation x_i of some d-dimensional space X, the first principal component is defined as

$$w_1^* = \underset{w \in \mathbb{R}^d, |w|=1}{\arg\max} \frac{1}{n} \sum_{i=1}^{n} (w^T x_i)^2, \tag{2.34}$$

that is the direction in X along which the variance of τ is maximixed. The second principal component is calculated by first considering the "residuals" of the data set, defined as $r_i = x_i - (w_i^{*T} x_i) w_i^*$, and then by looking for a direction w_2^* orthogonal to the first along which the variance of the residuals is maximized, as in eq. (2.34). This process is continued until all p principal components w_i^* are computed. Finally, the data set is transformed by taking all projections: $x_i \to (w_1^* x_i, w_2^* x_i, ..., w_p^* x_i)$. The number of principal components p must be chosen properly noting that i) a small number will benefit a simpler description of the data set but it will necessarily lose some information (the overall amount of variance along all the components) and that ii) a large number will be more precise, as a higher amount of variance will be "explained" by the principal components, but will result in a complex description which does not allow a simple visualization. More importantly, in the second case, unsupervised learning algorithm implementations will be heavier, due to time complexities' dependence on the dimension. In our experience, we found that in most cases, two or three principal components are enough to keep between 90% and 95% of the overall variance of the data set, which is a commonly accepted threshold [88, 89].

Chapter 3

Clustering of nanoparticles

As described in previous chapters, computer simulations play a fundamental role in the investigation of the properties of metal nanoparticles, as they represent an indispensable tool for understanding experimental results. Indeed, computer simulations proved several times to be capable of solving some issues otherwise too hard to tackle by means of theoretical or experimental tools - see for example Refs. [19, 90]. With nowadays resources, some properties of a nanoparticle composed of a few hundreds of atoms can be studied *ab-initio* by means of DFT in a reasonable amount of time. Larger sizes and time scales can be studied by simplified atomistic approaches, in much faster calculations. Typically, the optimal structure (and also the chemical ordering if there are two or more metals) of a NP is searched by global optimizations techniques, such as BH or genetic algorithm, which implement clever ideas to explore the atomistic potential energy landscape, as described in the previous chapter. Then, thanks to Molecular Dynamics simulations, the thermal evolution and/or growth of a NP composed of thousands of atoms can be followed for tens of μs [91]. Even larger sizes and time scales are achieved by coarse-grained models, in which also complex environments of nanoparticles (for example solid substrates and embedding matrices) can be simulated and studied [92].

A common feature of these simulations is the production of large outputs, usually many NP structures in some three-dimensional coordinates file format. The systematic analysis of all these structures can be a far from trivial task for complex systems, and since these data usually contain crucial amount of information, this procedure cannot be simply bypassed. Automatic tools capable of doing this job are then quite convenient. In particular, an automatic procedure for the subdivision of nanoparticle structures large datasets into different groups, based on some similarity criterion, was missing. We note that the manual inspection of three dimensional structures - for example by means of molecular modeling software - is not guaranteed to be the best approach for solving this problem. In fact, such an approach is i)

very time-consuming, especially for large data sets, and ii) not necessarily the most accurate, since some geometric details of the three dimensional structures could be easily missed at human-eye level.

Here, we describe two procedures based on a combined approach of Machine Learning and Common Neighbour Analysis (CNA) that solve this problem. These procedures resulted in three publications [93–95]. We show that for both procedures, CNA is very well suited for a successful and physically meaningful description of NPs that is necessary for unsupervised learning algorithms to solve the clustering problem efficiently.

The first procedure [93, 94], discussed in section 3.2, relies on a very simple two-dimensional description derived from the elaboration of two order parameters given by CNA. This method has proven to be very convenient for data sets obtained by global optimization searches of nanoalloys with fixed size and different compositions. On the other hand, it failed in detecting the different groups of structures that emerged in more complex data sets such as those of MD simulations at high temperatures.

The second procedure [95], described in section 3.3, is based on a more detailed description of the local environment of atoms, similar in spirit to that of some works recently published [96, 97], but with use of a different set of descriptors. It is shown to improve the first procedure in the cases in which it failed. Both CNA descriptions are preliminarily discussed in section 3.1. We also show and stress the importance of Machine Learning in the whole process. This comes essentially in two ways: first, the combined choice of a clustering algorithm and of a clustering score, which is needed in order to select the best output. This choice was made out of a combination of two different algorithms (K-Means and Gaussian Mixture Model) and three scores (Bayesian criterion information, silhouette and gap statistic). Secondly, the extraction of the most relevant information from the above-mentioned complex description through a dimensionality reduction technique, which was achieved by PCA, and that was used only in the second procedure. The application of Machine Learning algorithms (K-Means, GMM, PCA) and scores (silhouette, Bic) was done by using the open-source python module Scikit-Learn [98] (version 1.0.2), available at https://scikit-learn.org/stable/, with an exception for the gap statistic, which was calculated using our own code. We believe that this last method can be used as an effective recipe to more easily study all the different geometric structures that emerge from computer simulations of metal nanoparticles, allowing to quickly grasp some subtle differences between seemingly similar objects. The methods were applied to the following systems: AgCu, AuPd, Au and Ag nanoparticles. The potential parameters were taken from Ref. [99] for AgCu and Ag, from [100] for Au and from [101] for AuPd; they are reported in Appendix B. These systems have been widely studied in the

literature so far, both theoretically and experimentally, for their applications to catalysis [102, 103], and plasmonics [104, 105].

A note on terminology. In order to avoid confusion, aggregates of atoms will be referred to as *nanoparticles* or *nanoalloys*. On the other hand, the term *cluster* will be used in this chapter exclusively to denote a set of nanoparticle structures which are grouped together by a clustering algorithm working in the space of suitable variables (i.e. of structural descriptors).

3.1 Common Neighbour Analysis

In the Common Neighbour Analysis [106], each pair of nearest neighbours of some given structure is assigned a signature of three integers *rst* that depends on its local environment:

- r - The number of common nearest neighbours of the pair.
- s - The number of bonds between those r atoms, i.e. the number of nearest neighbours pairs in these r atoms.
- t - The length of the longest chain of bonds that can be made out of the s bonds present.

As an example, consider the atoms in a five-fold symmetry axis of a decahedral structure. A pair of nearest neighbours lying on that axis will have five common nearest neighbours placed on a pentagon, all of which are nearest neighbours. Thus the pair has a 555 signature (see Fig. 3.1 (a)). Other typical signatures are those of fcc fragments and twin planes and stacking faults, as shown in Fig. 3.1 (a) and (b), respectively.

In the first description, used for Refs. [93, 94], an order parameters *rst* OP is defined, for a single NP, as follows:

$$rst\,\mathrm{OP} = \frac{\text{number of nearest neighbours pairs having the } rst \text{ signature}}{\text{number of all nearest neighbours pairs}} \tag{3.1}$$

These order parameters are designed to quantify, in each NP, the overall amount of the structural features relative to a particular *rst* OP. The idea is that nanoparticles having fivefold symmetry will have, for example, both high 555 OP (due to atoms in fivefold axis) and 422 OP (due to atoms in twin planes). On the other hand, a perfect fcc fragment, will have both 422 and 555 OP equal to zero. A faulted fcc fragment will have 555 OP equal to zero but a nonzero 422 OP. Then, by assigning to each NP a two-dimensional variable formed by two of these *rst* OPs, one can essentially project a data set into a plane, noting that structures having similar amount of particular structural features will be automatically clustered together. The advantage in making such transformation comes from the fact that

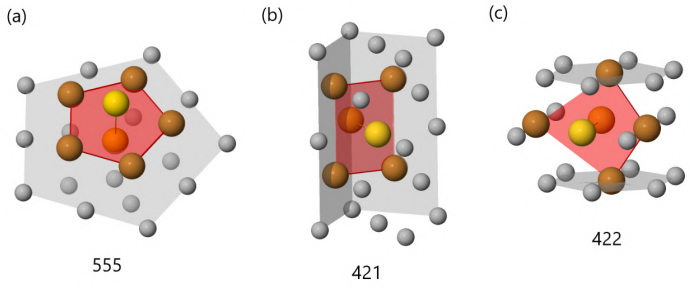

Fig. 3.1 Three typical CNA signatures. (a) 555 signature, which denotes atom pairs along 5-fold symmetry axes, such as those of icosahedra and decahedra, (b) 421 signature, which is that of a perfect FCC crystal fragment and (c) 422 signature, which is instead typical of twin planes, fcc stacking faults and hcp stackings. In all cases, yellow atoms are the reference atom pair for which one investigates the neighbourhood, whereas the common nearest neighbours of the pair (corresponding to the integer r) are colored in brown. Bonds (corresponding to the integer s) are represented by segments between brown atoms. Reprinted with permission from [95]. Copyright © 2023 The Authors. Published by American Chemical Society.

the $3N$ variables needed to represent the geometry of a nanoparticle having N atoms are reduced to only two variables. As it turns out, in some cases this reduction is sufficient to cluster some data sets of nanoparticles structures. The performance of clustering algorithms on such two-dimensional spaces is discussed in section 3.2.

The second description, used in Ref. [95], is based on the single atoms rather than atom pairs. In principle, each atom can be classified by means of the signatures of the pairs formed with all its nearest neighbours. However, this would open up too many possibilities, so that we can restrict ourselves only to a limited number of possible combinations. In fact, the analysis of a single data set composed of several nanoparticle structures will generally deliver a huge amount of different possible combinations of signatures, especially for the data sets collected in molecular dynamics simulations. Indeed, we checked that for some of our data sets there are thousands of these possible atom classifications. However, most of these combinations are rarely explored along the MD trajectory. Very often, a particular classification is explored by just one atom in a single structure for the whole simulation. In such a case, that particular classification can be discarded as its frequency is very low - and the corresponding geometry barely relevant with respect to other, more frequent features. Note that some of these combinations appear much more often than others, as they represent atoms in well defined positions. For example, an atom in a perfect fcc crystal will have twelve nearest neighbours, all of which forming a 421 signature (see Fig. 3.1 (b)). Thus, this kind of atom can be classified by a list of twelve 421 signatures. An atom placed in

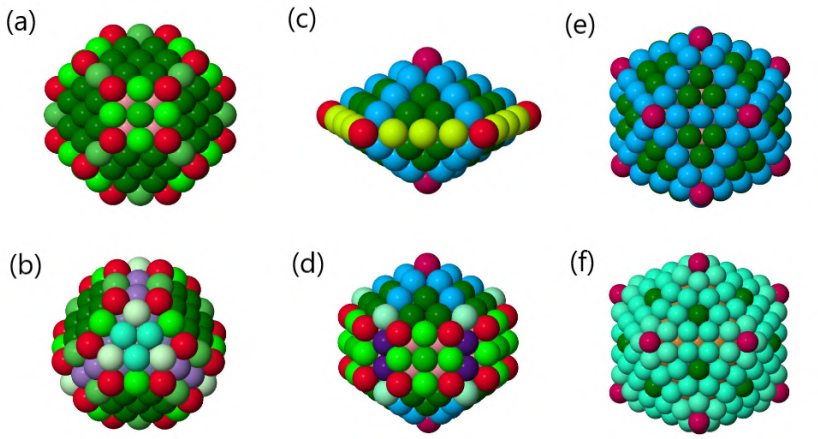

Fig. 3.2 (a) Regular truncated octahedron, (b) truncated tretrahedron with islands in stacking faults on its facets, (c) regular decahedron, (d) Marks decahedron, (e) Mackay icosahedron and (f) anti-Mackay icosahedron. Different colors refer to different atom classifications (see Table 3.1). Reprinted with permission from [95]. Copyright © 2023 The Authors. Published by American Chemical Society.

the inner part of a five-fold axis also has twelve nearest neighbours. Two these neighbours, the ones placed in the five-fold axis, just above and below it, form a 555 signature, with the original atom, while the remaining ten yield a 422 signature. A vertex of an icosahedron or a vertex of a decahedron has six nearest neighbours, five of which make a 321 signature whereas with the last one, placed just below in the five-fold axis, forms a 555 signature. In Fig. 3.2 a selection of structures is provided with atoms colored differently to show their various classifications.

We defined a list of 63 different combinations of signatures; the complete list of atom classifications can be found in Appendix A. Following this list, a 64-dimensional vector can be assigned to each NP of any simulation, in which for the i-th component of the vector the fractions of atoms of that NP having the i-th combination of signatures is calculated. This list of 63 different combinations then comes from the tradeoff for a detailed but contained range of possible atom classifications. The last component of the vector is dedicated to all the atoms that were not classified, that is those atoms whose local environment could not be described in terms of one of the 63 combinations of the list (this fraction of not-classified atoms reflected our decision to select these 63 combinations, and it would be zero in the extreme case of considering all the possible combinations that appeared in each NP in a particular data set). As an example, some of the possible combinations of signatures are listed in Table 3.1.

Table 3.1 Some atom classifications based on the list of signatures of its nearest neighbours, taken as examples from Fig. 3.2. The complete list of atom classifications can be found in Appendix A. Reprinted with permission from [95]. Copyright Copyright © 2023 The Authors. Published by American Chemical Society.

Number of nearest neighbours	list of signatures	color
7	211 211 211 311 311 421 421	
6	200 211 211 311 311 421	
9	311 311 311 311 311 311 421 421 421	
6	322 322 322 322 322 555	
8	311 311 311 311 322 322 422 422	
10	300 300 311 311 311 311 421 421 422 422	
8	200 200 322 322 322 422 422 555	

Each data set then, can be described by a collection of 64-dimensional vectors, that is a $n \times 64$ matrix, where n is the number of structures of the data set. A visualization of one of these matrices is given for example in Fig. 3.3, where for each row a vector (i.e. a NP structure), is represented by coloring each component (i.e. column) in a reverse grayscale mode. This type of visualization allows to detect, at a first glance, the most frequent signatures (i.e. the darker components) in the whole data set, which also serves as a rough first estimate of its variation.

3.2 Clustering of nanoparticles - part I

In this section we describe the first procedure mentioned earlier for dealing with the problem of the clustering of nanoparticle structures. The description closely follows that reported in Ref. [93].

The first step of the procedure is the creation of the data sets for the subsequent application of clustering algorithms and scores. Here we constructed three data sets. Each data set consists of nanoparticle structures obtained by global optimization searches for the lowest-energy structures of AgCu nanoalloys with $N = 100$ and $N = 200$ atoms. For $N = 100$, the first data set consists of the global minima of Ag_mCu_n for all compositions, i.e. for $m = 0, 1, 2, ..., 100$. For the second data set, we considered a specific composition, $Ag_{64}Cu_{36}$, and we took all the structures of the low-energy local minima collected by our BH searches. We built the third data set by collecting global minima of Ag_mCu_n with $N = 200$ and even m, i.e. $m = 0, 2, 4, ..., 200$. Therefore, all structures considered in the following correspond to local minima in the energy landscape, and, where specified, to global minima.

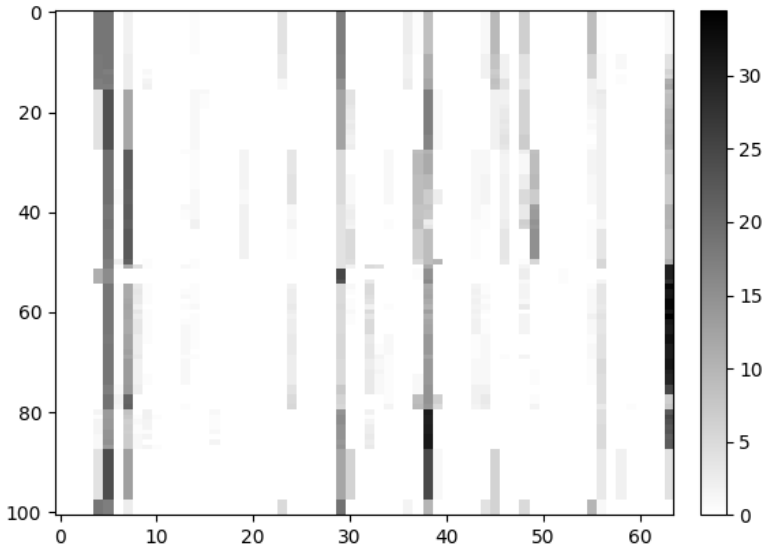

Fig. 3.3 Example of the 64-dimensional vector representation of nanoparticles given by the CNA. In this case, each row represents a AgCu nanoalloy with a different composition of Ag and Cu; each column represents a vector component whose values (i.e. percentages) are indicated in the colorbar. Data from Ref. [93]. Reprinted with permission from [95]. Copyright © 2023 The Authors. Published by American Chemical Society.

The global optimization searches were made by the Basin Hopping algorithm, using our own code [27, 107, 108]. For each composition, three independent simulations of 200000 steps each were made, using different seeds and parameters. Each of these three simulations had different proportions for Brownian, exchange, shake and bonds moves [107, 108]. Two simulations over three were using a single Monte Carlo walker (standard BH algorithm), whereas the third simulation used three different walkers running in parallel (parallel excited walker algorithm [107]). The use of different global optimization algorithms usually allows a more thorough exploration of the energy landscape. The efficiency of BH algorithm in the optimization of AgCu nanoalloy structures was already proven in Refs. [24, 109–111]. The parameters of the potential were taken from Ref. [99] and are reported in Appendix B. This interaction potential has been used previously to model the structures of AgCu nanoalloys and compared to DFT calculations and experimental results [24, 112–114], obtaining quite good agreement with DFT data on the behaviour of the composition-dependent excess energy and on the structures of lowest-energy magic polyicosahedra of sizes 34, 38 and 45 [112], on the energetics of the placement of Cu impurities in Ag icosahedra and truncated octahedra (see Ref. [13], Tables 5.1 and 5.3), on the relative stability of Mackay, anti-Mackay and chiral Cu@Ag icosahedral structures (see Ref. [24]). Moreover, the agreement between the predictions of this model and the experimentally observed structures is quite good [113] as discussed in Ref. [114]. Therefore we believe that this model, although approximate, is able to catch the relevant structural aspects of AgCu nanoalloys, with the advantage of allowing such a thorough exploration of the nanoalloy energy landscape that would be unfeasible by DFT calculations.

AgCu nanoalloys are important for a different number of remarkable reasons. In general, the bi-metallic nature of nanoalloys allows to enrich their range of applicability in real life scenarios, since the chemical ordering of equilibrium and out of equilibrium structures will induce different physical and chemical properties, missing most of the times in their single metal counterparts. For example, AgCu nanoalloys have shown interesting plasmonic [115], electrical [116], antibacterial [117] and catalytic [118] properties, but also found applications in corrosion resistance [119] and solar cells [120]. The interest in the theoretical modeling of such nanoalloys is therefore motivated by this impressive variety of experimental results

In sections 3.2.1 and 3.2.2 we provide results for $N = 100$ and $N = 200$, respectively. In section 3.2.3, we discuss different possible choices of the order parameters for the application of the clustering alogorithms. Finally, in section 3.2.4, we consider the specific composotion $Ag_{64}Cu_{36}$ for $N = 100$. We show the need of a different clustering algorithm to separate these structures into different families, and we calculate the temperature-dependent probability of these families by means of the Harmonic Superposition Approximation (HSA).

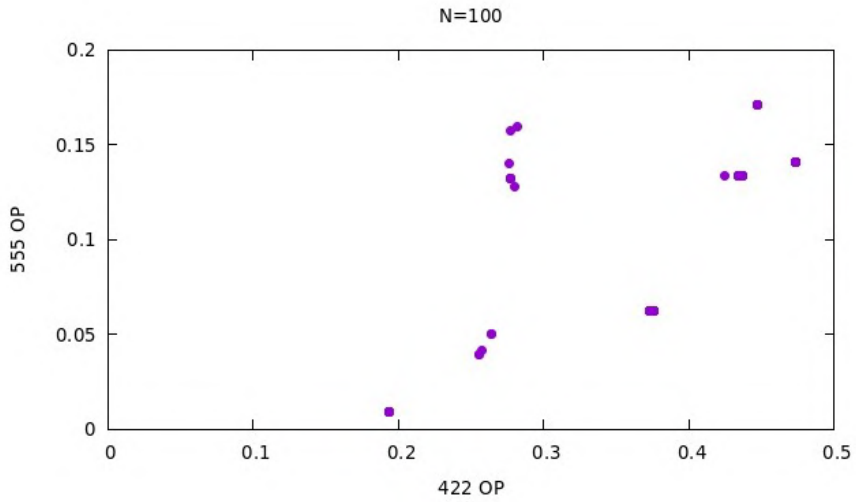

Fig. 3.4 Data set representation in the two dimensional space of 422 and 555 order parameters. For each nanoalloy, we calculated its 422 and 555 order parameters as the fractions of nearest-neighbor pairs presenting such signatures.

3.2.1 N=100

After collecting the lowest-energy structures for all compositions, the two order parameters 422 OP and 555 OP were calculated for all the 101 structures by using eq. (3.1). When the data set is projected into this two-dimensional space, points automatically separate into different groups, as shown in Fig. 3.4. However, it is still not clear exactly how many groups are there. For this reason we used the K-Means algorithm for different values of k, the number of clusters. Then, the silhouette score was plotted as a function of k, as shown in Fig. 3.5. The optimal number of clusters, according to this criterion, is then $k = 7$. The Voronoi tessellation for this value of k, along with each cluster center, is shown in Fig. 3.6. A representative structure for each family can be found in Fig. 3.7. Here we give a description of the different structural families found, specifying the number of silver atoms m.

- 1) $m = 0-4$, $m = 100$
  These are the only six structures with Marks decahedral symmetry.
- 2) $m = 79-83$
  Five asymmetric icosahedral structures.
- 3) $m = 59-66$
  These eight nanoalloys have a 55-atom perfect Mackay icosahedron covered by an incomplete Mackay crust, which is slightly distorted and presents a small rotation.

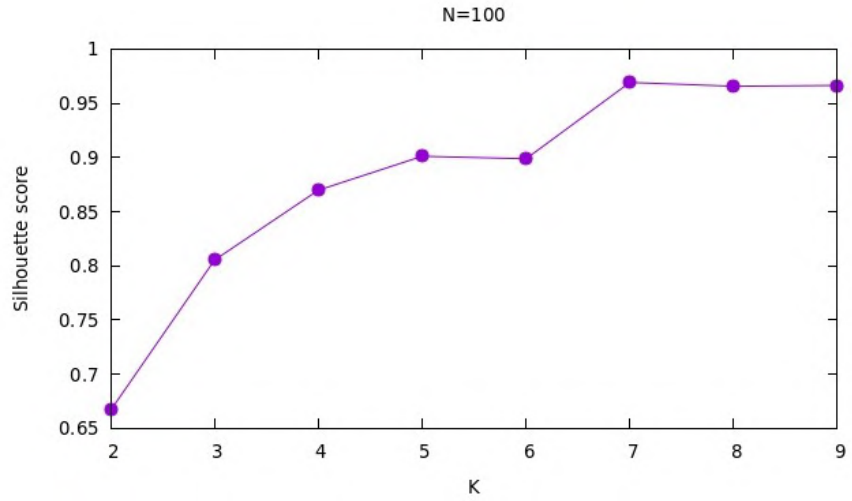

Fig. 3.5 Silhouette score as a function of k for the case $N = 100$.

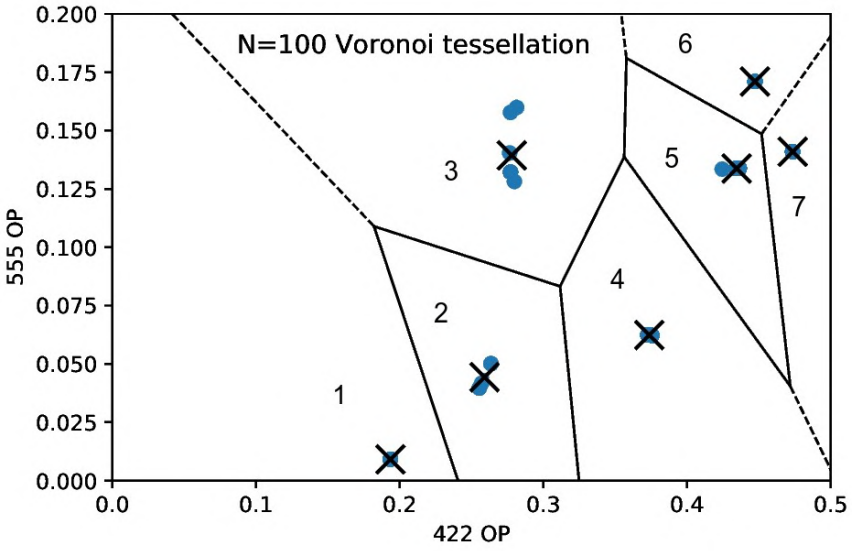

Fig. 3.6 Voronoi tessellation and cluster centers (means), for $k = 7$, when $N = 100$.

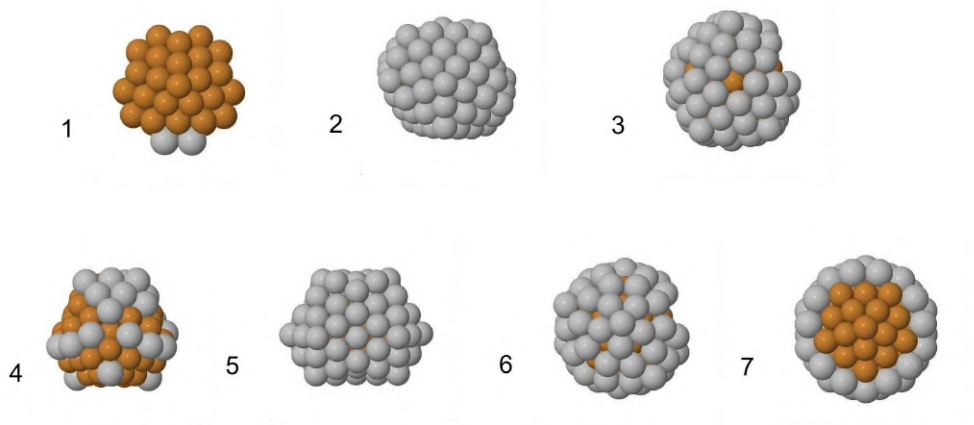

Fig. 3.7 Seven representative structures, one for each family. Labels are referred to Fig. 3.6. The seven structures represented in this figure have 2, 82, 62, 23, 72, 56 and 45 silver atoms respectively.

- 4) $m = 5 - 34$, $m = 84 - 99$
  These forty six structures, which compose the largest cluster, have icosahedral symmetry. They are basically composed of a 55-atom perfect Mackay icosahedron covered with an incomplete Mackay icosahedral shell (which is part of the surface of the 147-atom icosahedron). However, even if they share this common feature, there are two subgroups that can be identified. The first subgroup is that of $m = 5 - 34$, where the silver atoms are at the surface, typically occupying icosahedral vertices and the external shell. The second subgroup can be identified with the remaining nanoalloys. Those structures have all of their copper atoms in the core, typically forming part of the 13-atom perfect icosahedron.

- 5) $m = 67 - 78$
  These twelve structures are polyicosahedra [112] resulting from three joined 55-atom icosahedra sharing some atoms. The third icosahedron is incomplete because of an insufficient total number of atoms.

- 6) $m = 54 - 58$
  These five structures are again core-shell as those in group 4. However their crust is of anti-Mackay type [24], see Fig. 1.8. Moreover, they have part of such crust removed at the boundary and some silver atoms are placed at the fivefold vertices. We remark that this small deviation (their 422 signature differs 0.0262 from the seventh group) was detected by the clustering algorithm.

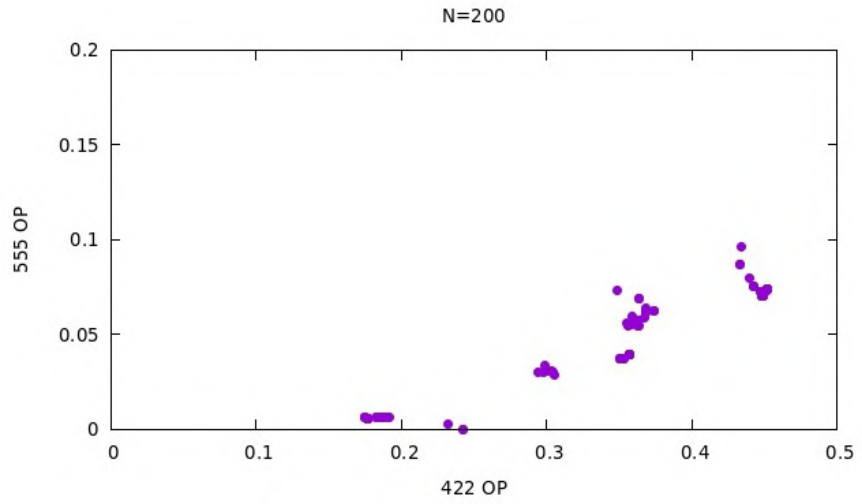

Fig. 3.8 Data set representation in the two dimensional space of 422 and 555 order parameters. For each nanoalloy, we calculated its signature 422 and 555 order parameters as the fractions of nearest-neighbor pairs presenting such signatures.

- 7) $m = 35 - 53$
  All these nineteen structures are similar for their icosahedral symmetry to those already described in group 4 and 6, however they have the 55 perfect Mackay icosahedron covered with a partial anti-Mackay crust to form a *ball-and-cup* structure [121]. Perfect symmetry is achieved when $m = 45$.

With very few exceptions, the global minima of 100-atom particles belong to some type of icosahedral family. Exceptions are found for a few extreme Cu-rich compositions and for pure Ag, where the best structures are decahedral. All structures with the lowest mixing energy are icosahedral, and the best ones (belonging to clusters 3, 6 and 7) present a 55-atom Mackay icosahedron covered either by a Mackay or an anti-Mackay incomplete shell. These results show that icosahedral and polyicosahedral structures take advantage from stress relaxation in Cu@Ag structures much more efficiently than decahedral ones.

3.2.2 N=200

The representation of these nanoalloys in the same two dimensional space described by the 422 and 555 CNA order parameters is given in Fig. 3.8. When K-Means is implemented, and the silhouette score is plotted as a function of the number of clusters k, one obtains the plot given in Fig. 3.9. The optimal number of clusters, according to this criterion, is then $k = 5$. The relative Voronoi tessellation, along with each cluster center, is shown in Fig. 3.10. A representative structure for each family is shown in Fig. 3.11. The different structural

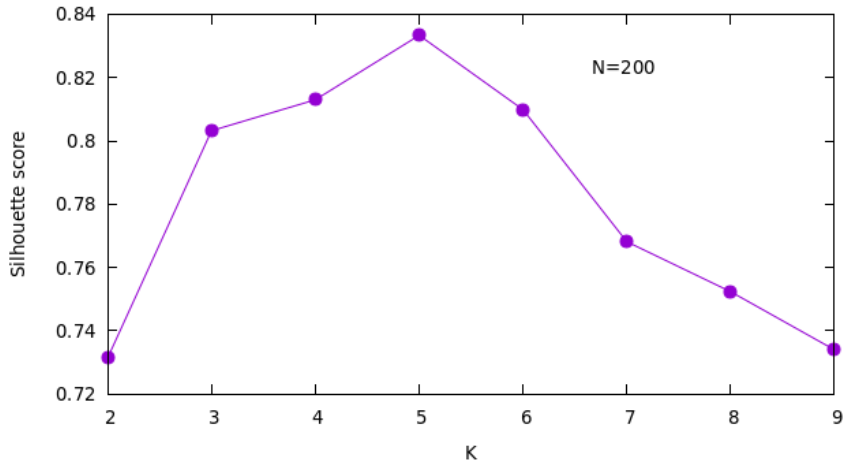

Fig. 3.9 Silhouette score as a function of k for the case $N = 200$.

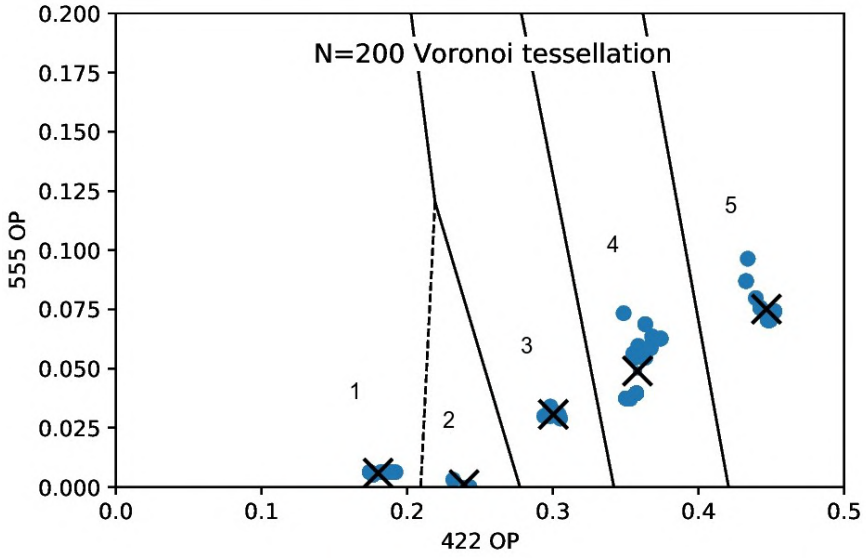

Fig. 3.10 Voronoi tessellation and cluster centers (means), for $k = 5$, when $N = 200$.

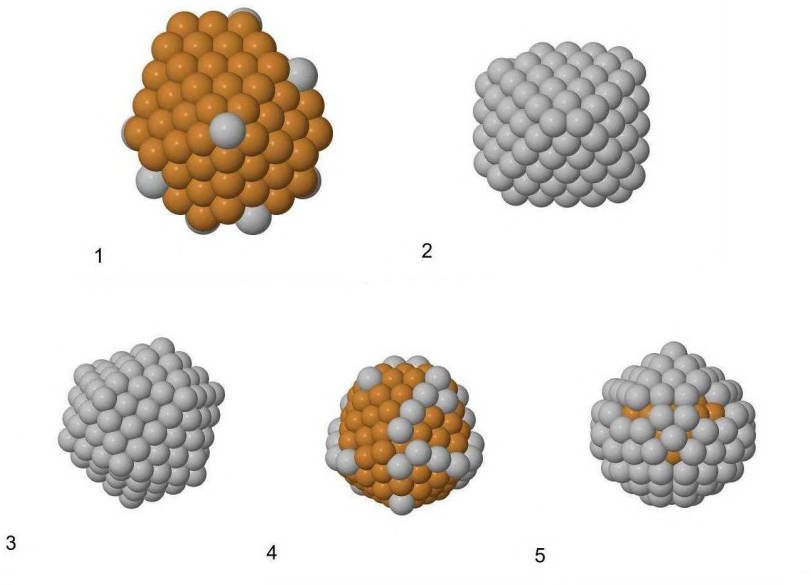

Fig. 3.11 Five representative structures, one for each family. Labels are referred to Fig. 3.10. The five structures have 10, 106, 168, 42 and 80 silver atoms respectively.

families can be described as follows:

- 1) $m = 0 - 30$, $m = 196 - 200$
  Marks decahedra. In Cu-rich decahedra, Ag atoms fill the vertices first, then they start filling (100) facets. In Ag-rich decahedra, the few Cu are atoms placed in the fivefold axis.

- 2) $m = 104 - 108$
  Core-shell fcc-hcp fragments.

- 3) $m = 160 - 174$
  Core-shell asymmetric icosahedra.

- 4) $m = 32 - 54$, $m = 102$, $m = 110 - 152$, $m = 176 - 194$
  Incomplete core-shell structures, with a Cu icosahedron of $N = 147$ atoms covered by a Mackay Ag crust. Ag atoms initially fill the vertices, and later the edges. Finally they become part of the surface of the core 147 icosahedron. Again as in the case with $N = 100$, this is the largest cluster of structures.

- 5) $m = 56 - 100$, $m = 154 - 158$
  As group 4), but with an anti-Mackay crust.

Also for size 200, a vast majority of global minima is of icosahedral structure. The exceptions are the decahedra found for Ag-rich and Cu-rich compositions and few fcc-hcp

structures at intermediate compositions. These results confirm the key role of stress relaxation in determining the most stable structures also at this larger size of 200 atoms.

3.2.3 Other choices of order parameters

In this section, we describe how clustering results are sensitive to the choice of the nanoparticle descriptors, i.e. of our 555, 422 and 421 variables. This analysis was made by using K-means, which was applied to different choices of variables besides the (522,422) choice used for the two previous examples.

First of all, we applied the clustering algorithms in the three-dimensional space of (555,422,421) signatures. Then we applied clustering in the spaces of two signatures at a time: (555,421) and (422,421) besides (555,422), and finally to one-dimensional spaces of one signature at a time, i.e. (555), (422) and (421) separately. We compared all clustering choices finding the following results:

– For size 100, only the pair (555,422) was able to reproduce exactly the same clustering as the three-dimensional description, while (555,421) and (422,421) were giving somewhat different clusters. On the other hand, the clustering obtained by one-dimensional descriptions was significantly different.

– For size 200, only the pair (422,421) was able to reproduce the same clustering as the three-dimensional description. At variance with the (555,422) description, (422,421) gave six clusters instead of five, due to the splitting of cluster 4 of Section 3.2.2 into two new clusters corresponding to Cu-rich and Ag-rich parts. These two parts differ by a small distortion of the Ag crust in the Ag-rich part which eliminates the few 421 signatures that are present in Cu-rich nanoparticles.

From these results it turned out that (555,422) and (422,421) are the best choices to capture the physically relevant clusters of the full three-dimensional description. However we note that the (422,421) pair would be unable to separate well between nanoparticles with fivefold symmetries and nanoparticles with extended hcp domains or several stacking faults. The latter were not present in our samples of global minima for sizes 100 and 200, but they may appear in samples including also higher energy isomers. For this reason we preferred the (555,422) pair as the most useful two-dimensional description.

3.2.4 $Ag_{64}Cu_{36}$

We now analyze the results obtained for the specific composition $Ag_{64}Cu_{36}$, for $N = 100$. We considered all the structures collected in the output of our three BH searches. In total, our pool consists of 309 structures. In the usual (555,422) two-dimensional space given by

the CNA signatures, the structures are arranged as shown in Fig. 3.12 (a). Given the nature of such representation (evidently more complicated than the previous two cases), we used the Gaussian Mixture Model in order to find a separation into structural families, because the Gaussian Mixture Model allows clusters to have ellipsoidal shapes (a more general and flexible hypothesis with respect to the hard tessellation found by K-Means). The BIC and silhouette scores were then plotted as a function of the number of mixture components, k, as shown in Fig. 3.13 (a) and (b). The minimum of the BIC scores dictates that the optimal separation happens when the number of components is seven. This optimal number is confirmed by the silhouette score which shows a local maximum at $k = 7$. However we must recall that the silhouette score is less and less representative as the elongation of clusters increases. Apparently then, there is a clear distinction between seven different structural families. However, after manual inspection, one finds out that the first three clusters on the left (i.e. the orange, purple and red one) comprehend a large variety of amorphous structures, making very difficult the distinction between them, even at human-eye level. The reason behind this fact is that the pool of structures is composed of various local minima, among which a large part (the majority of them, actually) is very high in energy with respect to the global minimum, and thus represents a sort of noise of non-relevant structures. A simple way to overcome this obstacle is to put an energy cutoff, reducing the number of structures of the data set. If we consider only structures which differ at most 0.5 eV from the global minimum, we obtain another representation of such nanoalloys, as shown in Fig. 3.14 (a). With such restriction, the amount of structures reduces to 90. BIC and silhouette score suggest (as expected) four clusters to be the optimal subdivision of the reduced data set, as shown in Fig. 3.13 (a) and (b). A representative structure for each family is instead depicted in Fig. 3.15.

As explained in the Introduction, the post-processing of some numerical simulations, such as the global optimizations described here, may require the clustering of the data sets for the application of other algorithms. An example, already mentioned at the beginning of this section, is now given below.

Thermodynamic informations can be extracted from global optimization results. In fact, once a set of nanoparticles structures is obtained, and the clustering procedure as described above is implemented to group them into different structural families, the probability of these groups as a function of temperature can be calculated. This quantity is very important because it tells the expected fraction of NPs having a specific structural motif that should be measured in an experiment that aims at studying the same system at a particular temperature. In order to estimate the temperature-dependent probability for the four structural families obtained in our global omptimizations of $Ag_{64}Cu_{36}$ with the energy cutoff, we implemented the Harmonic Superposition Approximation [36, 122], which is an approximation for the

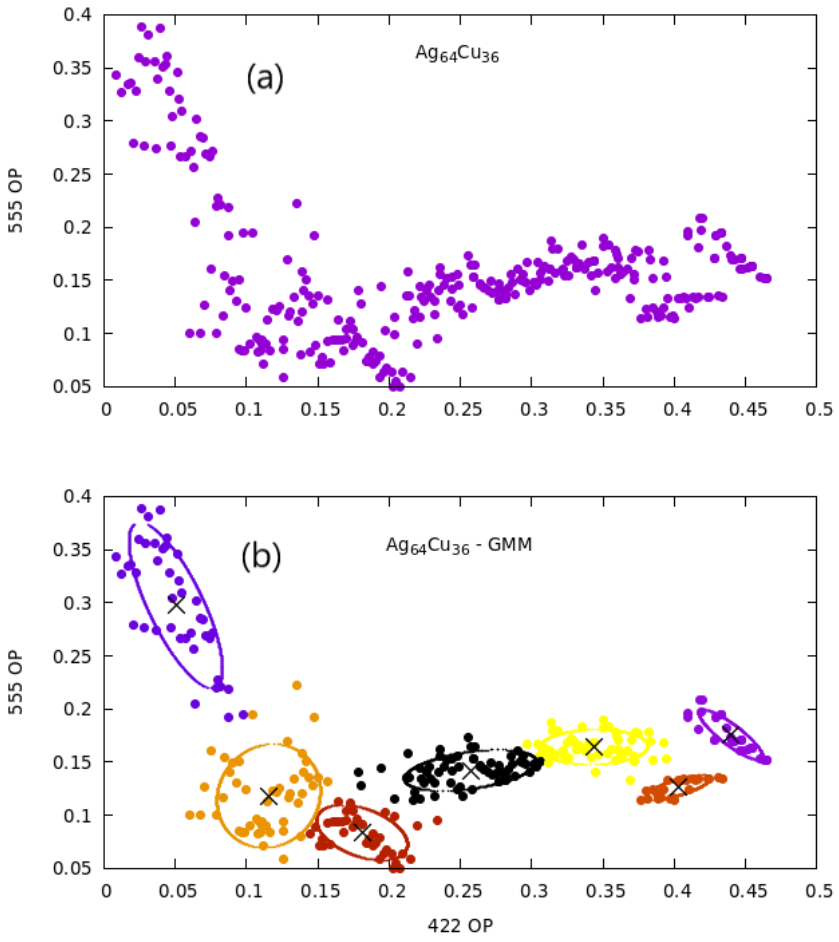

Fig. 3.12 (a) Data set representation in the two dimensional space of 422 and 555 order parameters. (b) Gaussian Mixture Model plot with centers and contours for $k = 7$ distributions. Adapted with permission from [95]. Copyright © 2023 The Authors. Published by American Chemical Society.

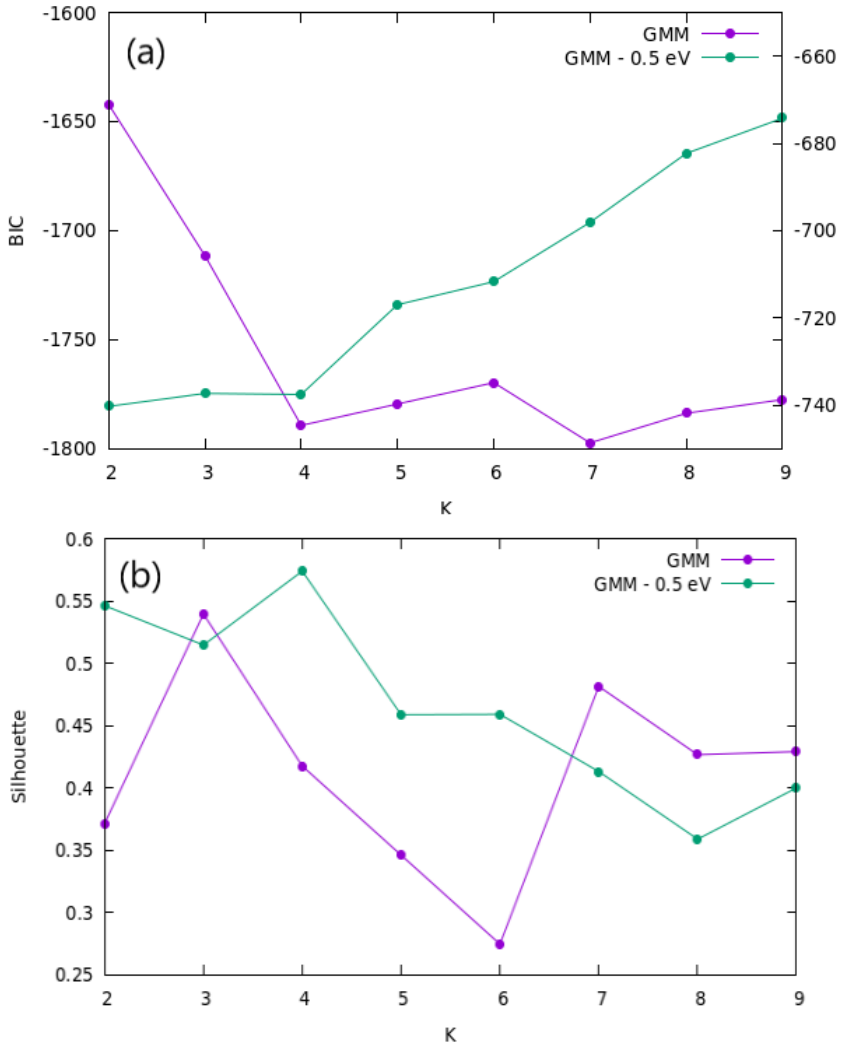

Fig. 3.13 (a) BIC and (b) silhouette scores for both full and reduced data sets. In (a) the curve for the reduced data set has the y-axis range given on the right part of the plot. Adapted with permission from [95]. Copyright © 2023 The Authors. Published by American Chemical Society.

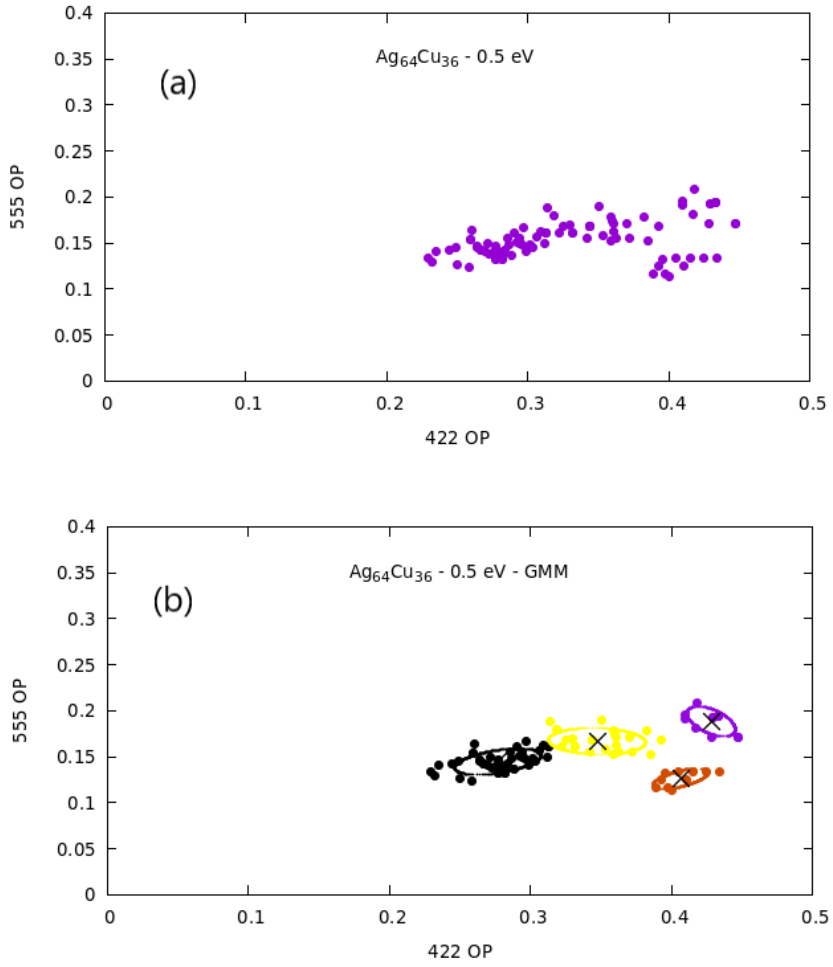

Fig. 3.14 (a) Data set representation in the two dimensional space of 422 and 555 order parameters, when the cutoff for energy is applied. (b) Gaussian Mixture Model plot with centers and contours for $k = 4$ distributions. Reproduced from Ref. [93] with permission from the Royal Society of Chemistry.

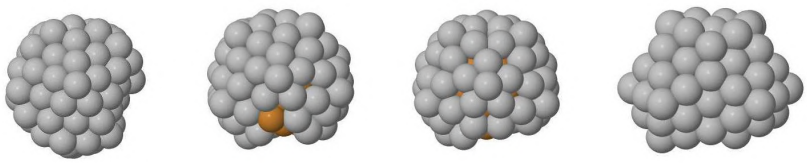

Fig. 3.15 Representative structures for the four clusters of Fig. 3.14 (b). From left to right: an icosahedron with a Mackay crust (black cluster), an icosahedron with mixed Mackay and anti-Mackay crust (yellow cluster), an icosahedron with full anti-Mackay crust (purple cluster) and a polyicosahedron (red cluster).

partition function of a system of N atoms. For a local minimum s with potential energy E_s, it is assumed that the partition function can be decomposed into translational, rotational and vibrational terms:

$$Z_s = \frac{1}{h_s} Z_s^{tr} Z_s^{rot} Z_s^{vib} e^{-\beta E_s} \tag{3.2}$$

where h_s is the order of symmetry group of the local minimum s and $\beta = 1/k_B T$, where T is the temperature of the canonical ensemble considered. In particular we have that:

$$Z_s^{tr} = V \left(\frac{M k_B T}{2\pi\hbar^2} \right)^{3/2} \tag{3.3}$$

is the translational term, where V is the volume of the box containing the nanoparticle, M the total mass;

$$Z_s^{rot} = \left(\frac{2\pi k_B T \bar{I}_s}{\hbar^2} \right)^{3/2} \tag{3.4}$$

is the rotational term, where $\bar{I}_s$ is the average moment of inertia of local minimum s: $\bar{I}_s = (I_s^{xx} I_s^{yy} I_s^{zz})^{1/3}$ and I_s^{xx}, I_s^{yy} and I_s^{zz} are the principal moments of inertia;

$$Z_s^{vib} = \prod_{i=1}^{3N-6} \frac{1}{2\sinh(\beta\hbar\omega_{s,i}/2)} \tag{3.5}$$

is the vibrational term in the harmonic approximation, where $\omega_{s,i}$ is the i-th non zero normal mode of the local minimum s. The probability as a function of temperature of the local minimum s in the ensemble is then given by

$$p_s = \frac{Z_s}{\sum_{\sigma=1}^{n_{min}} Z_\sigma}, \tag{3.6}$$

where n_{min} is the number of isomers considered in the ensemble. With this tool, it is then possible to estimate the temperature-dependent probability of the four structural families found for $Ag_{64}Cu_{36}$ with the energy restriction. The results are as shown in Fig. 3.16. Specifically, the relative probability P of family $\mathscr{F}$ is given by

$$P = \frac{\sum_{i \in \mathscr{F}} p_i}{\sum_{j=1}^{n_{min}} p_j} \tag{3.7}$$

where the sum in the numerator is restricted to the minima belonging to family $\mathscr{F}$, while the sum in the denominator extends to the minima of all families considered in the calculation. The probabilities p_i of individual minima are given by Eq. (3.6). The black curve in Fig. 3.16 suggests that the icosahedron with Mackay crust is the most favorite structural family

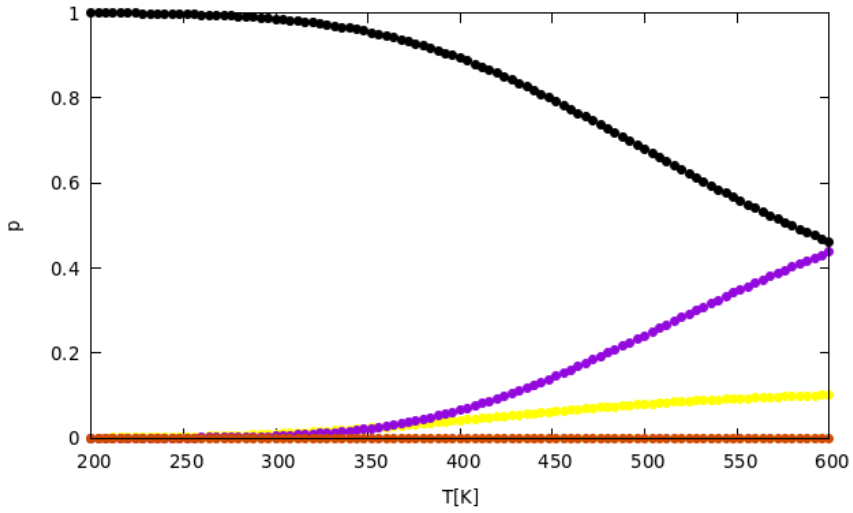

Fig. 3.16 Probability P of the different structural families as a function of temperature in the range 200-600K. P is calculated by eq. (3.7). The curves refer to icosahedra with Mackay crust (black), icosahedra with mixed Mackay and anti-Mackay crust (yellow), icosahedra with full anti-Mackay crust (purple) and polyicosahedra (red). The colors correspond to those of the clusters of Fig. 3.14 (b), while representative structures are given in Fig. 3.15. Reproduced from Ref. [93] with permission from the Royal Society of Chemistry.

(i.e. the most probable) in the relevant interval of temperature from 0 to 500 K (after which AgCu nanoalloys start melting their surface), coherently with the previous discussion on the structural properties of global minima at all compositions for AgCu nanoalloys with $N = 100$ atoms in total. Icosahedra with anti-Mackay crust are ranked second (purple curve), whereas mixed crust (yellow) and polyicosahedra (red) are ranked respectively third and fourth.

3.2.5 Discussion

Thanks to the method presented in this section, we demonstrated the possibility of solving the problem of the clustering of nanoparticles. In particular, we showed that it was possible to automatically discover the variety of structural families present in AgCu nanoalloys of sizes $N = 100$ and $N = 200$ atoms. In particular, we found that even without a previous manual classification of such nanoalloys, it is still possible to recover a physically meaningful as well as detailed separation into different clusters of structures. This result was achieved also thanks to the clever description given by the CNA signatures, which made possible the success of the machine learning algorithms used, in the two dimensional space. In order to cluster the data sets composed of the global minima for $N = 100$ and $N = 200$, we used K-Means which produced a hard partition (Voronoi tessellation) of the two dimensional space of the two order parameters relative to 422 and 555 signatures. The classification obtained by

the (555,422) pair was compared also to those obtained by using other CNA sets of variables, discussing how the classification depended on the choice of the set.

A different algorithm, the Gaussian Mixture Model, was used instead to perform the same task on a slightly more complicated case, that is the one offered by the two dimensional representation of some of the local minima found in the global minimization of $Ag_{64}Cu_{36}$. Here the superior flexibility of such algorithm with respect to K-Means was crucial to find a good separation into clusters.

The usefulness of the clustering of the minima of $Ag_{64}Cu_{36}$ was then demonstrated with an example by calculating the temperature-dependent equilibrium probabilities of the different structural families. Finally, we note that the approaches developed in this work does not rely on any specific feature of the AgCu system, so that they can be easily used to treat other nanoalloys.

3.3 Clustering nanoparticles - part II

In the previous section we described a method for the clustering of nanoparticle structures based on the CNA for the description of nanoparticles and two algorithms for the actual solution of the clustering problem. The method, though very simple and functional in some cases, has some limitations. As it was explained in section 3.2.4, the two-dimensional description given by the two order parameters is sufficient to cluster efficiently a data set made of local minima only when an energy cutoff is applied to it. We found similar problems for MD simulations at constant temperatures near the melting temperature, for which many different disordered structures are part of the output of the simulations. Also in this cases, GMM was not sufficient to capture correctly the different structural motifs, so that an energy cutoff was needed to achieve better results. However, such constraint should be removed in order to build a method valid in as many cases as possible, disregarding the particular type of simulations by which the structures were produced.

In this section we describe the second procedure for tackling the problem of the clustering of nanoparticles, published in Ref. [95], which aimed at solving these issues. Also in this case, the very first step is the creation of the data sets. For this procedure we considered structures obtained both by global optimization searches and molecular dynamics runs. The details of these simulations are reported at the beginning of each section dedicated to the specific system under consideration. Once obtained, data sets were transformed by means of the second CNA description, explained in section 3.1, which defines a 64-dimensional vector for each nanoparticle. Then, PCA was used to map the data set into a three or four dimensional space, i.e. by using the first three or four principal components. In fact, we

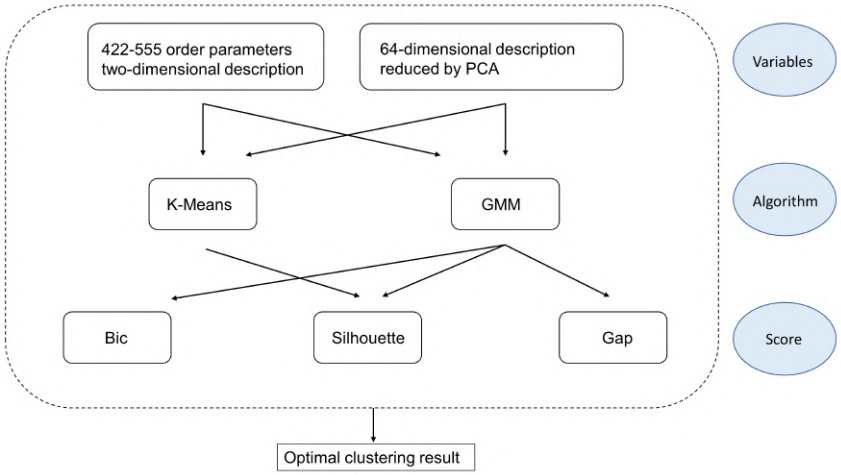

Fig. 3.17 Workflow scheme for the Machine Learning analysis. Reprinted with permission from [95]. Copyright © 2023 The Authors. Published by American Chemical Society.

found most of the times that this number of components is enough to preserve more than 90% of the entire variance of the data set, i.e. to preserve, at least to some extent, the information encoded in the 64-dimensional space defined by CNA. Finally, clustering algorithms and scores were applied to find the underlying structural families inside the data sets. In particular, the scheme adopted was the following (see Fig. 3.17 for a schematic representation of the workflow): first, a range for the number of cluster k was chosen, then for each k the model (GMM or K-Means) was fitted using 50 random initializations, the best result out of these 50 was kept and the score (silhouette, Bic or gap statistic) was calculated. The best value for the score in the range was then saved. The whole operation was repeated for a total of 50 times. Finally, the optimal number of clusters was deduced by looking at the most frequently chosen best score in the related histogram.

The need of running a certain number of independent calculations is due to the fact that, as already mentioned in section , the iterative algorithms used for solving problems (2.26, 2.27) may reach a local optimum. We have seen that, most of the times, fifty runs are enough to single out one result among the others, still without increasing too much the overall computational time.

3.3.1 AgCu, N=100 and N=200, again

We first considered the data set of Ref. [93], where AgCu nanoalloys with sizes $N = 100$ and $N = 200$ were globally optimized for different compositions. This set consists of $n = 101$ structures for both sizes. The results for AgCu nanoalloys with $N = 100$ already published in that reference are recovered with some modifications. In particular, the seven clusters found

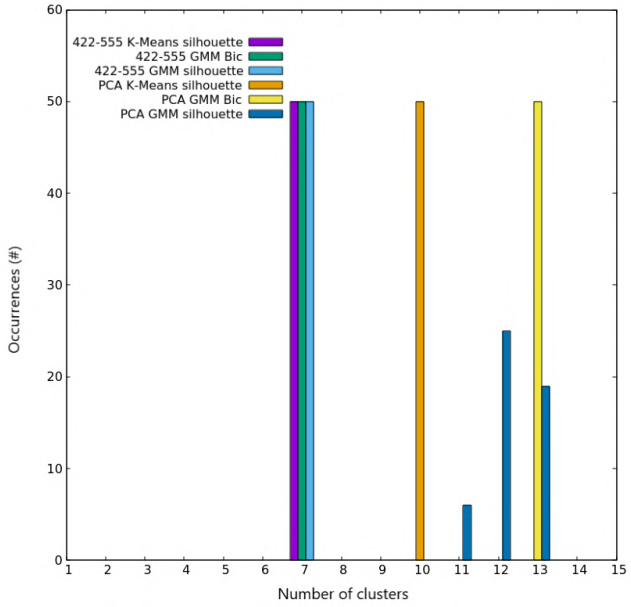

Fig. 3.18 Clustering scores for AgCu nanoalloys with $N = 100$. Occurrences of the best number of clusters out of the 50 independent trials, as given by silhouette and Bic scores for both K-Means and GMM algorithms on the two different spaces used for describing nanoparticles. Reprinted with permission from [95]. Copyright © 2023 The Authors. Published by American Chemical Society.

there were again found as the optimal separation by both K-Means and GMM on the 422-555 space, as shown in Fig. 3.18. The implementation of the 64-dimensional description of these nanoalloys and the subsequent application of PCA led us to use the first four principal components, explaining 94.8% of the variance, since the first three explained 89.4%. In this space, the two algorithms found a higher number of clusters as the best possible separation of data. In particular, the best silhouette score for K-Means is found for $k = 10$ in all cases (see again Fig. 3.18), whereas for GMM the best number of clusters was found to be $k = 13$ and $k = 12$ for the Bic and silhouette score respectively, as it can be seen in the same figure. Manual inspection revealed that these clusters were obtained by splitting into smaller clusters some of the seven previously found. An example of this cluster subdivision can be seen in Fig. 3.19, where the $N = 100$ AgCu polyicosahedral cluster (labelled as cluster (5) in section 3.1 of Ref. [93]) is split in two sub-clusters that differ in the displacement of one surface atom only.

Similarly, the five clusters found in the same reference for $N = 200$ were again recovered with eventually some further splitting. Using the 422-555 space, the silhouette scores of K-Means and GMM pointed out $k = 5$ and $k = 4$ respectively as the optimal number of clusters (see Fig. 3.20), whereas the Bic score of GMM did output more frequently $k = 10$

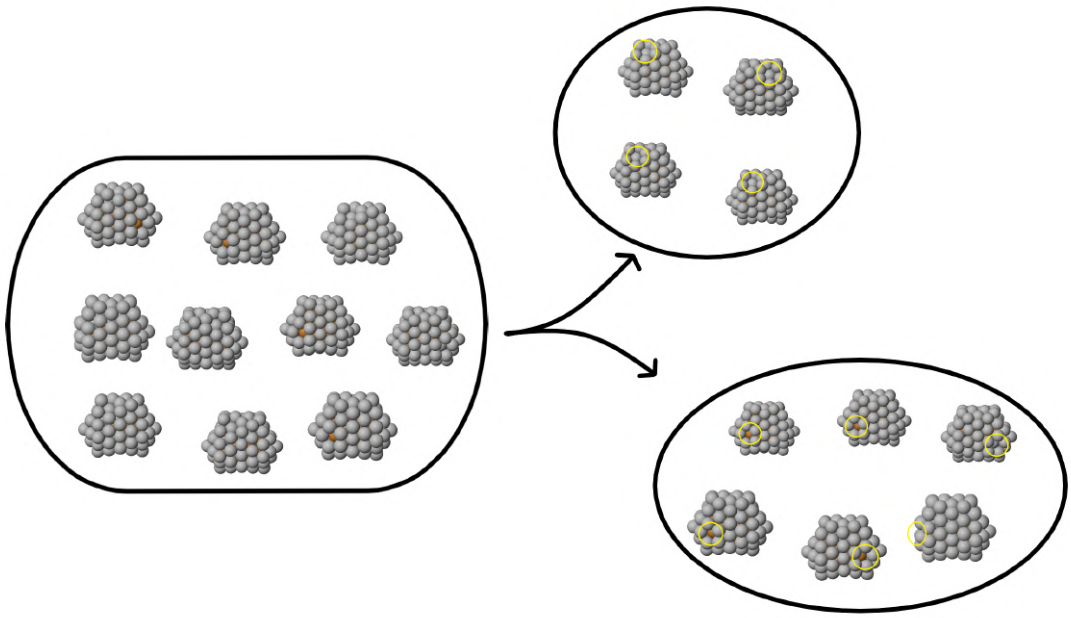

Fig. 3.19 Subdivision of the $N = 100$ AgCu cluster of polyicosahedral structures. The two clusters on the right only differ for the displacement of one surface atom. In particular, the four nanoparticles in the top cluster miss an atom in vertex position in their higher part, whereas the six nanoparticles in the bottom cluster also miss an atom in vertex position, but in their lower part. These missing-atom positions are highlighted by yellow circles. Reprinted with permission from [95]. Copyright © 2023 The Authors. Published by American Chemical Society.

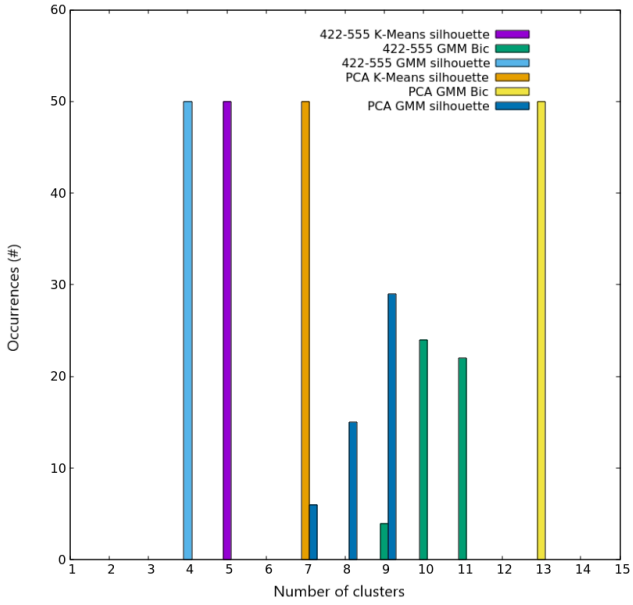

Fig. 3.20 Clustering scores for AgCu nanoalloys with $N = 200$. Occurrences of the best number of clusters out of the 50 independent trials, as given by silhouette and Bic scores for both K-Means and GMM algorithms on the two different spaces used for describing nanoparticles. Colors are explained in the inset. Reprinted with permission from [95]. Copyright © 2023 The Authors. Published by American Chemical Society.

as the optimal number of clusters. These clusters are split even further by the application of GMM on the three-dimensional space given by PCA, which in this case explains 90.7% of the variance of the data set. Here, the Bic score is minimized unambiguously for $k = 13$, as shown again in Fig. 3.20. A smaller number of clusters is instead found by the application of the silhouette score both for K-Means and GMM, giving $k = 7$ and $k = 9$ respectively, as shown in the same figure.

3.3.2 AuPd, N=250

From data sets of Ref. [19], a total number of 84 structures obtained from the global optimization of AuPd nanoalloys at size $N = 250$ and different compositions was collected. In our previous work [19], this data set was manually divided into five different groups: fcc, Dh, and three types of Ih, corresponding to different surface reconstructions (see Fig. 3.21).

Using the two-dimensional description of 555 and 422 signature order parameters, we found that K-Means and GMM silhouette scores are maximized for $k = 3$ (Fig. 3.22), whereas the Bic score calculated after the GMM fit is minimized when $k = 6$. When $k = 3$, the clusters found show Dh, fcc and Ih motifs. On the other hand, when $k = 6$, the whole icosahedral cluster is split in four sub clusters. In particular, the three icosahedral groups represented

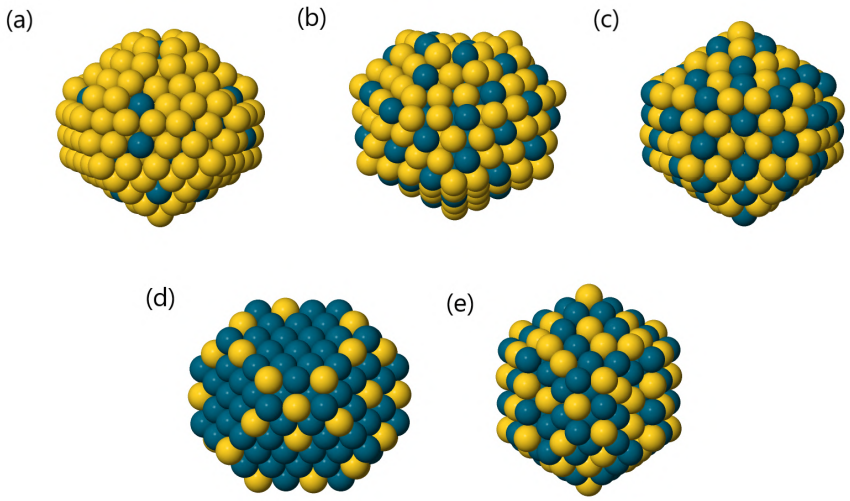

Fig. 3.21 The five different structural motifs for AuPd nanoalloys global minima with $N = 250$: (a) first icosahedral motif (b) second icosahedral motif (c) third icosahedral motif (d) fcc motif and (e) decahedral motif. Reprinted with permission from [95]. Copyright © 2023 The Authors. Published by American Chemical Society.

in Fig. 3.21(a,b,c), i.e. those that were already been discovered manually, are recovered; moreover, the first one is split in two groups.

When the 64-dimensional description is implemented and clustering is performed after PCA, which explains 98.7% of the variance of the entire data set, different results are obtained. The silhouette score related to the K-Means fit dictates that the optimal number of clusters should be again $k = 6$ (see again Fig. 3.22). This separation into six clusters on this space is very similar (almost identical) to that found by GMM on the 422-555 signature order parameters space. However, when GMM is implemented, the Bic score points out $k = 14$ as the optimal number of clusters (Fig. 3.22) whereas the silhouette score is maximized most of the times for $k = 9$ (Fig. 3.22); the gap statistic prefers instead $k = 13$ (Fig. 3.22). This result can be regarded as an example of overfitting. For instance, the thirteen groups found by GMM are obtained by dividing into smaller parts the first and second icosahedral groups. However, the difference between these clusters is so little that it is almost unnoticeable. This does not mean that the clustering result is wrong, rather it is almost too precise for our purpose. A possible reason for this is that when dealing with such data sets, which have a lot of similar, if not identical, structures, and the description is really detailed (even if the original 64-dimensional space has been mapped in a three-dimensional one that preserves its variance) then little departures from tightly-bound clusters have a good chance to be considered as clusters themselves.

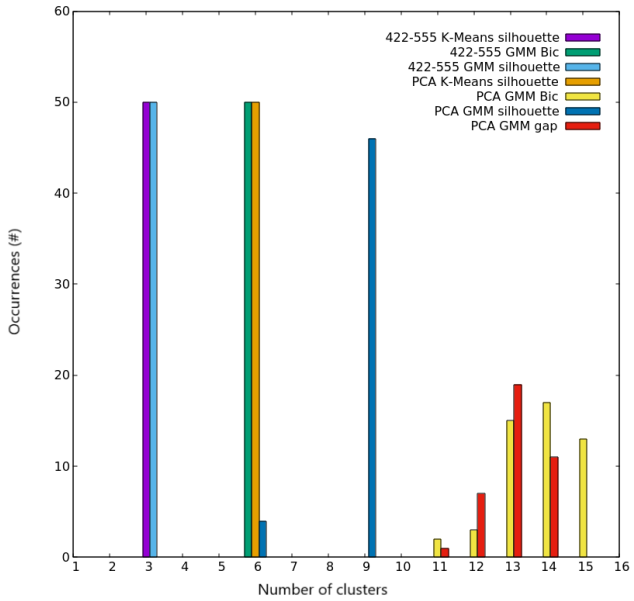

Fig. 3.22 Clustering scores for AuPd nanoalloys with $N = 250$. Occurrences of the best number of clusters out of the 50 independent trials, as given by silhouette, Bic and gap scores for both K-Means and GMM algorithms on the two different spaces used for describing nanoparticles. Colors are explained in the inset. Reprinted with permission from [95]. Copyright © 2023 The Authors. Published by American Chemical Society.

These two first systems considered, namely AgCu and AuPd, showed that for nanoalloy structures obtained after global minimization searches, it is possible to use different clustering approaches to perform a good separation into distinct geometrical families. Our results show that there are no wrong clustering choices. Rather, different descriptions or scores can lead to a more refined partition of the initial ensemble, resulting in a higher number of clusters found. We would like to remark that such possibility is a consequence of the nature of the data set and also of the algorithms/scores employed. As long as there are no wrong intersections between clusters, such refined solutions should not be considered as a drawback of the scheme since they only offer a more detailed version of a result that can be already obtained with a coarser description and less flexible algorithms. We observe that the results obtained on the data set of AuPd confirm that the first procedure presented in the previous section is a very good method when it comes to clustering data sets built from global optimizations at different compositions.

In the next sections we describe the results obtained for systems and data sets in which the simpler method offered by our fist proposed procedure does not give acceptable results anymore, and in which the second method that we described is instead capable of finding good clustering solutions.

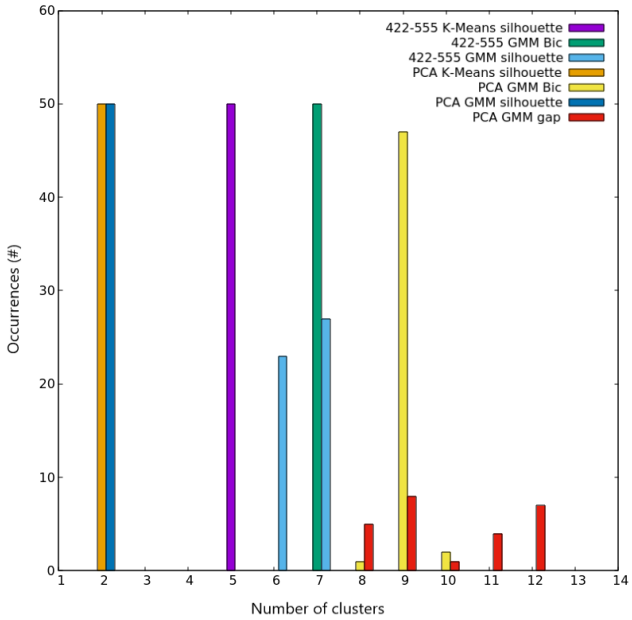

Fig. 3.23 Au_{309} clustering scores. Occurrences of the best number of clusters out of the 50 independent trials, as given by silhouette, Bic and gap scores for both K-Means and GMM algorithms on the two different spaces used for describing nanoparticles. Colors are explained in the inset. Reprinted with permission from [95]. Copyright © 2023 The Authors. Published by American Chemical Society.

3.3.3 Au, N=309 and N=315

We first considered a data set composed of about six hundred structures sampled from a molecular dynamics trajectory of 1μs for Au_{309} at 590K, near the melting temperature. This choice guarantees that, during the whole simulation, i) different structural motifs are visited due to the fluctuations induced by the high temperatures and that ii) several disordered structures showing a partial melting of the surface or even a total melting are collected. In this way, the constructed data set allows to seriously challenge our clustering procedures. By implementing PCA, we discovered that the three principal components explain 99.3% of the entire variance of the set. As anticipated, the combination of K-Means and silhouette score was not good enough to cluster the nanoparticles in this case, since the suggested number of clusters is $k = 2$ for all trials (see Fig. 3.23), which is wrong. Instead, when the GMM was fitted, the Bic score dictated that the optimal number of clusters is $k = 9$, see Fig. 3.23, and the same number was also singled out by the gap statistic.

The result of such separation can be seen in Fig. 3.24(a,b), where points in the three dimensional space given by PCA are colored differently for each cluster.

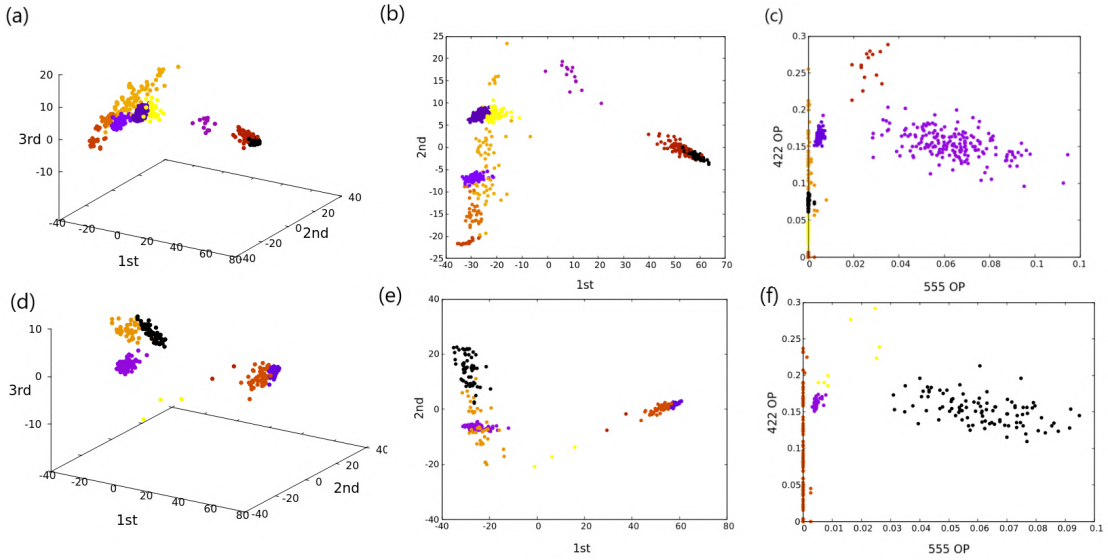

Fig. 3.24 (a) $k = 9$ clusters for Au_{309} obtained with GMM in the three-dimensional space given by the PCA. All axis are labelled with the corresponding principal component. Different colors refer to different clusters. (b) Projection of the same data along the first two principal components. (c) $k = 7$ clusters for the same data set obtained with GMM in the two-dimensional space given by 422 and 555 signatures order parameters. (d) $k = 7$ clusters for Au_{315} obtained with GMM in the three-dimensional space given by PCA. All axis are labelled with the corresponding principal component. Different colors refer to different clusters. (e) Projection of the same data along the first two principal components. (f) $k = 4$ clusters for the same data set obtained with GMM in the two-dimensional space given by 422 and 555 signatures order parameters. Reprinted with permission from [95]. Copyright © 2023 The Authors. Published by American Chemical Society.

Manual inspection of the nine clusters revealed that, in most cases (in general, since any clustering algorithm solution may not be perfect, one should always consider a chance to get some structures belonging to the wrong structural family), they contain the following structures:

- twin structures.
- fcc fragments with two ore more islands on stacking fault or defected/faulted/asymmetric twin structures. This cluster is the most spread out among others, thus it is the one characterized by a higher degree of diversity between its elements.
- icosahedral fragments.
- decahedra.
- fcc fragments with one or two islands on stacking fault. Also this cluster is quite blurred, revealing why it contains both structures with one or two stacking fault islands.
- fcc fragments with no stacking faults.
- decahedra with some surface defects or small disordered regions.
- liquid/amorphous structures.
- liquid/amorphous structures with a higher percentage of not-classified atoms.

A representative structure for each cluster can be found in Fig. 3.25.

When GMM was fitted instead on the two-dimensional space given by 422 and 555 signature order parameters, the optimal number of clusters which minimized the Bic score and maximized the silhouette score was $k = 7$ (see Fig. 3.23). These seven cluster are equal to those previously found, except for the two decahedral cluster which are merged into a single one as well as the two liquid clusters. On the same space, K-Means found an optimal separation of data into $k = 5$ clusters; however, this tessellation leads to a wrong intersection of different structural families (such as Dh with fcc, liquid with Ih, etc) and therefore it was discarded.

These results showed that in this case there is only a little gain in using the three principal components of the 64-dimensional CNA space, since a good clustering result is already achieved by using GMM on the two-dimensional space given by 422 and 555 signatures order parameters. However, the same conclusion does not hold for the case $N = 315$, as we now describe.

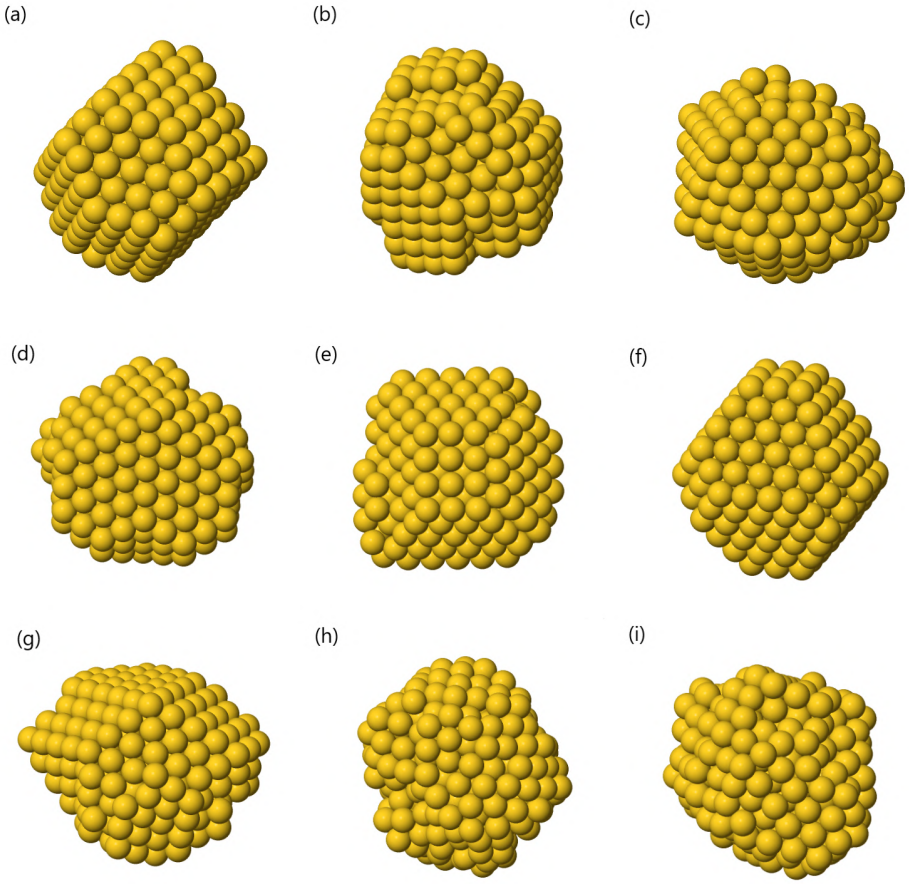

Fig. 3.25 Au_{309} representative structures for the $k = 9$ clusters found by GMM in the three dimensional space given by PCA, together with the Bic score. (a) Twin structure, (b) fcc fragment with many stacking fault islands, (c) icosahedral fragment, (d) decahedron, (e) fcc fragment with a few faults, (f) fcc fragment with no faults, (g) decahedron with disordered region on the surface, (h) liquid structure, (i) another liquid structure. Reprinted with permission from [95]. Copyright © 2023 The Authors. Published by American Chemical Society.

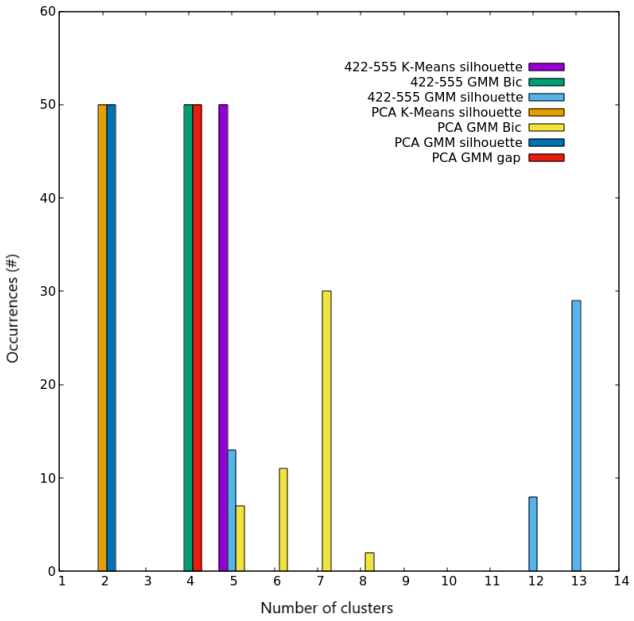

Fig. 3.26 Au_{315} clustering scores. Occurrences of the best number of clusters out of the 50 independent trials, as given by silhouette, Bic and gap scores for both K-Means and GMM algorithms on the two different spaces used for describing nanoparticles. Colors are explained in the inset. Reprinted with permission from [95]. Copyright © 2023 The Authors. Published by American Chemical Society.

In this case, $n = 300$ structures from a Au_{315} MD simulation at 590K were analyzed with both methods. Here, the combination of PCA and GMM singled out seven different structural motifs (see Fig. 3.26), including icosahedra, decahedra, liquid structures and different kind of fragments, with very similar structures as shown in in Fig. 3.25. Differently from before, the application of GMM in the 422-555 space was not as successful, finding four groups with some wrong intersections of structural motifs (see Fig. 3.26) and Fig. 3.24(f)). We note that in this case the gap statistic was not able to single out a good number of clusters for this system.

It is now clear from these two examples that for such data sets, it is possible that a simple description of NPs as the one given by the two 422 and 555 order parameters signatures may not be good enough to allow the clustering algorithms to find a good separation of structures. Instead, the application of GMM after the dimensionality reduction given by PCA was good for both cases, as long as the Bic score was used.

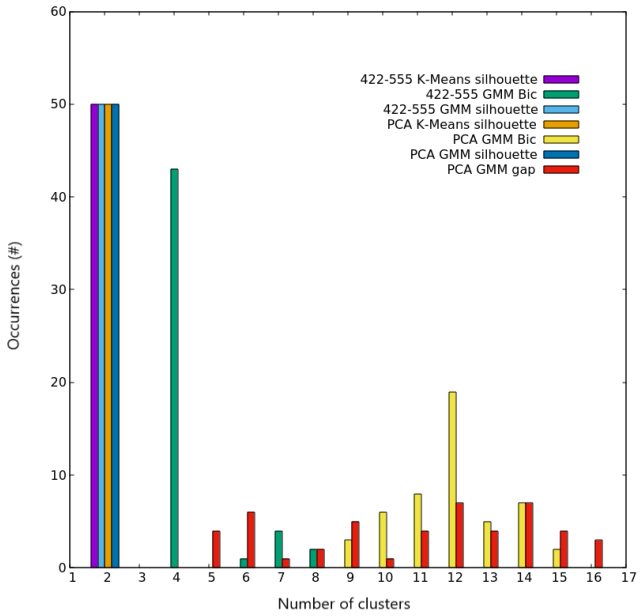

Fig. 3.27 Ag_{147} clustering scores. Occurrences of the best number of clusters out of the 50 independent trials, as given by silhouette, Bic and gap scores for both K-Means and GMM algorithms on the two different spaces used for describing nanoparticles. Colors are explained in the inset. Reprinted with permission from [95]. Copyright © 2023 The Authors. Published by American Chemical Society.

3.3.4 Ag, N=147

About three hundred structures from a Ag_{147} MD simulation at 650K were given as an input to the two clustering approaches. The three principal components were able to explain 99.3% of the variance. In this case, the minimization of the Bic score for the PCA+GMM procedure dictated that the optimal number of clusters is $k = 12$ (see Fig. 3.27), which is also preferred by the gap score, together with $k = 14$. We note that for this data set, both K-Means and GMM failed to find a good clustering results on both spaces, when the silhouette score was used.

In this data set there are no fcc fragments; among these twelve clusters, the algorithm was able to distinguish between liquid structures, different kind of fragments and some variations on an icosahedral theme. Among those variations there are icosahedra with different surface reconstructions, such as regular rosettes [123], distorted rosettes, surface defects and one, two or more than two missing vertexes. A representative structure for each cluster can be seen in Fig. 3.28.

The application of GMM and Bic on the 422-555 space dictated instead that the optimal number of clusters should be $k = 4$. Manual inspection of these four clusters revealed that this procedure was able to single out liquid structures, fragments with also some liquid

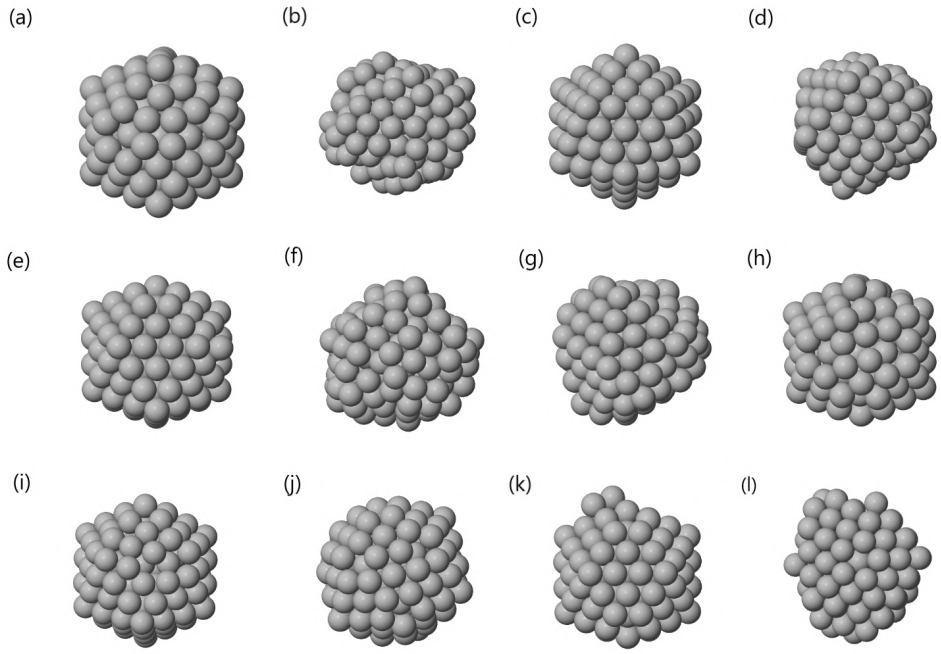

Fig. 3.28 Ag_{147} representative structures for the $k = 12$ clusters found by GMM in the three dimensional space given by PCA, following the indication of the Bic score. (a) Icosahedron with rosettes, (b) liquid structure, (c) perfect Mackay icosahedron, (d) icosahedral fragment, (e) icosahedron without one vertex, (f) other liquid structure, (g) other kind of fragment, (h) icosahedron with distorted rosettes, (i) icosahedron with surface defects, (j) icosahedron without many vertexes and (k) icosahedron without two vertexes and (l) decahedral fragment. Reprinted with permission from [95]. Copyright © 2023 The Authors. Published by American Chemical Society.

and icosahedral structures, and two groups of icosahedra, which contain all those already described above. Essentially, this result can be regarded as a coarser division of Ag_{147} NPs in a smaller number of groups, with again some wrong intersections between these groups.

Evidently, also in this case the application of this procedure based on a more detailed description of NPs together with a reduction of the high-dimensional space was effective in detecting clusters thanks to the employment of GMM and Bic score.

3.3.5 Au, N=100

Another challenging system to analyze is that of Au_{100} molecular dynamics at 420K. At this temperature, which is just below the melting point for this size, the evolution of such a small system is very complicated since there are frequent fluctuations between isomers with comparable energy but very different and complicated structural motifs [124]. Moreover, these fluctuations are not always stable, as some of these isomers only last few nanoseconds during the MD run. Here, the Gaussian Mixture Model on the three-dimensional space given by the principal components analysis minimized the Bic score when $k = 8$, whereas the gap score prefers $k = 7$ (see Fig. 3.29). The result was quite good, since the clustering procedure was able to automatically distinguish between decahedra, bi-decahedra, fcc fragments, faulted fcc fragments, twin structures and some poly-icosahedra.

Also in this case, the K-Means algorithm was not able to discover a good separation of data on both spaces. Similarly as before, the GMM on the 422-555 found out $k = 6$ clusters that are partially overlapped, due to the high presence of different isomers in this sample.

3.3.6 Discussion

Through all the results presented here, a comparison between different choices of algorithms, variables and scores was made in order to single out the most effective clustering methodology.

In general, we have experienced that data sets composed of structures obtained by global optimizations are well described both by the two-dimensional space given by the 422 and 555 signatures order parameters and by the first principal components of the 64-dimensional space described above, meaning that in these spaces there is a good chance to obtain tightly bound clusters that are simple to identify. In these cases, K-Means and GMM are reliable tools to cluster the data set, and both silhouette and Bic score can be used to evaluate the optimal number of structures. However, in global optimizations searches, there may be a tendency to produce very close points in such spaces, or even identical points when, for example, two nanoalloys with different compositions share exactly the same geometrical

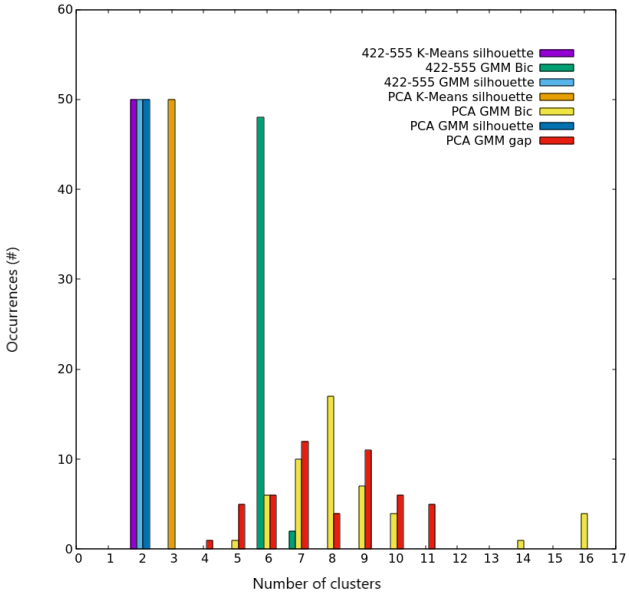

Fig. 3.29 Au_{100} clustering scores. Occurrences of the best number of clusters out of the 50 independent trials, as given by silhouette, Bic and gap scores for both K-Means and GMM algorithms on the two different spaces used for describing nanoparticles. Colors are explained in the inset. Reprinted with permission from [95]. Copyright © 2023 The Authors. Published by American Chemical Society.

shape and so the same vector of CNA signatures. In these cases clustering algorithms may overfit the data set. When this is the case, the score outputs an optimal number of clusters which is greater than the "real" one, meaning that the precision by which clustering is carried out to divide the data set is too high even for being detected and/or appreciated at human-eye level. This scenario is realized for example when the Bic score has a high value in the log-likelihood term in eq. (2.29), which, in turn, shifts the position of the minimum in the high range of k. We note that this possibility should not be considered as a real drawback, but rather as a opportunity to obtain a more refined grouping of structures.

On the other hand, structures obtained by MD simulations offer much more complex scenarios, since they usually involve fluctuations of structures and even amorphous/liquid-like NPs (especially if, for a given size, the simulation runs at a sufficiently high temperature). Moreover, due to the nature of physical trajectories, evolution within these structural motifs are followed with a certain degree of continuity. Thus, in the two spaces defined by CNA order parameters and PCA, all the structures are projected in much more elongated and blurred distributions, with respect to global optimizations, resulting in a much more difficult clustering problem, especially for smaller NPs sizes (i.e. for higher surface to volume ratios). We found that, in these cases, K-Means usually fails to perform a good clustering and that

even GMM often poorly performs on the 422 and 555 signatures order parameters space, whereas it still gives good results on the PCA reduced space. For the same reason, also the silhouette score becomes less and less representative with increase in elongation and blur, so that, if one has to resort to a single score, the Bic score becomes the most suitable choice.

In summary, we presented a scheme for clustering the structures of metal nanoparticles based on a combined approach of Common Neighbor Analysis and of Machine Learning. By analyzing several examples of increasing structural complexity, we showed that the most effective strategy consists of three steps: (i) using a high-dimensional description of the local environment of each atom in the nanoparticle; (ii) reducing the dimensionality of the description by means of the Principal Component Analysis (PCA); (iii) clustering in the reduced space by virtue of the Gaussian mixture model (GMM) and assigning the scores by the Bayesian information criterion (Bic). The workflow of this scheme is represented in Fig. 3.30.

We believe that this scheme could be used for different applications involving the problem of the clustering of nanoparticle structures given their atomic coordinates, thus acting as a starting point for the analysis of data sets of different complexity. The most evident application involving the problem of the clustering of nanoparticles is the analysis of a data set that includes different geometrical structures, which has served as the main motivation for our work. In practice, this is always the case for global optimization searches and molecular dynamics simulations. In fact, any MD simulation of interest has at least one atom diffusing inside the nanoparticle or on its surface, thus creating a variety of closely related structures (otherwise if nothing happens - for example if the temperature is low - the nanoparticles always looks the same and there is no need for clustering). Other types of simulations are for example those examined in this chapter, in which, at a sufficiently high temperature, nanoparticles are allowed to fluctuate between different isomers. Another type of simulation that was not considered here (but that would not change the substance of our work) is that of a solid-liquid transition, in which temperature is increased by a given rate. At some point the nanoparticle undergoes a transition towards the liquid state, so that the analysis of the different structural types explored by the simulation could be of some interest. Finally, another application is that involving the calculation of probabilities for the different structural families as a function of temperature. This can be done for example by applying the Harmonic Superposition Approximation, which allows to compute the partition function of a nanoparticle in the canonical ensemble. From this, one can go back to the temperature-dependent probability of a particular structural family. The procedure was explained in detail in section 3.2.4 and implemented in one of our data set to give a working example.

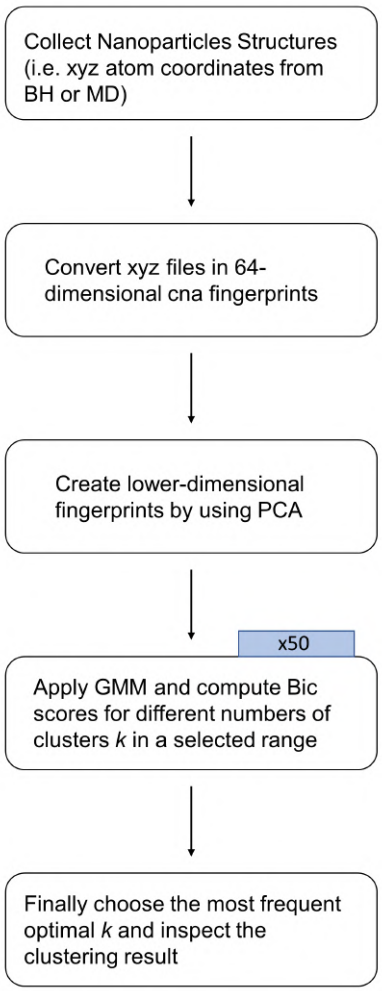

Fig. 3.30 Our scheme workflow described in blocks. Reprinted with permission from [95]. Copyright © 2023 The Authors. Published by American Chemical Society.

Chapter 4

Optimizing the shape and chemical ordering of nanoalloys with specialized walkers

In Chapter 2 we described the Basin Hopping algorithm in its standard form, that we used for almost all the results regarding global optimizations that are presented in this thesis. Here in this chapter, we describe two new algorithms for the optimization of nanoalloys that we developed. These results were published in Ref. [125]. The new algorithms are based on the concept of multiple Basin-Hopping walkers running in parallel, each with its own specialized task – the *flying* walker, exploring the energy landscape at high temperatures to sample different geometric structures, and the *landing* and *hiking* walkers, mainly refining the optimization of chemical ordering at low temperatures. In the following, these algorithms will be referred to as Flying-Landing (FL) and Flying-Landing-Hiking (FLH). We tested the two algorithms against several benchmarks (AuCu and AuRh clusters of 400 atoms and PtNi clusters of 38 and 55 atoms). In all cases, it is demonstrated that both FL and FLH perform very well compared to previous results in the literature. In addition, the algorithms were applied to the optimization of larger nanoalloys, with sizes up to 4000 atoms, in order to establish the behavior of the mixing energy and to compare full global optimization of shape and chemical ordering with optimization of chemical ordering alone at fixed shape. In general, our results show that the simultaneous optimization of shape and chemical ordering is necessary in many cases, and that the FLH approach is especially efficient for that purpose.

As discussed in Chapter 2, the search for the global minimum of a function of many variables is a long-standing open problem. Due to its intrinsically complicated nature, there is no choice of attempting any analytical calculation; in practice, this problem can be tackled by numerical techniques only. The two key questions that any global optimization technique

always needs to answer to, are the following:
i) How broad is the exploration of the high-dimensional space in which the function is defined?
ii) How fast is the convergence to the global minimum?
Any algorithm that is in charge of finding the global minimum of any function, should be able to look for as many different relevant portions of that space as possible, i.e. to perform a wide exploration of the energy landscape [126]. In addition, the algorithm must be able to go deep down in the relevant regions of the landscape, thus performing an efficient exploitation [126]. Several approaches have been recently proposed to deal with these issues [127–132]. Regarding question ii), we note that, in general, any global minimum found by any optimization algorithm is for sure a global miminum only if it would be possible to compare it to all the other local minima of the function. Therefore, since it is virtually impossible to find all local minima of a function with more than a few variables in a reasonable amount of time, the global minimum found after a global optimization search is only a putative one.

Global optimization is a very challenging task already for one-component (elemental) nanoparticles due to the enormous number of local equilibrium configurations (i.e. of local minima) of the potential energy surface, which is expected to exponentially increase with the number of atoms N [133–135]. These local minima correspond to different geometric structures which in principle can present quite different properties. The global optimization problem is even more complex for binary and multi-metallic systems. In fact, in these systems, the geometric shape as well as the chemical ordering have to be optimized. The optimization of the chemical ordering is challenging because of the enormous number of permutational isomers (often referred to as *homotops* [136, 137]).

In this chapter we introduce two new algorithms that are specifically designed for the global optimization of bi-metallic nanoparticles. The new algorithms improve upon the basin hopping algorithm previously developed in Refs. [55, 107], which was favorably tested for the optimization of nanoalloys of sizes up to a few hundred atoms [108]. We show that these algorithms perform very well when compared to our previous multi-temperature Basin-Hopping scheme [108] and to other algorithms proposed recently in the literature [44].

The material of this chapter is organized as follows. In section 4.1 we describe in details the two new algorithms. In section 4.2 we discuss the results obtained on the chosen systems. Finally, in the last paragraph, we address the conclusions of this work. My main task in this work was to analyse and organise the material of the global optimization searches.

4.1 Description of the algorithms

In this section, we describe the FL and FLH algorithms. In the FL algorithm, there are two basin-hopping walkers, the *flying walker* (fw) and the *landing walker* (lw). The fw evolves by a majority of shape-changing moves [107] accepted at high temperatures and a smaller percentage of exchange moves, which are accepted at a lower temperature, see section 2.1.2 for a description of the moves. Acceptance temperature values will be given when treating the specific case studies in the next section. As shown in Ref. [108], this is the most efficient scheme for a standard BH algorithm in the optimization of nanoalloys. On the other hand, the lw evolves by a majority of exchange moves and a smaller percentage of shape-changing moves, with all moves accepted at low temperatures. We note that the most efficient settings for BH searches in nanoalloys, as determined in Ref. [108], imply acceptance rates in the range 20-40% for moves aiming at the wide exploration of the landscape, while the best refinement of chemical ordering (i.e. for exploitation purposes [126]) is obtained with much lower acceptance rates, below 5%.

The basic idea of the FL algorithm is that the lw periodically takes configurations from the fw (i.e. it is restarted) and refines them to decrease their energy, while the fw continues its broad range exploration of the landscape at high temperatures. In fact, we remember that accepting moves at high temperatures generally means that structures having high energies in the potential energy surface are visited by the walker. To follow this scheme, a prescription to periodically restart the lw is necessary. Here we describe the one that we adopted for the FL algorithm.

Let us consider a simulation of N BH steps, numbered by $n = 0, 1, ..., N-1$. With $C_{fw}(t_n)$ and $C_{lw}(t_n)$ we indicate the configurations (i.e. the sets of atomic coordinates $\{\mathbf{R}\}$) of the fw and lw, respectively, whereas $E_{fw}(t_n)$ and $E_{lw}(t_n)$ are their locally minimized energies. Let t_{n_0} be the time of the last restart of the lw. At t_{n_0} both the fw and the lw have the same energy $E(t_{n_0})$ and then they evolve independently. The two walkers are updated sequentially one by one, by some kind of move, according to percentages and acceptance temperatures as explained above. Now, let us assume that at $t_{\tilde{n}} > t_{n_0}$ the fw has improved its own best energy. When this happens, the lw may be restarted. One possibility could be to restart the lw each time the fw improves its own best energy. More generally, the fw may be restarted by from time to time, following a probabilistic criterion. By definition, we have that

$$E(t_{n_0}) - E_{fw}(t_{\tilde{n}}) > 0, \tag{4.1}$$

and, since we expect that the landing walker is decreasing faster in energy than the flying walker, we have also

$$E(t_{n_0}) - E_{lw}(t_{\tilde{n}}) > E(t_{n_0}) - E_{fw}(t_{\tilde{n}}) > 0, \tag{4.2}$$

so that the quantity

$$\xi = \frac{E(t_{n_0}) - E_{fw}(t_{\tilde{n}})}{E(t_{n_0}) - E_{lw}(t_{\tilde{n}})} \tag{4.3}$$

satisfies $0 \leq \xi \leq 1$ in most cases. We choose to restart the lw with probability p_r

$$p_r = \xi^{\alpha}, \tag{4.4}$$

where $\alpha \geq 0$, by extracting a random number r_{fl} uniformly distributed between 0 and 1. If $r_{fl} \leq p_r$ the lw is restarted, and takes the configuration of the fw at $t_{\tilde{n}}$, i.e. $C_{lw}(t_{\tilde{n}+1}) \leftarrow C_{fw}(t_{\tilde{n}})$. If the condition of Eq. (4.2) is not fulfilled, the lw has not improved the energy better than the fw did, so that it is restarted automatically with probability 1.

For $\alpha = 0$ the lw is restarted every time the fw finds a new lowest energy, since $p_r = 1$ always. Other reasonable choices of α are $\alpha = 1/2$ or $\alpha = 1$. The number of restarts decreases at increasing α.

In Fig. 4.1 a block diagram for the FL algorithm is given. A representative behavior of the time evolution of the fw and lw walkers is shown instead in Fig. 4.2, where $\alpha = 1$ is used, for an example of optimization of an $Au_{200}Cu_{200}$ nanoalloy (the optimization of this system will be treated more in detail in a following section). The fw evolves at high temperatures, finding local minima whose energies correspond to the orange line. Every time the fw improves its best local minimum (see the red squares), the algorithm decides whether to restart the lw according to the criterion of Eqs. (4.3) and (4.4). When the lw restarts, its energy suddenly increases (see the light blue line in Fig. 4.2) and then quickly drops down thanks to the exchange and shape-changing moves accepted at low temperatures. Each time the lw finds a better local minimum, the structure is stored together with its energy (these events correspond to the purple circles).

A further refinement of the FL algorithm is obtained by adding a third walker, denoted as the *hiking walker* (hw), whose configurations and energies will be denoted by $C_{hw}(t_n)$ and $E_{hw}(t_n)$. In the following, this algorithm is referred to as FLH algorithm. The hw is used basically for continuing the refinement of the configurations at low temperatures, even when the lw jumps up in energy to restart its search. In order to do that, the hw uses the same type of moves and acceptance temperatures as the lw. Let us assume that at time $t_{\hat{n}}$ the lw reaches energy which is lower than the lowest energy reached by the hw walker so far, i.e

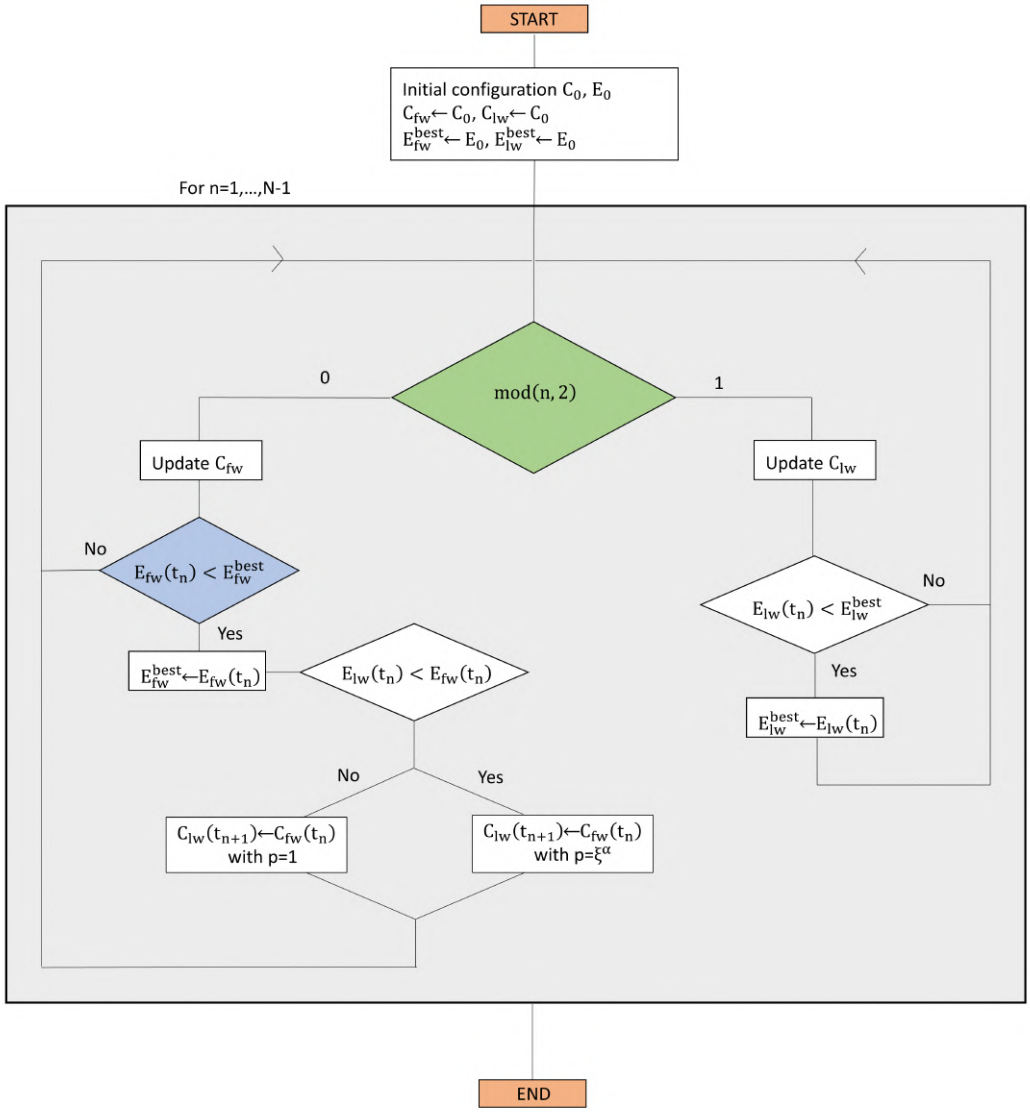

Fig. 4.1 Block diagram of the FL algorithm. In a simulation of N steps numbered as $n = 0, 1..., N-1$, the configurations of fw (C_{fw}) and of lw (C_{lw}) are updated for $\mathrm{mod}(n,2) = 0$ and $\mathrm{mod}(n,2) = 1$, respectively. Reproduced from [125]. © 2023 The Authors. Advanced Theory and Simulations published by Wiley-VCH GmbH.

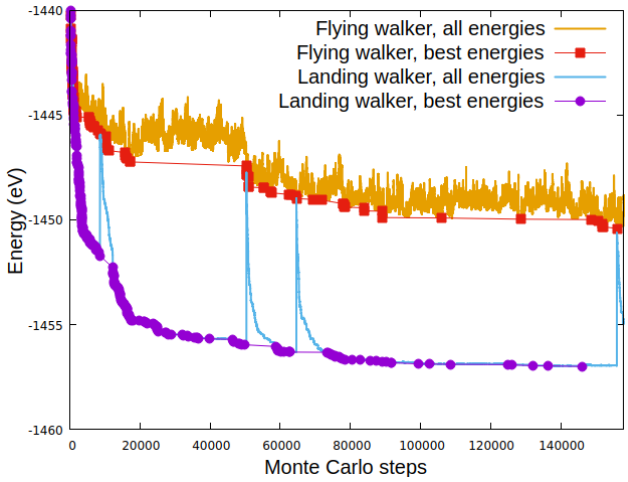

Fig. 4.2 Evolution of the energy during optimization of an $Au_{300}Cu_{100}$ nanoalloy. In this simulation, one fw is used together with its associated lw, which is restarted according to the probability of Eqs. (4.3) and (4.4) with $\alpha = 1$. When the lw is restarted its energy suddenly increases to match the energy of the fw. Then the energy sharply decreases due to the exchange and surface rearrangement moves accepted at low temperatures. Reproduced from [125]. © 2023 The Authors. Advanced Theory and Simulations published by Wiley-VCH GmbH.

$E_{lw}(t_{\hat{n}}) < E_{hw}^{best}$. If this condition holds, the hw is restarted by taking the configuration of the lw and its energy, so that $E_{hw}(t_{\hat{n}+1}) = E_{lw}(t_{\hat{n}})$. At the same time, the lw is restarted too, i.e. it takes configuration and energy from the fw, so that $E_{lw}(t_{\hat{n}+1}) = E_{fw}(t_{\hat{n}})$. In this way the lw goes up and down in energy between the fw and the hw, with the aim of feeding the hw with new good configurations to be further refined. Also in this case the three walkers are updated sequentially one by one, according to percentages and acceptance temperatures for different moves as explained above.

The block diagram of the FLH algorithm is given in Fig. 4.3, whereas a representative behavior of the time evolution of the three walkers is shown in Fig. 4.4. We note that in the FLH scheme, the fw evolves in the same way as in the FL algorithm, but the lw is restarted in two cases – i. according to the criterion of Eqs. (4.3) and (4.4), as in the FL algorithm; ii. every time it finds a new putative global minimum (i.e., when its energy is lower than the best energy found by the hw so far). In case ii., the hw takes configuration and energy from the lw with probability 1.

These algorithm can be used also with multiple flying walkers running in parallel, each with its individual landing and hiking walker. In this scheme, referred to as FLH-PEW algorithm, the flying walker may interact with each other in the space of a suitable order

parameter, as in the PEW algorithm [55, 107], while the landing walkers do not interact with each other.

4.2 Results and Discussion

In this section we present some case studies to test and compare the efficiency of the three different algorithms: standard BH, FL and FLH. In all cases, we considered binary metallic systems whose interactions are described by the Gupta potential. The parameters of the potentials are given in Appendix B.

The AuCu, AuRh, and PtNi systems were chosen because they have been the subject of previous optimization studies so a comparison can be made. The AgCu system was chosen to deal with the optimization of large nanoalloys, containing up to a few thousand atoms, also comparing the outcomes of unseeded and seeded optimizations. AgCu is a widely studied system from the experimental point of view [113, 138–143], and, as such, it has been the subject of many optimization studies [24, 110–112, 144–146], but systematic unseeded searches for sizes of few hundred atoms and above were still missing.

4.2.1 $Au_{300}Cu_{100}$, $Au_{200}Cu_{200}$ and $Au_{300}Rh_{100}$

The $Au_{300}Cu_{100}$, $Au_{200}Cu_{200}$ and $Au_{300}Rh_{100}$ systems were studied in Rossi et al. [108] by the BH algorithm in which different shape-changing moves and exchange moves were accepted at different temperatures. Here we report the comparison between the BH optimization algorithm as used in Ref. [108] and the FL and FLH algorithms.

In agreement with Ref. [108], we found that for all systems the global minimum is a Mackay icosahedron (Ih) with an incomplete outer shell as shown in Fig. 4.5, where the best structures belonging to the other relevant motifs are shown too. These motifs are the Marks decahedron (Dh) [147], the face-centered-cubic truncated octahedron (fcc) and the icosahedron with incomplete anti-Mackay shell (Ih-aM) [24].

Here below we analyze the performance of the BH, FL, and FLH algorithms separately for each system.

$Au_{300}Cu_{100}$

For $Au_{300}Cu_{100}$ we performed searches of $N = 300000$ steps for each algorithm. Note that this implies that in the FL algorithm both the fw and the lw make 150000 steps, whereas in the FLH algorithm, each walker makes 100000 steps. In all simulations, the same types of moves were used, namely the *Brownian* and the *bonds* moves, which mainly affect the

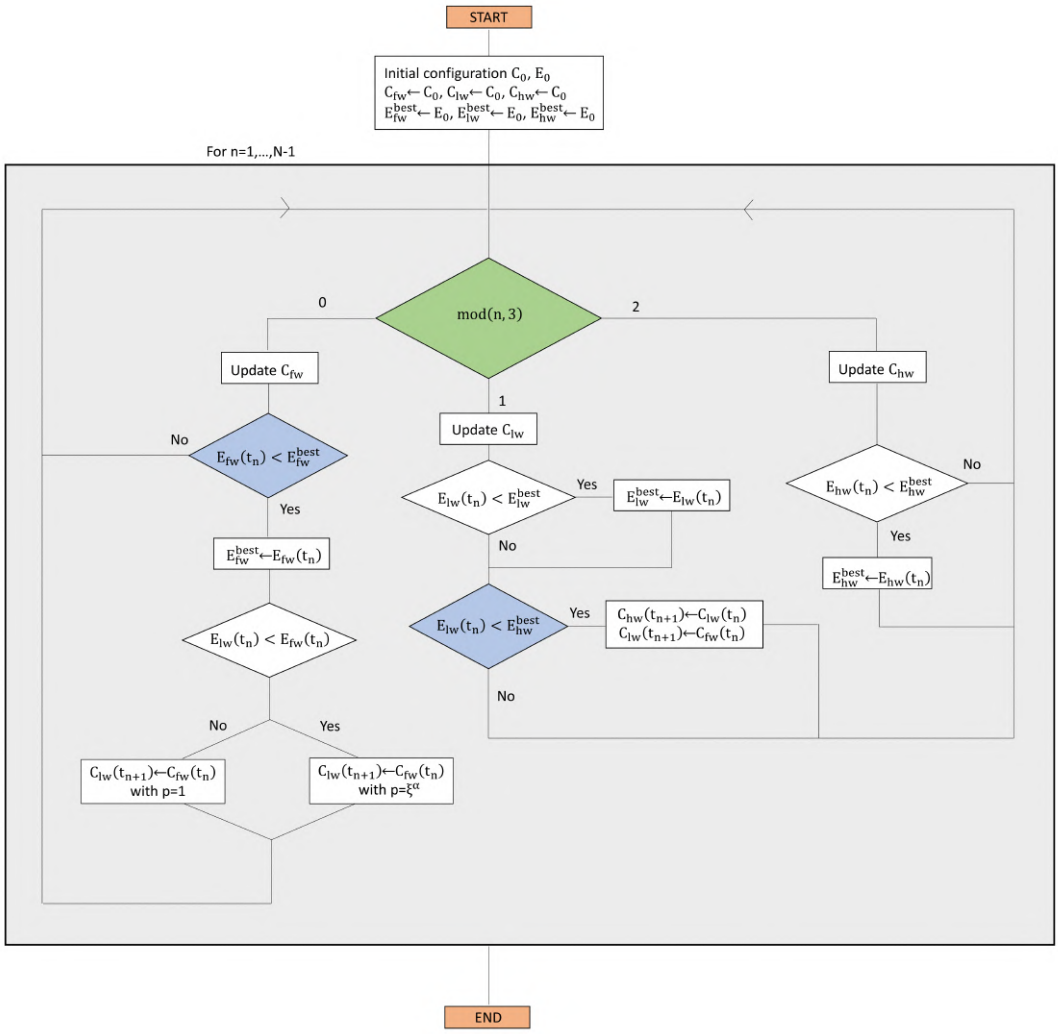

Fig. 4.3 Block diagram of the FLH algorithm. In a simulation of N steps numbered as $n = 0, 1..., N-1$, the configurations of fw (C_{fw}), lw (C_{lw}) and hw (C_{hw})are updated for $\mathrm{mod}(n,3) = 0$, $\mathrm{mod}(n,3) = 1$ and $\mathrm{mod}(n,3) = 2$, respectively. Reproduced from [125]. © 2023 The Authors. Advanced Theory and Simulations published by Wiley-VCH GmbH.

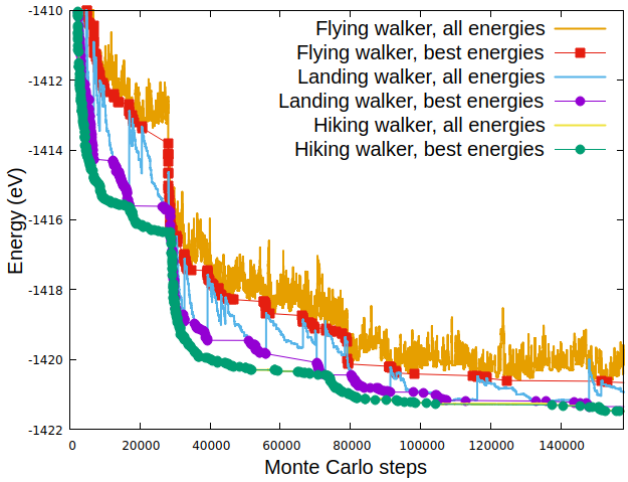

Fig. 4.4 Evolution of the energy during optimization of an $Au_{200}Cu_{200}$ nanoalloy. In this simulation, one fw is used together with its associated lw and hw, which are restarted according to the rules explained in the text. Reproduced from [125]. © 2023 The Authors. Advanced Theory and Simulations published by Wiley-VCH GmbH.

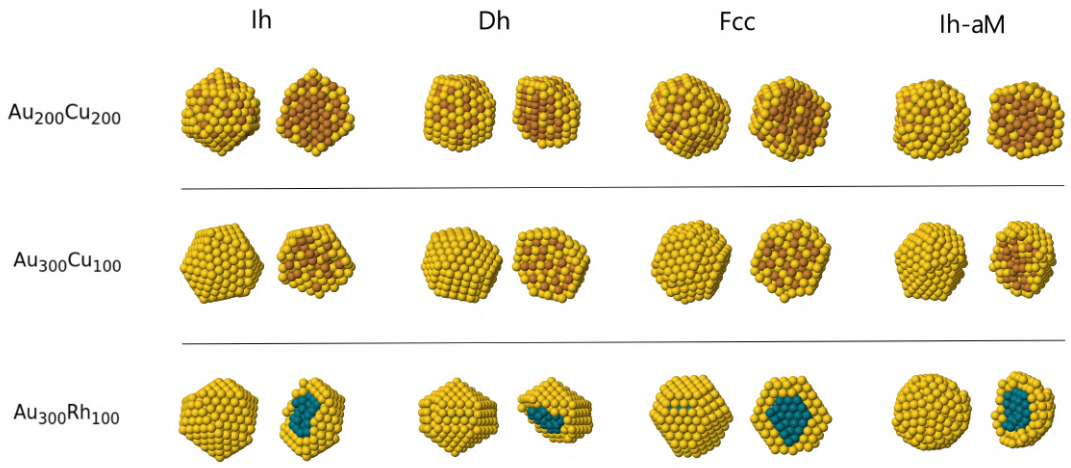

Fig. 4.5 Lowest-energy structures belonging to the different structural motifs: Mackay icosahedra (Ih), Marks decahedra (Dh), face centered cubic truncated octahedra (fcc) and anti-Mackay icosahedra (Ih-aM). Every structure is shown in two views, showing the surface and a cross-section. For all systems, the lowest energy structures are the Mackay icosahedra (Ih). Reproduced from [125]. © 2023 The Authors. Advanced Theory and Simulations published by Wiley-VCH GmbH.

system	algorithm	setting	walker	f_{Br}	T_{Br}^{acc}	f_{exch}	T_{exch}^{acc}	f_{bonds}	T_{bonds}^{acc}
$Au_{300}Cu_{100}$	BH	1	fw	0.600	3000	0.200	100	0.200	100
		2	fw	0.600	3000	0.300	100	0.100	100
	FL	1	fw	0.800	3000	0.100	100	0.100	100
			lw	0.100	100	0.800	100	0.100	100
		2	fw	0.600	3500	0.200	100	0.200	100
			lw	0.100	100	0.800	100	0.100	100
	FLH	1	fw	0.600	3500	0.200	300	0.200	300
			lw, hw	0.100	100	0.800	100	0.100	100
		2	fw	0.800	3500	0.100	100	0.100	100
			lw, hw	0.100	100	0.800	100	0.100	100

Table 4.1 Settings of the simulations for $Au_{300}Cu_{100}$. One hundred simulations per setting were made. T_{Br}^{acc}, T_{exch}^{acc} and T_{bonds}^{acc} are the acceptance temperatures (in K) of Brownian, random exchange and bonds moves. f_{Br}^{acc}, f_{exch}^{acc} and f_{bonds}^{acc} are the fractions of Brownian, random exchange and bonds moves. Reproduced from [125]. © 2023 The Authors. Advanced Theory and Simulations published by Wiley-VCH GmbH.

cluster shape, and the *random exchange* move, which mainly affects chemical ordering [107]. The *Brownian* move consists of a molecular dynamics run of 200 steps at a temperature of 2000 K.

For each algorithm, two settings of the moves were used, and, for each setting, 100 independent searches were run to accumulate 200 simulations per algorithm. The settings of the simulations are reported in Table 4.1.

All algorithms found lowest-energy structures with exactly the same geometric shape but slightly differing in chemical ordering, with the best and second best chemical ordering found by the FLH and FL algorithms, respectively, as can be seen in Table 4.2.

In Table 4.2 we display the energy difference between the global minimum found for any of the three system and the best structure found for the other relevant structural motifs, for all three algorithms. For example, ΔE_{Dh}^{best} in the first row is the energy difference between the best decahedron found by the standard BH algorithm and the global minimum, which is a Mackay icosahedron found by the FLH algorithm. The main difference between the performances of the three algorithms is clearly shown in Fig. 4.6, where the frequencies at which the searches were able to converge close to the lowest-energy structure are plotted in a histogram.

In 300000 steps, FLH was able to get within 0.25 eV from the lowest-energy structure 27 times, compared to the 24 and 18 times of FL and BH. The better performance of FLH is even more evident if the results are compared at the same CPU times instead of the same number of steps (right plot of Fig. 4.6). In fact, in the CPU time in which FLH completes 300000

system	algorithm	ΔE_{Ih}^{best}	ΔE_{Dh}^{best}	ΔE_{fcc}^{best}	ΔE_{Ih-aM}^{best}
$Au_{300}Cu_{100}$	BH	0.106	2.078	2.927	1.380
	FL	0.007	*1.715*	*2.923*	*1.307*
	FLH	**0.000**	2.060	3.023	2.466
$Au_{200}Cu_{200}$	BH	0.212	3.423	3.815	0.988
	FL	0.141	*2.623*	*3.366*	1.337
	FLH	**0.000**	3.096	3.453	*0.616*
$Au_{300}Rh_{100}$	BH	**0.000**	5.898	*5.321*	2.037
	FL	**0.000**	*4.629*	5.385	*2.032*
	FLH	**0.000**	5.882	5.376	5.535

Table 4.2 Energy differences between global minimum and best isomer for the four main different geometrical motifs (Mackay Icosahedron, Decahedron, Face Centered Cubic, and Anti-Mackay Icosahedron), as found by the three different algorithms for the three different systems. All energy differences are in eV. Reproduced from [125]. © 2023 The Authors. Advanced Theory and Simulations published by Wiley-VCH GmbH.

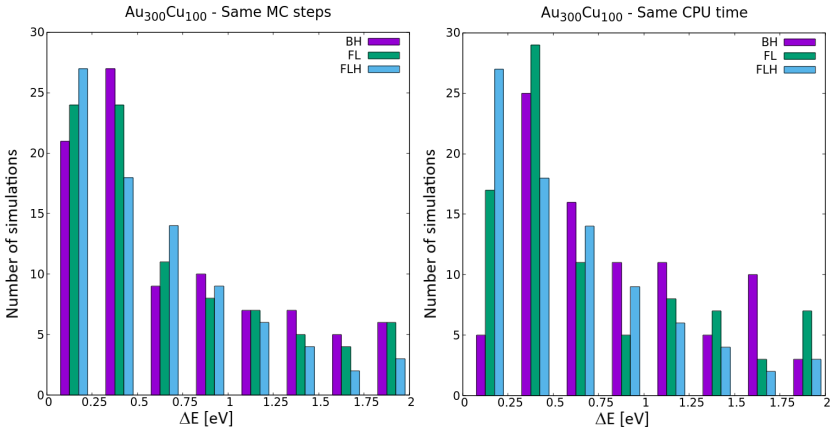

Fig. 4.6 Histogram of the energies (in eV) of the lowest-energy structures found in the global optimization searches for a $Au_{300}Cu_{100}$ nanoalloy. For each algorithm, 200 independent searches of 300000 steps each were made. Reproduced from [125]. © 2023 The Authors. Advanced Theory and Simulations published by Wiley-VCH GmbH.

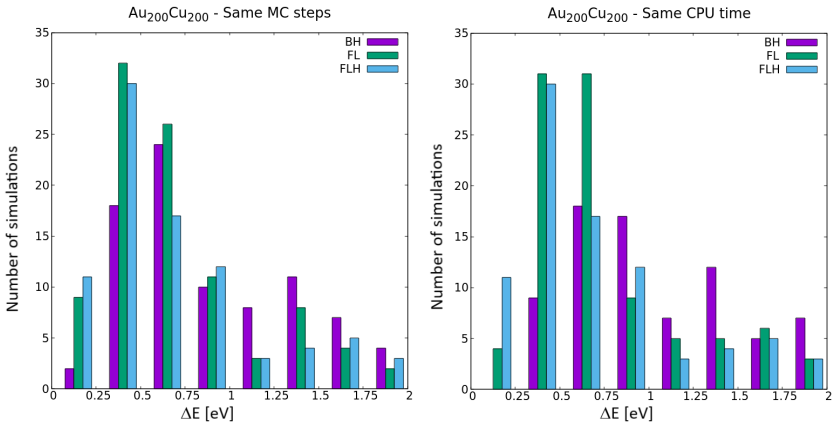

Fig. 4.7 Histogram of the energies (in eV) of the lowest-energy structures found in the global optimization searches for a $Au_{200}Cu_{200}$ nanoalloy. For each algorithm, 200 independent searches of 300000 steps each were made. Reproduced from [125]. © 2023 The Authors. Advanced Theory and Simulations published by Wiley-VCH GmbH.

steps, FL and BH complete 240000 and 170000 steps on average. Steps in FLH are on average faster because of the larger proportion of exchange moves whose local minimization is much faster than that of shape-changing moves. At the same CPU time, the number of searches that ended within 0.25 eV were 27, 17, and 5 for FHL, FL, and BH. On the other hand, if we compare the efficiency to explore other structural motifs beyond the dominant one, FL obtains better results than FLH and BH (see Table 4.2).

$\mathbf{Au_{200}Cu_{200}}$

For $Au_{200}Cu_{200}$ we adopted the same scheme as for $Au_{300}Cu_{100}$. The lowest-energy Mackay icosahedral shape was found by all algorithms, but FLH was able to perform a better optimization of chemical ordering than FL and BH, thus obtaining the lowest-energy structure (see Table 4.2). The histograms of Fig. 4.7 show that, in 300000 steps per simulation, FLH was able to optimize within 0.25 eV from the best structure in 11 simulations over 200, compared to the 9 of FL and to the 2 of BH. These numbers become 11, 4, and 0 when the comparison is made at the same CPU time.

In Table 4.3 all simulation settings are reported. As regards the other structural motifs FL performed slightly better than FLH, whereas BH was less efficient than both.

$\mathbf{Au_{300}Rh_{100}}$

For $Au_{300}Rh_{100}$ we performed 100 searches of 300000 steps for each algorithm. Also in these simulations, the same types of moves were used, namely the *Brownian* and the *bonds*

system	algorithm	setting	walker	f_{Br}	T_{Br}^{acc}	f_{exch}	T_{exch}^{acc}	f_{bonds}	T_{bonds}^{acc}
$Au_{200}Cu_{200}$	BH	1	fw	0.800	3000	0.100	100	0.100	100
		2	fw	0.666	3000	0.167	100	0.167	100
	FL	1	fw	0.800	4000	0.100	100	0.100	100
			lw	0.167	100	0.666	100	0.167	100
		2	fw	0.800	4000	0.100	100	0.100	100
			lw	0.100	100	0.800	100	0.100	100
	FLH	1	fw	0.800	4000	0.100	100	0.100	100
			lw, hw	0.167	100	0.666	100	0.167	100
		2	fw	0.800	4500	0.100	100	0.100	100
			lw, hw	0.100	100	0.800	100	0.100	100

Table 4.3 Settings of the simulations for $Au_{200}Cu_{200}$. One hundred simulations per setting were made. T_{Br}^{acc}, T_{exch}^{acc} and T_{bonds}^{acc} are the acceptance temperatures (in K) of Brownian, random exchange and bonds moves. f_{Br}^{acc}, f_{exch}^{acc} and f_{bonds}^{acc} are the fractions of Brownian, random exchange and bonds moves. Reproduced from [125]. © 2023 The Authors. Advanced Theory and Simulations published by Wiley-VCH GmbH.

moves, which mainly affect the cluster shape, and the *tailored exchange* move, which mainly affects chemical ordering and favors the convergence towards phase-separated configurations [148]. The *Brownian* consisted of a molecular dynamics run of 200 steps at a temperature of 3000 K. The settings of the searches are reported in Table 4.4.

For these systems, whose most favorable chemical ordering is core@shell Rh@Au [108], all algorithms were able to find the lowest-energy structure. However, FLH was able to find low-energy structures more frequently than FL and BH, as shown in Fig. 4.8. In fact, when comparing the algorithms for the same number of steps, FLH searches found isomers within 0.25 eV from the global minimum in 28 simulations over 100, against 17 and 9 of FH and BH. The superior performance of FLH was even more evident in the comparison for the same CPU time (28 against 14 and 7 searches within 0.25 eV). On the other hand, FL was more efficient in exploring other motifs than the Mackay Ih (see again Table 4.2).

4.2.2 $Pt_{19}Ni_{19}$ and $Pt_{27}Ni_{28}$

For PtNi, the parameters of the Gupta potential were taken from Yang et al. [44], who optimized all compositions for sizes 38 and 55 with a new improved algorithm. Here, we concentrated on $Pt_{19}Ni_{19}$ and $Pt_{27}Ni_{28}$, for which complete data on the CPU times are available [44]. For both $Pt_{19}Ni_{19}$ and $Pt_{27}Ni_{28}$ we ran 100 independent searches by the FLH algorithm. The settings of the moves for these searches are given in Table 4.5.

system	algorithm	setting	walker	f_{Br}	T_{Br}^{acc}	f_{exch}	T_{exch}^{acc}	f_{bonds}	T_{bonds}^{acc}
$Au_{300}Rh_{100}$	BH	1	fw	0.800	2000	0.200	700	0.000	–
		2	fw	0.800	2000	0.100	700	0.100	300
		3	fw	0.800	2500	0.200	700	0.000	–
		4	fw	0.800	1500	0.200	700	0.000	–
		5	fw	0.800	2500	0.100	700	0.100	300
		6	fw	0.800	3000	0.100	700	0.100	300
		7	fw	0.700	2500	0.200	700	0.100	300
		8	fw	0.700	3000	0.200	700	0.100	300
		9	fw	0.700	3500	0.200	700	0.100	300
		10	fw	0.800	2250	0.100	170	0.100	300
	FL (FLH)	1	fw	0.800	3500	0.100	700	0.100	300
			lw (hw)	0.167	300	0.666	700	0.167	300
		2	fw	0.800	3500	0.100	700	0.100	300
			lw (hw)	0.167	300	0.666	700	0.167	300
		3	fw	0.800	3500	0.100	700	0.100	300
			lw (hw)	0.167	300	0.666	700	0.167	300
		4	fw	0.800	3500	0.100	1000	0.100	2000
			lw (hw)	0.167	300	0.666	700	0.167	300
		5	fw	0.800	3500	0.100	2500	0.100	300
			lw (hw)	0.100	300	0.800	700	0.100	300
		6	fw	0.800	3500	0.100	3000	0.100	2500
			lw (hw)	0.167	300	0.666	700	0.167	300
		7	fw	0.800	3500	0.100	2000	0.100	3000
			lw (hw)	0.167	300	0.666	700	0.167	300
		8	fw	0.800	3500	0.100	100	0.100	2000
			lw (hw)	0.167	300	0.666	700	0.167	300
		9	fw	0.800	3500	0.100	1000	0.100	2500
			lw (hw)	0.167	300	0.666	700	0.167	300
		10	fw	0.800	3500	0.100	1000	0.100	3000
			lw (hw)	0.167	300	0.666	700	0.167	300

Table 4.4 Settings of the simulations for $Au_{300}Rh_{100}$ for BH, FL and FLH algorithms. For FLH, the same settings as for FL were used, simply repeating the setting of the lw also for the hw. Ten simulations per setting were made. T_{Br}^{acc}, T_{exch}^{acc} and T_{bonds}^{acc} are the acceptance temperatures (in K) of Brownian, tailored exchange and bonds moves. f_{Br}^{acc}, f_{exch}^{acc} and f_{bonds}^{acc} are the fractions of Brownian, random exchange and bonds moves. Reproduced from [125].

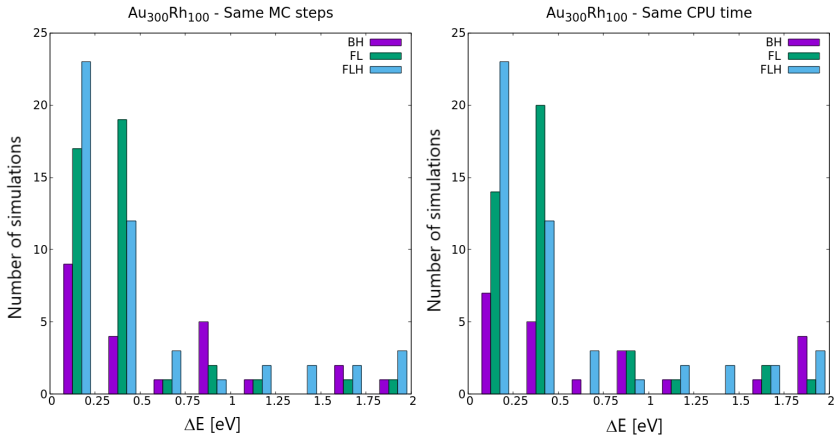

Fig. 4.8 Histogram of the energies (in eV) of the lowest-energy structures found in the global optimization searches for a $Au_{300}Rh_{100}$ nanoalloy. For each algorithm, 100 independent searches of 300000 steps each were made. Reproduced from [125]. © 2023 The Authors. Advanced Theory and Simulations published by Wiley-VCH GmbH.

system	algorithm	setting	walker	f_{shake}	T^{acc}_{shake}	f_{exch}	T^{acc}_{exch}	f_{bonds}	T^{acc}_{bonds}
PtNi, all cases	FLH	1	fw	0.800	3000	0.100	100	0.100	100
			lw, hw	0.100	100	0.800	100	0.100	100

Table 4.5 Setting of the simulations for PtNi. One hundred simulations per setting were made. T^{acc}_{shake}, T^{acc}_{exch} and T^{acc}_{bonds} are the acceptance temperatures (in K) of shake, random exchange and bonds moves. f^{acc}_{shake}, f^{acc}_{exch} and f^{acc}_{bonds} are the fractions of shake, random exchange and bonds moves. Reproduced from [125]. © 2023 The Authors. Advanced Theory and Simulations published by Wiley-VCH GmbH.

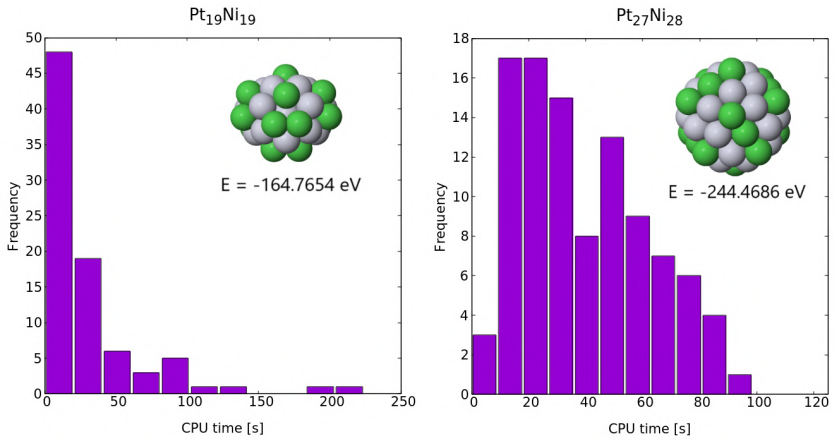

Fig. 4.9 Histogram of the CPU times (in seconds) for finding the global minimum of $Pt_{19}Ni_{19}$ and $Pt_{27}Ni_{28}$ nanoalloys. Reproduced from [125]. © 2023 The Authors. Advanced Theory and Simulations published by Wiley-VCH GmbH.

We note that at variance of the previous cases, *shake* moves instead of *Brownian* moves were used for shape changes. This is because, for small systems, global optimizations usually take more advantage from *shake* moves than from *Brownian* moves. In the *shake* moves every atom was displaced randomly around its present position with a sphere with radius of 1.3 Å.

Each run was of 100000 steps, and took on average 234 s for $Pt_{19}Ni_{19}$ and 312 s for $Pt_{27}Ni_{28}$, running on a single core of a workstation equipped with a quad-core Intel(R) Core(TM) i7-6700K CPU with 16 GB of RAM. The FLH algorithm was able to locate the same global minima as in Ref. [44], with a success rate of 85/100 for $Pt_{19}Ni_{19}$, which is a very high rate compared to the 12/40 of Ref. [44]. For $Pt_{27}Ni_{28}$ the success rate was 100/100. The average CPU times of successful searches were very short: 31 s for $Pt_{19}Ni_{19}$ and 39 s for $Pt_{27}Ni_{28}$, corresponding to 13300 and 12500 steps on average, respectively. These times are considerably shorter than those in the previous literature. The complete data about the time distribution of successful searches are given in Fig. 4.9. Finally, we note that the relatively easier optimization of $Pt_{27}Ni_{28}$ compared to $Pt_{19}Ni_{19}$ is due to the single-funnel character of the potential energy surface of the former and the double-funnel character of the potential energy surface of the latter [35], where the global minimum is in competition with a regular truncated octahedral structure whose energy is higher by 0.10 eV.

4.2.3 Optimization of larger nanoparticles

In this section, we describe the results of optimizing larger bi-metallic nanoparticles. We chose the AgCu system because it has been the subject of several optimization studies from

very small sizes to a few hundred atoms, in which both shape and chemical ordering were fully optimized starting from random configurations [24, 93, 109–112, 149–152]. Optimization of chemical ordering alone at fixed shape has been performed for AgCu nanoparticles of a few thousand atoms [145, 146]. Here we extended the size of full global optimization well above 10^3 atoms, with the aim of shedding light on the following issues:

i) In the size range up to a few hundred atoms, the best structures of AgCu nanoparticles can be significantly different from those of the pure clusters Ag and Cu of the same size [24, 93, 111, 112]. Is this fact still true for larger nanoparticles of a few thousand atoms? If yes, this would mean that the bulk-like behavior is attained at a much larger size in nanoalloys than in the corresponding pure systems.

ii) The mixing energy in AgCu nanoalloys of a few hundred atoms is negative for almost all compositions (see the cases of 100 and 200 atoms in Ref. [93]). This is a completely different behaviour from the bulk AgCu, where mixing energy is always positive [153]. What is the sign of the mixing energy for nanoparticles of several thousand atoms?

iii) Is the optimization of chemical ordering alone at fixed shape able to produce low energy structures resembling those of full global optimization?

In order to treat these issues, we optimized AgCu nanoparticles of sizes $N = 586, 1289, 2406$ and 4033 atoms, corresponding to the magic sizes of regular truncated octahedra [14]. For $N = 586, 1289, 2406$ we fully optimized the nanoparticles starting from random configurations and consider compositions with $N_{Ag} = 0.1N, 0.2N, ..., 0.9N$, whereas for $N = 4033$ we only performed seeded optimizations, considering two compositions only: $N_{Ag} = 2823$ and $N_{Ag} = 3000$. Representative lowest-energy structures for the different sizes and compositions are shown in Figs. 4.10, 4.11, and 4.12.

For $N = 586$, the substitution of 10% Ag in Cu or of 10% Cu in Ag is already sufficient to cause a transition from the fcc truncated octahedron to the icosahedron, whose magic number is at $N = 561$, so that the 25 additional atoms are placed in an island with anti-Mackay stacking [24]. Truncated octahedral structures however reappear for intermediate compositions [109], but they are different from the regular truncated octahedron of the pure Ag and Cu clusters. An example of these truncated octahedral structures is given in Fig. 4.10 for composition $Ag_{234}Cu_{352}$. This structure is core@shell Cu@Ag. It presents an Ag surface and only one Ag internal atom. In addition, there is an Ag adatom on top of its surface. Therefore this structure is magic, with a monolayer Ag shell, for $N = 585$ and composition $Ag_{232}Cu_{353}$. It is asymmetric, with two 3×3, two 4×3, one 5×4, and one 4×4 square

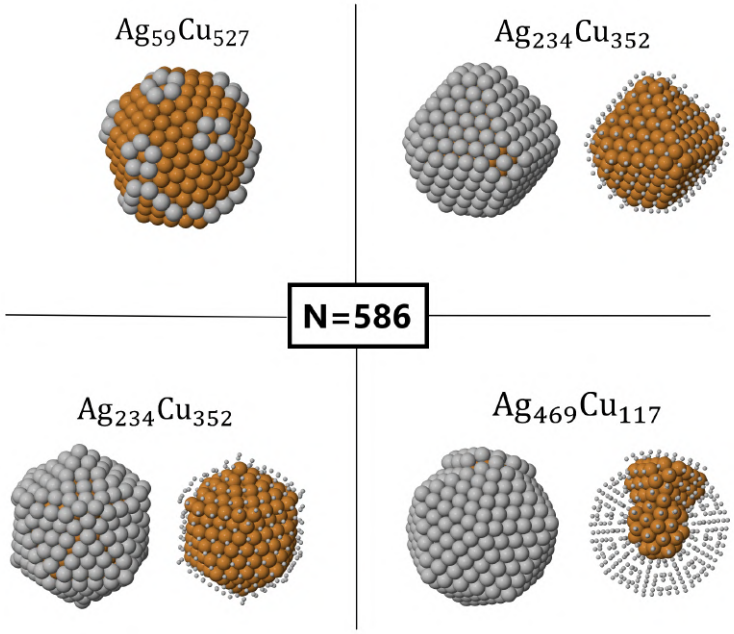

Fig. 4.10 AgCu structures for $N = 586$ at different compositions. Reproduced from [125]. © 2023 The Authors. Advanced Theory and Simulations published by Wiley-VCH GmbH.

facets. For comparison, the regular truncated octahedron for $N = 586$ has six symmetric 4×4 facets.

For $N = 1289$ and 2406 (see Fig. 4.11), icosahedral structures are still dominant for a wide spectrum of compositions, especially in the intermediate range. Truncated octahedral or decahedral structures were found for Ag-rich and Cu-rich compositions.

Finally, since for $N = 4033$ calculations are very cumbersome, we considered only two compositions, $Ag_{2823}Cu_{1210}$ and $Ag_{3000}Cu_{1033}$, and in both cases, we ran seeded optimizations. As seeds, we used regular truncated octahedra or incomplete icosahedra with random chemical ordering. The optimization runs allowed for both shape-changing and exchange moves. Also for this size (results in Fig. 4.12), icosahedral nanoparticles were found lower in energy than truncated octahedral ones.

In relation to point i), our result indeed shows that icosahedral structures are still dominant for intermediate compositions in a size range where for elemental nanoparticles truncated octahedra are much lower in energy [100]. This effect is due to the atomic stress release effect allowed by size mismatch between Cu and Ag atoms [154], since Cu atoms are about 13% smaller. The transition from truncated octahedra to icosahedra experimentally observed in AuPd clusters has been attributed to stress release allowed by size mismatch [19]. These

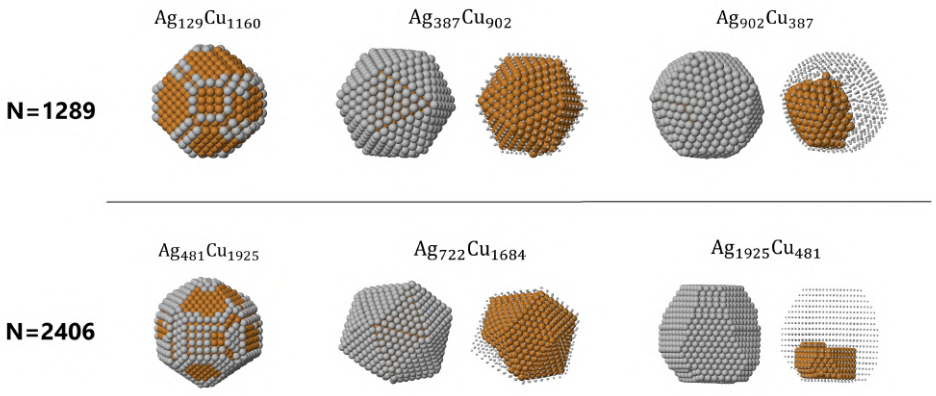

Fig. 4.11 AgCu structures for $N = 1289$ and $N = 2406$ at different compositions. Reproduced from [125]. © 2023 The Authors. Advanced Theory and Simulations published by Wiley-VCH GmbH.

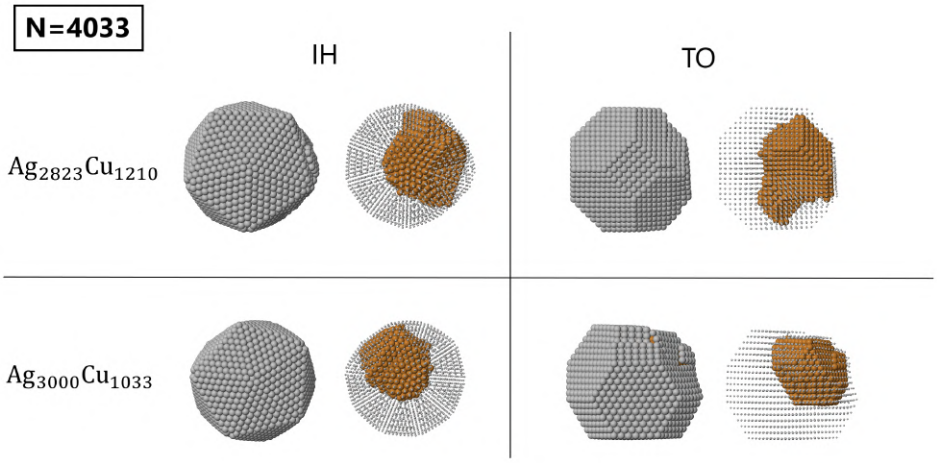

Fig. 4.12 AgCu structures for $N = 4033$ at different compositions. Reproduced from [125]. © 2023 The Authors. Advanced Theory and Simulations published by Wiley-VCH GmbH.

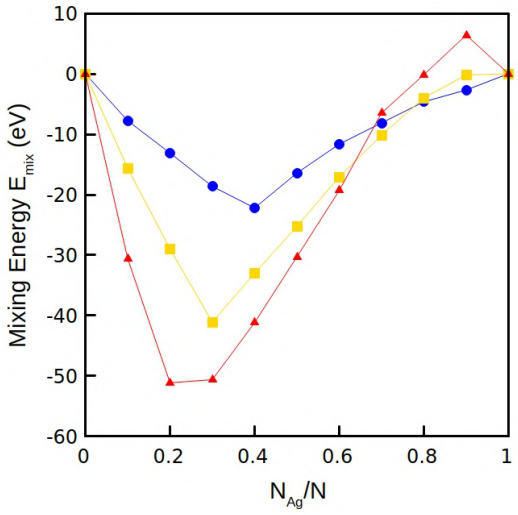

Fig. 4.13 Mixing energy E_{mix} depending on composition N_{Ag}/N for different sizes $N = 586$ (blue circles), 1289 (yellow squares), 2406 (red triangles). Reproduced from [125]. © 2023 The Authors. Advanced Theory and Simulations published by Wiley-VCH GmbH.

results demonstrate that the bulk-like behavior in nanoalloys shall be attained at much larger sizes than in elemental nanoparticles.

Regarding point ii), we calculated the mixing energies as a function of composition for $N = 586, 1289$, and 2406 nanoalloys. We remember that the mixing energy E_{mix} of a generic AgCu nanoalloy having N_{Ag} silver atoms and N_{Cu} copper atoms, is defined as

$$E_{mix}(N_{Ag},N_{Cu}) = E(N_{Ag},N_{Cu}) - \frac{E(N,0)}{N}N_{Ag} - \frac{E(0,N)}{N}N_{Cu}, \tag{4.5}$$

where $N = N_{Ag} + N_{Cu}$ is the total number of atoms of the nanoalloys and $E(N_{Ag},N_{Cu})$ its potential energy. $E(N,0)$ and $E(0,N)$ are the potential energies of the reference structures of pure clusters, in our cases fcc regular truncated octahedra [13, 14]. The results of our calculations are shown in Fig. 4.13. In all cases, E_{mix} shows a rather regular behavior as a function of N_{Ag}/N. For $N = 586$ and 1289, E_{mix} is always negative at least in the range of $0.1 \leq N_{Ag}/N \leq 0.9$. For $N = 2406$, there is an Ag-rich range, roughly above $N_{Ag}/N > 0.8$ in which E_{mix} is positive. For $N = 4033$, the mixing energies of the two lowest-energy icosahedral nanoparticles, whose compositions are in the range $0.70 \leq N_{Ag}/N \leq 0.75$, are slightly negative. From the results of Fig. 4.13, we note also that E_{mix} has a rather sharp minimum whose position shifts to smaller and smaller N_{Ag}/N as size increases.

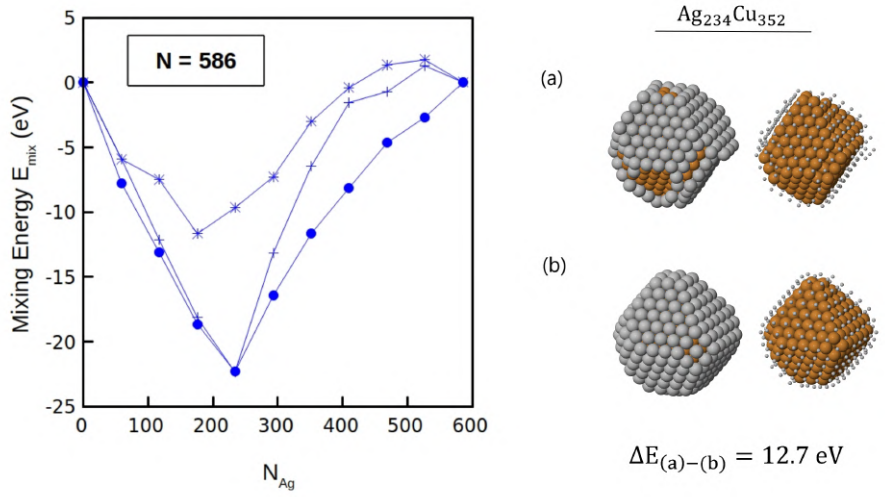

Fig. 4.14 Left panel: mixing energy plot for $N = 586$ AgCu nanoparticles at different compositions as found by different optimization schemes. Circles correspond to full unseeded optimization, crosses to seeded optimization with exchange and Brownian moves, stars to seeded optimization with exchanges only. Right panel: the two structures found at composition $Ag_{234}Cu_{352}$ by (a) seeded optimization with exchange moves only, and (b) seeded optimization with both exchange and Brownian moves. Reproduced from [125]. © 2023 The Authors. Advanced Theory and Simulations published by Wiley-VCH GmbH.

The change of sign of E_{mix} with composition should indeed be expected for any size N of the reference truncated octahedron. In fact, in the extreme Cu-rich limit, E_{mix} will always be negative because, in a pure Cu truncated octahedron, the substitution of one Cu vertex atom by an Ag atom produces a negative mixing energy for all sizes of the truncated octahedron. On the contrary, in the extreme Ag-rich limit, the substitution of one Ag atom with a Cu atom, whose best position is subsurface [155] also according to DFT calculations [113], produces a positive mixing energy. Therefore, since the two extremes have opposite signs, there must be at least one change of sign in between. With increasing size, the Cu-rich composition range in which E_{mix} is negative shrinks. We expect that the position of the minimum of E_{mix} shifts approximately as N_{surf}/N, where N_{surf} is the number of surface atoms because we found the lowest values of E_{mix} in correspondence to the structures with a Cu core surrounded by a monolayer-thick Ag shell. N_{surf} can be estimated as the number of surface atoms in an elemental truncated octahedron rescaled by $(r_{Cu}/r_{Ag})^2$ to account for size mismatch. This estimate gives $N_{surf}/N = 0.364, 0.294$ and 0.245 for $N = 586, 1289$ and 2406, which correspond well to the minima of E_{mix} in Fig. 4.13.

To deal with point iii) we considered the optimization of $N = 586$ by three different approaches. The first approach is full global optimization of shape and chemical ordering

from random initial configurations, whose results have been already discussed before. The second approach is a *seeded* optimization which starts from a truncated octahedron with random chemical ordering and used only exchange moves. In this second approach, the cluster shape can change only because of local minimization. In the third approach, the seeded optimization uses mainly exchange moves but with a relatively small percentage (10-20%) of shape-changing moves. The results of the three approaches are compared in Fig. 4.14. In the seeded searches with exchange moves only, E_{mix} is negative below $N \simeq 400$, in qualitative agreement with the results of the symmetry-constrained optimizations of Ref. [145, 146], but with somewhat lower values, indicating that the absence of symmetry constraints may allow a somewhat better optimization. However, this is not the main issue, because this type of optimization itself is often not satisfactory at all. In fact, the inclusion of a relatively small percentage of shape-changing moves in the seeded searches can lead to major improvements, especially in the intermediate composition range, producing fcc structures with much more regular shape and better chemical ordering, whose energy is often very close to that obtained by full global optimization. For example, structures (a) and (b) of Fig. 4.14 at composition $Ag_{234}Cu_{352}$ were obtained by exchanges only and by exchanges and Brownian moves together, respectively. Structure (a) presents a quite rough surface exposing some Cu patches. Structure (b) has a smooth surface containing Ag atoms only. As a result, structure (b) is lower in energy than (a) by almost 13 eV. For Cu-rich and Ag-rich compositions, the results of chemical ordering optimization are closer to those of full optimization [156, 157].

Therefore the answer to point iii) is no in many cases. The optimization of chemical ordering alone at fixed geometrical structures is often unable to lead to low-energy structures in AgCu because the search often remains trapped in unphysical high-energy shapes. Even if the optimization of chemical ordering alone starts with the correct motif, the final results may turn out to be quite unsatisfactory. The equilibrium statistical weight of structures such as that of Fig. 4.14 (a) is completely negligible, and its shape is quite far from any physically sensible structure which may be produced by the kinetics of a true growth process. We believe that these findings can be generally extended to systems in which atomic species present relevant size mismatch, for example AgNi, AgCo, AuCo, AuCu, AuRh, AuPt, and AuNi.

In summary, we have proposed two new algorithms (FL and FLH algorithms) for the full global optimization of nanoalloys. In these algorithms, there are different BH walkers with specific roles – the flying walker, the landing walker, and (in FLH only) the hiking walker. These walkers act together to ensure a wide exploration of different shapes together with a deep refinement of chemical ordering.

The effectiveness of FL and FLH has been tested in the optimization of a few systems, for sizes from a few ten to a few thousand atoms. The tests have revealed that both FL and FLH are more efficient than other approaches available in the literature. FLH shows some advantages over FL for what concerns the exploitation task, since it is able to better optimize chemical ordering within the global minimum geometric structure. On the other hand, FL shows a somewhat better performance in exploration of different funnels than that of the global minimum. These differences are due to the different balance between exploration and exploitation moves in the two algorithms. We believe that an effective strategy when dealing with a new system could be to run searches by both algorithms.

Further improvement in efficiency may be expected by using multiple flying walkers running in parallel, each with its individual landing (and eventually hiking) walker. In systems with tendency to intermixing, such as AuCu and PtNi, other possible improvements in efficiency could be looked for by implementing more efficient schemes for homotop search [146] instead of random exchanges.

Our results have also shown that the optimization of shape and chemical ordering together is indeed necessary in many cases, since the optimization of chemical ordering alone at fixed shape (apart from local relaxations) may lead to unphysical results. This is especially true for intermediate compositions in systems with size mismatch between the atomic species.

Finally, the study of AgCu nanoalloys for sizes up to 4000 atoms has shown that the bulk-like regime, in which the optimal structures are fragments of the fcc lattice common to both metals, is not yet attained for sizes of a few thousand atoms, since icosahedral structures are found as the lowest in energy for several compositions. This behaviour is quite different from that of elemental Ag and Cu nanoparticles, in which icosahedra are already largely unfavorable for sizes above a few hundred atoms.

Chapter 5

Stabilisation of tetrahedral clusters induced by alloying

It is well known that many of the physical and chemical properties of metallic nanoparticles depend on the specific arrangement of their atoms [13]. As we discussed in Chapter 1, the most common shapes for face-centered cubic metal nanoparticles are truncated octahedra [100], decahedra and icosahedra [147, 158]. Recently, other types of structures based on different symmetries have been object of intense research due to their unique properties. An exceptional example is given by nanoparticles exhibiting tetrahedral (Th) symmetry [159–162]. In many experiments, these NPs have shown remarkable catalytic [10, 163–167] as well as optical [168–170] properties. Besides, we recall that tetrahedra are the building blocks of multi-twinned NPs, such as decahedra and icosahedra [90]; their study, then, is of primary importance. Unfortunately, metal nanoparticles showing tetrahedral symmetry are known to be energetically favored only for very small sizes and unstable for larger sizes – a feature that constitutes a drawback for practical applications.

Actually, tetrahedral structures are known to be stable (i.e. known to be the lowest-energy structures) at DFT level of accuracy, only up to a few atoms, i.e. the famous case of Au_{20} [171]. Larger tetrahedra can grow as non-equilibrium, meta-stable structures starting from octahedral seeds [172]. Another notable tetrahedral structure was found by Leary and Doye in 1999 [173]. In that work, they found that a tetrahedral structure with $N = 98$ atoms is the global minimum for the Lennard-Jones atomistic potential. The Leary tetrahedron can be constructed by building a 19-atom tetrahedron (which is a 20-atom regular tetrahedron without one vertex) on each of the four facets of a regular 20-atom tetrahedron, for a total of 56 atoms. The remaining 42 atoms are placed in six hexagonal patches on the naked edges of the starting 20-atom tetrahedron. The stability of the Leary tetrahedron was also proved

for some compositions of the PtPd Gupta atomistic force field [174], but not confirmed at DFT level, for which an attempt was made considering Au-Pd clusters [175].

In this Chapter, we discuss the result of a work [176], where we show that a different family of structures based on tetrahedral symmetry can be stabilized even at DFT level up to $N = 180$ atoms (~ 1.6 nm), thanks to the mixing of Pd and Pt metals. In particular, these clusters consist of symmetrically truncated tetrahedra with additional hexagonal islands placed in stacking fault positions on the four facets of the starting tetrahedron. We derived the series of geometric magic numbers of these clusters, which gives the number of atoms for the structures with different types of hexagonal islands. Global optimization searches within an atomistic potential model of PtPd showed that the tetrahedral structures can be stabilized for intermediate compositions of these nanoalloys, even when they are not the most stable structures of elemental clusters. Then, these results were confirmed also by DFT calculations for the magic sizes 59, 100 and 180. Finally, we showed thanks to a thermodynamic analysis provided by HSA that PtPd tetrahedral nanoalloys can be stable in temperature, even above room temperature. As a consequence of all these results, our calculations indicate that some tetrahedral metal nanoparticles are the lowest-energy structures in a size range that is actually wider than what was already known. Other than that, we remark that PtPd nanoparticles owe their interest to the exceptional catalytic activity that was shown to be superior than that of pure metals for several reactions [177–180].

5.1 Structural analysis of PtPd truncated tetrahedra

The family of structures that is object of this research is composed of truncated tetrahedra that have four stacking fault islands on their facets. Some examples are shown in Fig. 5.1 for different sizes ($N = 59$, 100 and 180) and compositions. The structure with $N = 59$ atoms (see Fig. 5.1) can be constructed by truncating the four vertices from the regular 34-atom tetrahedron, and by adding four regular hexagonal patches in stacking fault on each of the four facets. This structure was already found by Doye and Wales in 1995 [181], as the global minimum for the Morse atomistic potential. The structure with $N = 100$ atoms (see Fig. 5.1) was previously found by Manninen and Manninen in 2002, as the global minimum for two atomistic models based on the coordination numbers [182]. This structure can be obtained by truncating the four vertices from the 56-atom regular tetrahedron, and completed by adding four irregular hexagons as stacking fault islands on each of the four facets. We did not find any result for tetrahedral structures for $N = 180$ in the literature. This structure, see Figs. 5.1 and 5.2(a), is built by cutting four 4-atom tetrahedra from the apexes of the regular 116-atom tetrahedron, and by finally placing four regular hexagonal patches in stacking

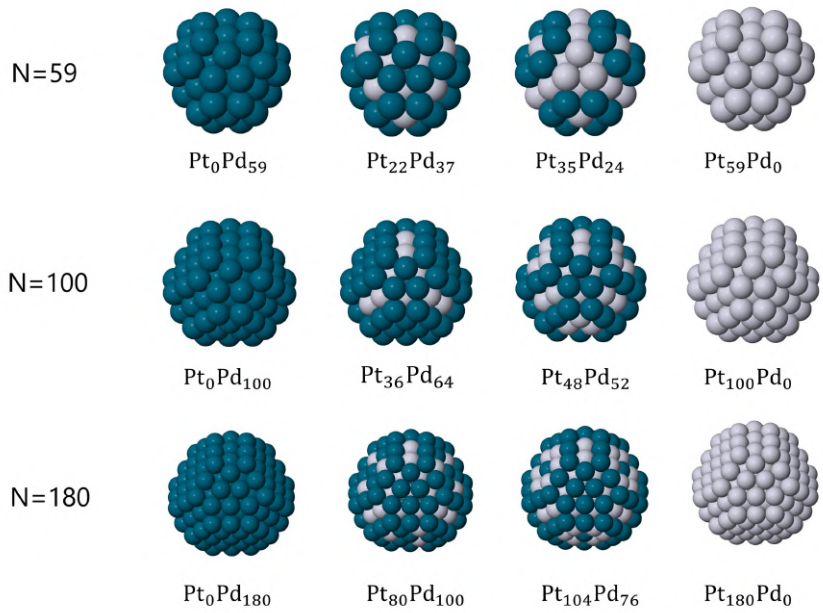

Fig. 5.1 Examples of truncated tetrahedra with both regular and irregular stacking fault islands. Reproduced from [176]. Copyright © 2023 The Authors. Published by American Chemical Society.

fault on the four facets. We note that for all mixed compositions, the arrangement of the two chemical species is always the same. In particular, Pt atoms lie almost entirely in the core of the nanoparticles, whereas Pd atoms tend to occupy the surface shell where they can accomodate into low-coordination sites; ultimately, they also take place in to some of the inner sites at the center of the NPs. Eventually, as can be seen in Fig. 5.1, Pt atoms in excess are located inside the hexagonal stacking fault islands. The surface segregation of palladium is consistent with previous numerical simulations [4, 183–185] and experiments [186–189]. To our knowledge, the stability of any of these structures at DFT level was never proved. In the following we derive the new series of magic numbers for these structures, referring to Fig. 5.2 for a schematic visualization of the proof.

In fcc stacking, a regular tetrahedron with a given edge of n atoms, is composed of n equilateral triangles with edges of increasing size from 1 (the vertex) to n (the base). Thus, the total number of atoms in a tetrahedron is given by

$$N_{tet} = \sum_{m=1}^{n} \frac{m(m+1)}{2} = \frac{1}{6}(n^3 + 3n^2 + 2n) \tag{5.1}$$

since the number of atoms in a equilateral triangle having m atoms in its edge is exactly $m(m+1)/2$. If at each vertex of the tetrahedron, a cut of length n_{cut} is made, the total number

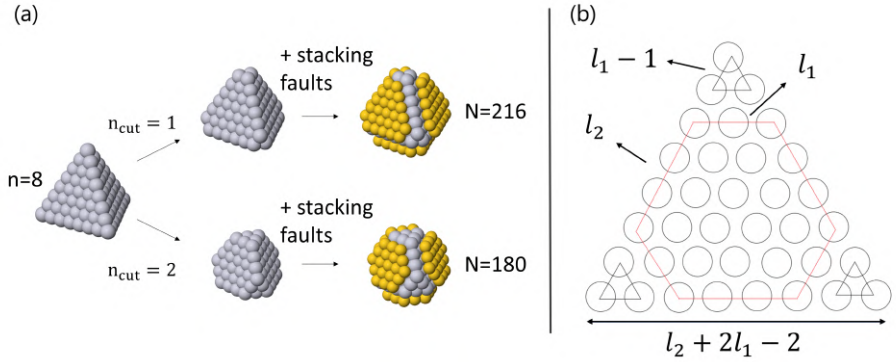

Fig. 5.2 (a) Two examples of different cuts from the same tetrahedral seed and (b) schematic representation of an irregular hexagon for the calculation of the number of atoms in stacking fault islands. Reproduced from [176]. Copyright © 2023 The Authors. Published by American Chemical Society.

of atoms in a regularly truncated tetrahedron is therefore given by

$$N_{tet}^{trunc} = \frac{1}{6}(n^3 + 3n^2 + 2n) - \frac{2}{3}(n_{cut}^3 + 3n_{cut}^2 + 2n_{cut}) \tag{5.2}$$

Stacking faults can be either regular or irregular hexagons. For the calculation of the number of atoms of an irregular hexagon we refer to Fig. 5.2 (b). Let l_1 and l_2 be the two side lengths of the irregular hexagon. Then, to calculate the total number of atoms, it is sufficient to take the size of the triangle and subtract three times the size of the small triangles created by the cuts. Then

$$N_{sf} = \frac{1}{2}(l_2 + 2l_1 - 2)(l_2 + 2l_1 - 1) - \frac{3}{2}l_1(l_1 - 1) \tag{5.3}$$

is the number of atoms of an irregular-hexagon stacking fault island. If we place such island on one of the four facets of the truncated tetrahedron, as in Fig. 5.2 (a), we have to make the substitution $l_1 - 1 = n_{cut}$ and $l_2 = n - 2n_{cut} - 1$. This is equivalent to say

$$N_{sf} = \frac{1}{2}n(n-1) - \frac{3}{2}n_{cut}(n_{cut} + 1) \tag{5.4}$$

Finally we are given the number of a regularly truncated tetrahedron with irregular stacking fault islands:

$$N = N_{tet}^{trunc} + 4N_{sf} = \frac{1}{6}(n^3 + 15n^2 - 10n) - \frac{2}{3}(n_{cut}^3 + 12n_{cut}^2 + 11n_{cut}) \tag{5.5}$$

which gives for example $N = 100$ for $n = 6$ and $n_{cut} = 1$, $N = 116$ for $n = 7$ and $n_{cut} = 2$.

Regular hexagons in stacking fault islands are obtained when $l_1 = l_2$, or $n_{cut} = (n-2)/3$. In this case, the total number of atoms is given by

$$N = \frac{1}{486}(69n^3 + 855n^2 - 414n + 744) \tag{5.6}$$

which gives the magic series $N = 59, 180, 394, ...$ for $n = 5, 8, 11, ...$

5.2 Energetic considerations: T=0 K

In order to assess the stability of these magic tetrahedral clusters, we first performed unseeded and seeded global optimization searches by using a Gupta atomistic potential for PtPd interactions. The parameters of the potential were taken from [190] and reported in Appendix B.

We considered Pt_mPd_{N-m} nanoalloys with $N = 59, 100$ and 180. In particular, for $N = 59$ we set $m = 0, 22, 23, 24, 35, 59$, for $N = 100$ we set $m = 0, 36, 40, 48, 52, 100$ and for $N = 180$ we set $m = 0, 80, 104, 180$. During global optimizations, the exploration of the potential energy surface of the systems allowed us to collect also other structures that are in competition, i.e. close in energy with truncated tetrahedra. The main competing structural motif is decahedral. Some examples of this and other competing structures can be found in Fig. 5.3.

Subsequently, we performed DFT relaxations of the competing clusters coordinates found by the global optimization searches. All calculations were made by using the Quantum Espresso open-source software [191]. We used two different exchange-correlations functionals: Perdew-Burke-Ernzerhof (PBE) [192] and the Local Density Approximation (LDA) [66]. The convergence thresholds for the total energy, total force, and for electronic calculations were set to 10^{-4} Ry, 10^{-3} Ry/a.u. and 5×10^{-6} Ry respectively. We used a periodic cubic cell, whose size was set to 25 Å for $N = 59$ NPs and 30 Å for $N = 100$ and $N = 180$ NPs. Cutoffs for wavefunction and charge density were set as suggested by the following pseudopotentials that we used: Pt.pbe-n-kjpaw_psl.1.0.0.UPF, Pd.pbe-n-kjpaw_psl.1.0.0.UPF, Pt.pz-n-kjpaw_psl.1.0.0.UPF and Pd.pz-n-kjpaw_psl.0.2.2.UPF for PBE and LDA respectively. They are currently available at https://pseudopotentials.quantum-espresso.org/legacy_tables/ps-library/ and https://dalcorso.github.io/pslibrary/.

Finally, we computed energy differences for all the sizes and compositions studied. The results of all calculations are summarized in Fig. 5.4.

For pure metals, decahedra and tetrahedra are always in competition for the Gupta potential ($|\Delta E| < 0.05$ eV), but not for DFT calculations, for which Dh are always favored

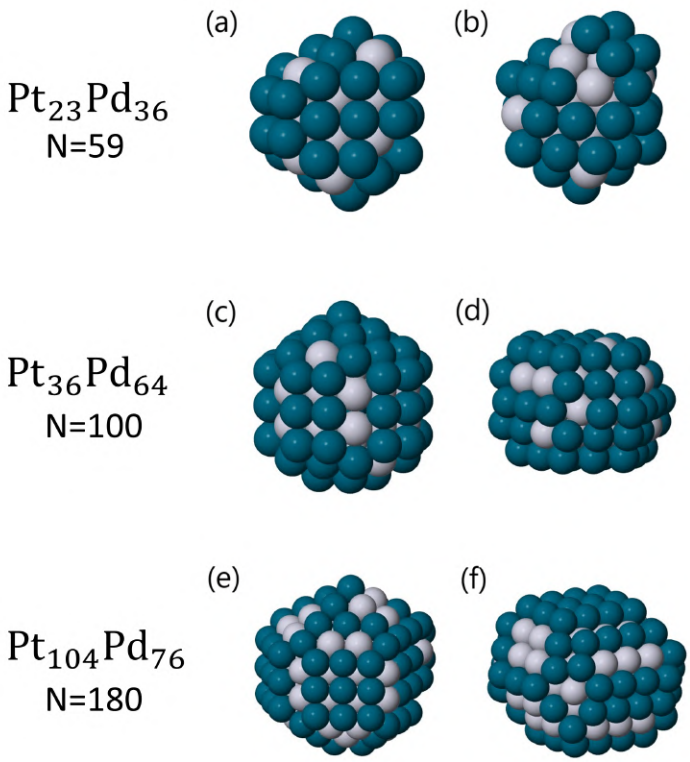

Fig. 5.3 (a) Decahedral and (b) icosahedral NP for $Pt_{23}Pd_{36}$. (c) Decahedral and (d) twin structure for $Pt_{36}Pd_{74}$; (e) decahedral and (f) twin structure for $Pt_{104}Pd_{76}$. Reproduced from [176]. Copyright © 2023 The Authors. Published by American Chemical Society.

consistently for both exchange-correlation functionals. The only exception is Pt_0Pd_{100}, for which even at DFT level the two structural motifs are in close competition.

For mixed compositions, tetrahedra are generally stabilized. In the case of $N = 59$, tetrahedra are favored for two of the four compositions tested: $Pt_{22}Pd_{37}$ and $Pt_{23}Pd_{36}$. For $Pt_{24}Pd_{35}$ composition, the Gupta potential strongly favors the tetrahedral motif, while DFT calculations agree about their competition ($|\Delta E| < 0.08$ eV for both exchange-correlation functionals). Finally, only in the case of $Pt_{35}Pd_{24}$, decahedra are consistently favored at DFT level, in contrast with the atomistic calculation. In the case of $N = 100$, tetrahedra are strongly favored at DFT level, whereas the Gupta potential tends to prefer the decahedral motif, but still with a small energy difference. Finally, for larger NPs ($N = 180$), tetrahedra are consistently favored both at atomistic and DFT level for at least one composition, i.e. $Pt_{104}Pd_{76}$. For the other mixed composition, the face-centered cubic motif is preferred at DFT level, the tetrahedron being favored instead by the atomistic potential.

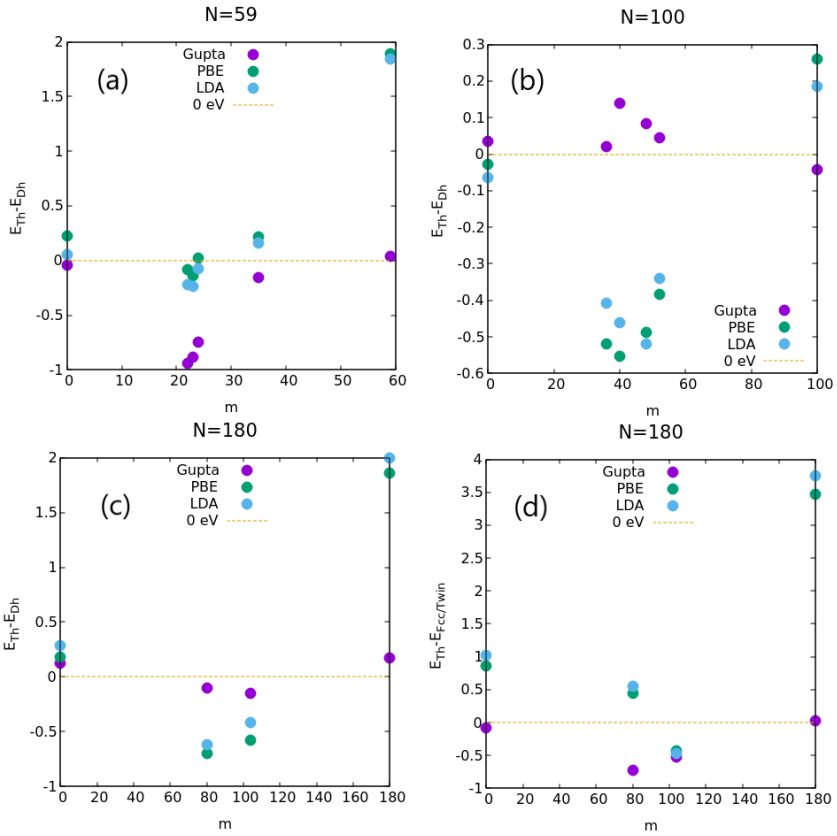

Fig. 5.4 Energy differences between best tetrahedron and best decahedron for (a) $N = 59$, (b) $N = 100$ and (c) $N = 180$. Energy differences between best tetrahedron and best fcc/twin structure for $N = 180$. For all sizes and compositions, we considered atomistic Gupta potential and two different exchange-correlations functionals: PBE and LDA. Reproduced from [176]. Copyright © 2023 The Authors. Published by American Chemical Society.

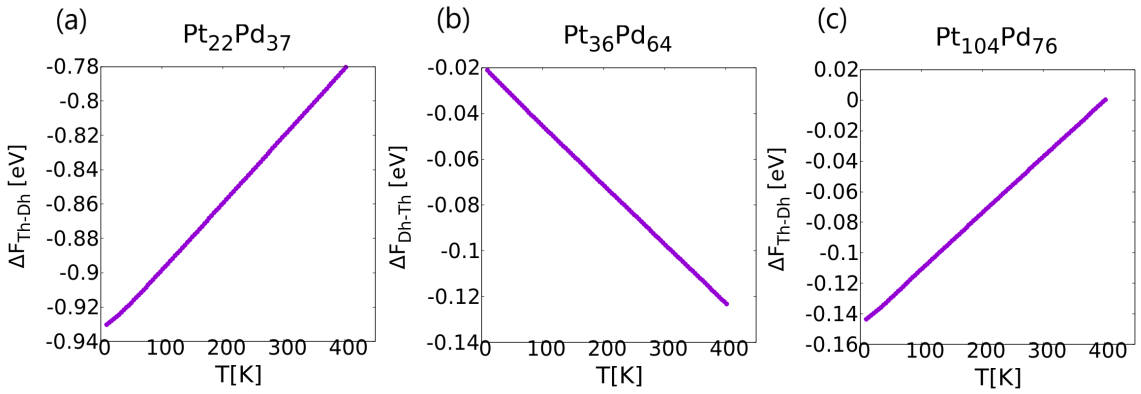

Fig. 5.5 Free-energy differences for one mixed composition at each size. (a) $Pt_{22}Pd_{37}$ for $N = 59$, (b) $Pt_{36}Pd_{64}$ for $N = 100$ and (c) $Pt_{104}Pd_{76}$ for $N = 180$. Reproduced from [176]. Copyright © 2023 The Authors. Published by American Chemical Society.

5.3 Energetic consideration: 0<T<400 K

The stability of some of the previously shown Dh and Th structures was studied for other temperatures than 0K, by estimating free energy differences thanks to the HSA, as explained in section 3.2.4. Results for the free-energy differences between Dh and Th are shown in Fig. 5.5. We decided to measure free energy differences from the structure having lower potential energy: $\Delta F_{a-b} = F_a - F_b$ where $E_a < E_b$.

For all cases, the entropic effects tend to stabilize the decahedral motif for increasing temperatures. In fact, $\Delta F = F_{Th} - F_{Dh}$ increases when Th is favored (Fig. 5.5 (a) and (c)) at 0K, and $\Delta F = F_{Dh} - F_{Th}$ decreases when Dh is favored at 0K (Fig. 5.5 (b)). We notice, however, that for the case of $Pt_{22}Pd_{37}$ and $Pt_{104}Pd_{76}$, the increase of ΔF is not enough to change its sign, so that $\Delta F < 0$ for all temperatures at least up to room temperature. This means that, at least for the atomistic model, we can conclude that the truncated tetrahedron remains the most stable structural motif, even in this temperature range. In order to corroborate this fact, we performed short Molecular Dynamics run of $1\,\mu s$ at a constant temperature of 400 K for the three tetrahedral structure considered for free energy differences. In all three simulations, we did not observe any transition. In particular, we considered $Pt_{22}Pd_{37}$ for $N = 59$, $Pt_{36}Pd_{64}$ for $N = 100$ and $Pt_{104}Pd_{76}$ for $N = 180$. For all simulations, the number of time steps used for propagating the trajectories was fixed to $2{\cdot}10^8$. The value of the time step was set to 5 fs, so that all simulations lasted $1\mu s$. We used interatomic forces derived from the Gupta potential, the velocity-Verlet algorithm for integrating the equations of motion and the Andersen thermostat to simulate the canonical ensemble properties, as described in section 2.1.3. For all three simulations, we used the tetrahedral structure as initial configuration. In

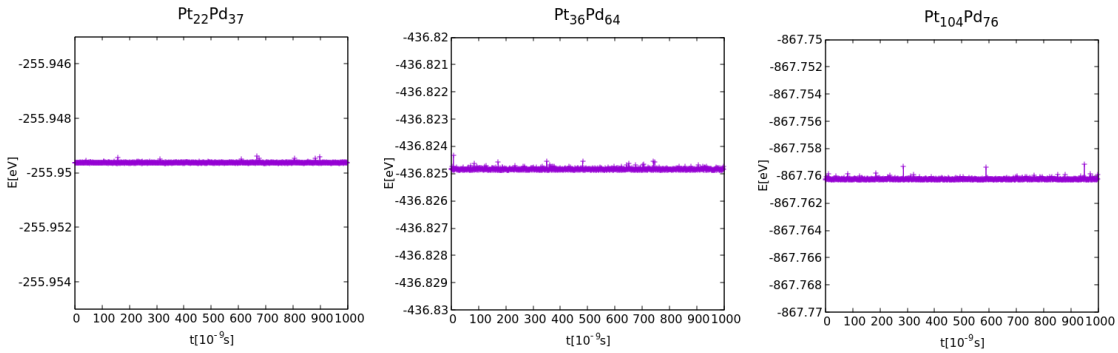

Fig. 5.6 Total energy of $Pt_{22}Pd_{37}$, $Pt_{36}Pd_{64}$ and $Pt_{104}Pd_{76}$ tetrahedron as a function of time. In all three cases, the value of the total energy is almost constant in time, a fact that suggests no transition towards other geometrical shapes occurred. In fact, this was verified by inspecting the structures given as output by the MD simulations.

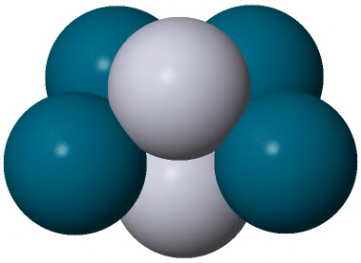

Fig. 5.7 Geometric structure and chemical ordering of Pt_2Pd_4. Reproduced from [176]. Copyright © 2023 The Authors. Published by American Chemical Society.

all cases, no transitions to other structures were observed. This demonstrate that, within the approximation given by the atomistic potential, tetrahedral structure are stable at 400K for at least $1\mu s$. We show in Fig. 5.6 the evolution of the total energy as a function of time for the three molecular dynamics simulations.

We speculate that the order of magnitude of entropic contributions in free energy differences ($\sim$ 0.1 eV at T=300K) could be the same also for DFT calculations. To this end, we performed DFT calculations for normal modes frequencies for a small Pt_2Pd_4 cluster, shown in Fig. 5.7, and compared them to those obtained by diagonalization of the dynamical matrix approximated by using the Gupta potential.

In particular, this structure was first relaxed with **pw.x** program of Quantum Espresso in a periodic cubic cell, whose size was set to 20 Å, using low convergence thresholds (10^{-6} Ry for total energy and 10^{-6} Ry/a.u. for total force, 10^{-15} Ry for electron self-consistent calculations). K-points were sampled using a 5x5x5 Monkhorst-Pack grid. We used PBE exchange-correlation functionals as described in section 5.2. Finally, the program **ph.x** was

	Gupta	DFT
ω_1	7.15	12.3
ω_2	10.7	15.1
ω_3	14.4	16.1
ω_4	16.5	17.7
ω_5	18.0	19.1
ω_6	21.8	19.9
ω_7	23.7	21.3
ω_8	23.8	24.0
ω_9	24.4	28.4
ω_{10}	32.4	32.1
ω_{11}	39.4	36.6
ω_{12}	47.2	41.4

Table 5.1 Normal modes vibrations as calculated by Gupta and DFT. Reproduced from [176].

used for estimating frequencies of normal modes at gamma point. In the Table 5.1 we report the 12 non-zero normal modes, units are in 10^{12} rad/s, for both Gupta and DFT calculations.

5.4 Discussion

A question that arises naturally is what are the causes of the stabilization of tetrahedal nanoparticles induced by the alloying of the two metals. It is our belief that the main reason of this result originates from a combined effect of i) the limited availability of competing shapes other than tetrahedra at a given size and ii) the choice of the right composition for the tetrahedral shape. In fact, by properly selecting the right amount of the two metals, one can build the tetrahedral nanoparticles in such a way that all palladium atoms decorate the four stacking fault islands – entirely or partially, as can be seen in Fig. 5.1 – as well as the four triangular facets of the tetrahedron that are left exposed after the cut of the vertices. Some of the palladium may also be included in the central sites of the NPs. This chemical arrangement is the best for these tetrahedral shapes. In addition, it turns out that such composition is not the best one for the other competing shapes, such as decahedra and twin structures. For example, even for the decahedral shape at size $N = 100$ – which is a very good one since it is only missing one vertex from the perfectly symmetric 101-atom Marks decahedron – the four compositions used for our calculations, $Pt_{36}Pd_{64}$, $Pt_{40}Pd_{60}$, $Pt_{48}Pd_{52}$ and $Pt_{52}Pd_{48}$ are not the optimal ones for decorating the decahedral shape.

$Pt_{22}Pd_{37}$		
Bond	Dh	Th
Pt-Pt	66	60
Pd-Pd	69	60
Pt-Pd	105	120

$Pt_{52}Pd_{48}$		
Bond	Dh	Th
Pt-Pt	192	198
Pd-Pd	70	72
Pt-Pd	177	168

$Pt_{104}Pd_{76}$		
Bond	Dh	Th
Pt-Pt	418	432
Pd-Pd	115	120
Pt-Pd	319	288

Table 5.2 Number of Pt-Pt, Pd-Pd and Pt-Pd bonds for Th and Dh structures in $Pt_{22}Pd_{37}$, $Pt_{52}Pd_{48}$ and $Pt_{104}Pd_{76}$. Reproduced from [176]. Copyright © 2023 The Authors. Published by American Chemical Society.

In order to gain more quantitative insights on the possible reasons for the stabilization of tetrahedral nanoparticles, we calculated the occurrence of Pt-Pt, Pt-Pd and Pd-Pd bonds, as well as coordination numbers for atoms in some of the competing isomers. The results of the calculations for the number of different bonds are reported in Table 5.2. For example, in $Pt_{22}Pd_{37}$, both decahedral and tetrahedral structures have a total of 240 bonds. The truncated tetrahedron has 60 Pt-Pt and 60 Pd-Pd bonds, and 120 Pt-Pd bonds. The decahedral isomer has 66 Pt-Pt bonds, 69 Pd-Pd bonds and 105 Pt-Pd bonds. Two atoms are bonded if their distance is within 20% of the nearest-neighbours distance. For Pt-Pd bonds the nearest-neighbour distance is the arithmetic average of Pt-Pt and Pd-Pd nearest-neighbour distances. We used $d = 1.385$ Å and $d = 1.375$ Å for Pt-Pt and Pd-Pd respectively. We note that DFT overestimates bond lengths, in fact for PBE the calculated nearest-neighbours distances in the fcc lattice are $d = 1.414$ Å and $d = 1.399$ Å for Pt-Pt and Pd-Pd respectively; however, for the purpose of calculating bonds occurrences, this is not relevant. In general for both structures, Pt atoms are highly coordinated, within a range spanning 8 to 12 nearest neighbours for Dh and 9 to 12 for Th. Instead, Pd atoms are in general low-coordinated, but with a slight difference for the two structures. In Dh, Pd atoms can have 5 to 8 nearest neighbours, whereas for Th, the coordination number is either 6 or 7, the only exception being the atom in the center of the NP, having 12 nearest neighbours. In particular, 24 Pd atoms have coordination number equal to 6 in Th, whereas only 18 atoms have the same coordination in the Dh. A similar analysis was done for $Pt_{52}Pd_{48}$. The calculation of the number of bonds revealed that the Dh has 192 Pt-Pt bonds, 70 Pd-Pd bonds and 177 mixed Pt-Pd bonds. The Th has instead 198 Pt-Pt bonds, 72 Pd-Pd bonds and 168 Pt-Pd bonds. All 52 Pt atoms in Th have 9 to 12 nearest-neighbours, whereas in Dh, three Pt atoms have 8 nearest-neighbours. In Dh, Pd atoms have 6 to 8 nearest neighbours, in Th only 6 or 7. In particular, the Dh has 21 Pd atoms with coordination number equal to 6, whereas the Th has 24. Finally, we also analyzed $Pt_{104}Pd_{76}$. In this case, the Th has 432 Pt-Pt bonds, 120 Pd-Pd bonds and 288 Pt-Pd bonds. The Dh has 418 Pt-Pt bonds, 115 Pd-Pd bonds and 319 Pt-Pd bonds. The fcc structure has 409 Pt-Pt bonds, 107 Pd-Pd bonds and 319 mixed Pt-Pd

bonds. In Th, all 104 Pt atoms have 9 to 12 nearest neighbours, Pd atoms have 6 to 9. In particular, a total of 24 Pd atoms have coordination number equal to 6. In Dh, Pt atoms have 8 to 12 nearest-neighbours, Pd atoms have 6 to 8 nearest-neighbours, with only one Pd atom in core position having 12 nearest-neighbours. A total of 23 Pd atoms has coordination number equal to 6. Also in the fcc structure, Pt atoms have 9 to 12 nearest-neighbours. Pd atoms have 6 to 8 nearest-neighbours, 3 of them in core positions have 12. A total of 26 Pd atoms has coordination number equal to 6. All these results are coherent with the surface segregation tendency of palladium atoms. However, it is difficult to establish a clear correlation between the different bonds numbers or coordination numbers and the stability of tetrahedral structures. For example, in two out of the three cases considered here, the Th has a larger number of Pd atoms with the lowest possible coordination number - 6 - the exception being $Pt_{104}Pd_{76}$. Similarly, in two out of three cases, the tetrahedral structure has a larger number of Pt-Pt bonds. However, this is not the case for $Pt_{22}Pd_{37}$, suggesting that there are indeed other factors playing an important role in the final determination of the most stable structure. Therefore, we recommend to look for other stable tetrahedral PtPd nanoparticles by following these two steps:

1. choosing the size according to the two equations (5.5) and (5.6) that give the number of atoms of irregular and regular truncated tetrahedra, respectively

2. choosing the optimal composition by filling the core with Pt atoms, the hexagonal islands as well as the triangular facets with Pd atoms, and eventually by putting excess Pt atoms inside the hexagonal islands.

In conclusion, we showed that tetrahedral nanoparticles can be stabilized by alloying Pt and Pd. At 0K, this was demonstrated both at atomistic and ab-initio level, whereas the stability up to room temperature was only proven by atomistic calculations, even if normal mode frequencies as calculated by DFT for a small PtPd cluster seem to indicate that the stability at higher temperatures could also be confirmed at ab-initio level. We believe that the importance of our work is two-fold. From a theoretical point of view, we proved the stability of the tetrahedral structural motif at DFT level, up to a relatively large size ($N = 180$), showing that these structures can be recovered by a new series of magic numbers. From an experimental point of view, our results show that by mixing the two metals, one can in principle produce tetrahedral nanoparticles that are more stable than those made by pure metals, so that they should be more resistant against ageing under the action of a controlled environment and possibly less prone to shape changes during chemical reactions. In addition, we cannot exclude that the size limit of stable tetrahedral clusters can be further pushed forward, since we have not proved yet the stability of other tetrahedral clusters that are next

in the magic series. Moreover, we speculate that the effect of tetrahedral stabilization induced by the alloying of two metals can be extended also to other metal pairs, for which there are similar interactions between the two elements.

Chapter 6

Collective atomic rearrangements in the growth of silver nanoparticles revealed by atomistic simulations

An important issue in the growth of materials is the achievement of regular and smooth shapes. In the case of thin films, smooth structures can be obtained by layer-by-layer (LBL) growth, in which an atomic layer is mostly completed before a new one starts to grow on top of it. The conditions allowing LBL growth have been deeply studied and understood [193]. Obtaining such a regular growth for nanoscale objects, such as nanoparticles [194–197], introduces new challenges. In fact, nanoparticles present inequivalent adsorption sites (e.g. at edges and vertices) even when they are free of defects, and their growth is a fully three-dimensional phenomenon in which both structure and symmetry can dynamically change [90, 172, 198]. The equivalent of LBL growth for nanoparticles is shell-by-shell (SBS) growth [199–201], whose aim is not only to form regular and smooth shapes, but also to preserve the initial structural motif which acts as a template. In this respect, the growth of icosahedra is a paradigmatic example, since icosahedra are the shell structures *par excellence* [202–204]. A schematic representation of LBL and SBS growth is given in Fig. 6.1.

In thin films, LBL growth is obtained when there is an effective mobility between the different growing layers (*inter-layer* mobility) [205], which is insured by the surface diffusion of individual adatoms [193]. Some contributions from multi-atom processes are also possible, but they are in most cases exchange processes involving a few atoms or concerted displacements of small islands on the otherwise flat surface [206, 207]. In order to insure inter-layer mobility, a deposited atom must be able to diffuse on a flat terrace, in order to reach its border. Then, the atom must be able to cross the border to descend to the lower level. This is often the rate-limiting step for LBL growth, because step descent presents in most

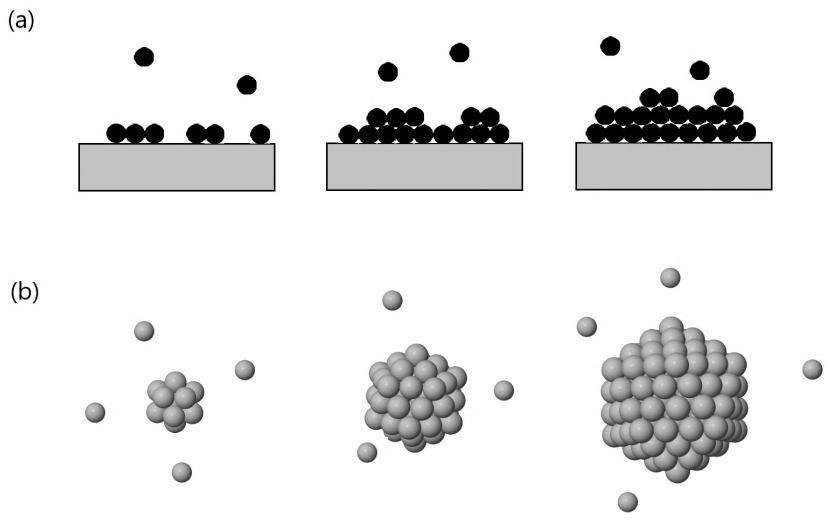

Fig. 6.1 (a) Two-dimensional schematic representation of a layer-by-layer growth of a thin film and (b) schematic representation of a shell-by-shell growth of an icosahedral nanoparticle.

cases an additional energy cost with respect to the surface diffusion alone. This additional contribution is known as the Ehrlich-Schwoebel (ES) barrier [208, 209]. In nanoparticles, the growth process is even more complex for the presence of surface strain [154] of edges and vertices, which make the growing shell prone to defects, that may hinder the perfect SBS growth and therefore must be eliminated before the completion of the growing shell.

In this chapter, we present the results of a collaboration with the experimental group headed by Prof. Andreazza (University of Orléans, France), about the growth of silver clusters. The experimental observations combined Grazing Incidence X-ray scattering at wide and small angles (GIWAXS and GISAXS, respectively), which allowed the real-time analysis of very large samples of growing clusters, and High Resolution Transmission Electron Microscopy (HRTEM) imaging of the final growth outcomes with atomic resolution. Numerical simulations of our group included MD simulations, which allowed to follow the growth mechanism atom by atom, complemented by DFT calculations to support the accuracy of the results.

Our computational investigations showed the formation of almost perfect Mackay icosahedra which takes place by a SBS mode. We show that this type of SBS growth is made possible by the occurrence of *intra-layer* rearrangement processes, which do not occur through the diffusion of individual adatoms on the surface, but through complex displacements of many atoms at the same time. These collective processes occur very rarely during the growth process, but their occurrence is crucial to make the SBS mode possible. Our

simulations therefore show that SBS growth is made possible by other crucial processes beyond interlayer mobility. The results of this collaboration are now published in Ref. [210]. In this work my main task was the performance and analysis of DFT calculations that were used to estimate the stability of different atomic islands on the surface of an icosahedral nanoparticle, a fundamental step to support the conclusions that arose from both experiments and atomistic simulations.

6.1 Nanoparticles growth at room temperature: experimental results and numerical simulations

The Ag metal nanoparticles were prepared at room temperature (RT) by UHV vapor deposition on thermally oxidized Si(100) wafers covered by an amorphous carbon layer or on amorphous carbon membrane self-supported on TEM Cu grids. Several samples were investigated to reveal the structural evolution with time at different activation temperature (from room temperature (RT) to 600 K) and to check the experimental result reproducibility. First of all, the growth of Ag clusters obtained by a Volmer-Weber vapor condensation mode [18, 211] was followed by X-ray scattering from nucleation to final growth in the range from some tens of atom to $D = 2.5$ nm in diameter. Fig. 6.2 (a) shows real-time monitoring of the structure of clusters under ultra-high vacuum during the deposition at 300 K, in a short acquisition time to simultaneously measure the scattered intensity at small and large angles, with a set of spectra collected every deposition of 15 atoms on average per cluster. The comparison with GIWAXS spectra simulations (Fig. 6.2 (b)) revealed that the icosahedral (Ih) structure of cluster is the main structure from ultra-small size ($D = 1.5$ nm) to larger size ($D = 2.5$ nm) with a size distribution ($\sigma(D)/D = 0.3$) measured by GISAXS. Note that an unambiguous determination of the structure for Ag clusters below 1-1.5 nm is not feasible by X-ray scattering analysis, because of the dominance of surface disordering at small size [212]. We note that our results agree with the X-ray scattering measurement performed on Ag particles obtained by vapor deposition in Ref. [213], which revealed the stability of Ih structure during the growth at RT of particles at increasing size from 1 to 3 nm. Note also that decahedral (Dh) and fcc truncated octahedral (TO) structures would not fit the spectra well, as clearly shown in Fig. 6.3.

In Fig. 6.4 the HRTEM images of a similar sample illustrating the structure and size distribution of Ag supported nanoparticles (NPs) prepared at 300 K up to an average diameter of 2.5 nm are shown. The samples shown in Fig. 6.4 were observed just after the end of NPs formation (i.e. several tens of minutes) by keeping the samples at RT. Fig. 6.4 (a) shows a

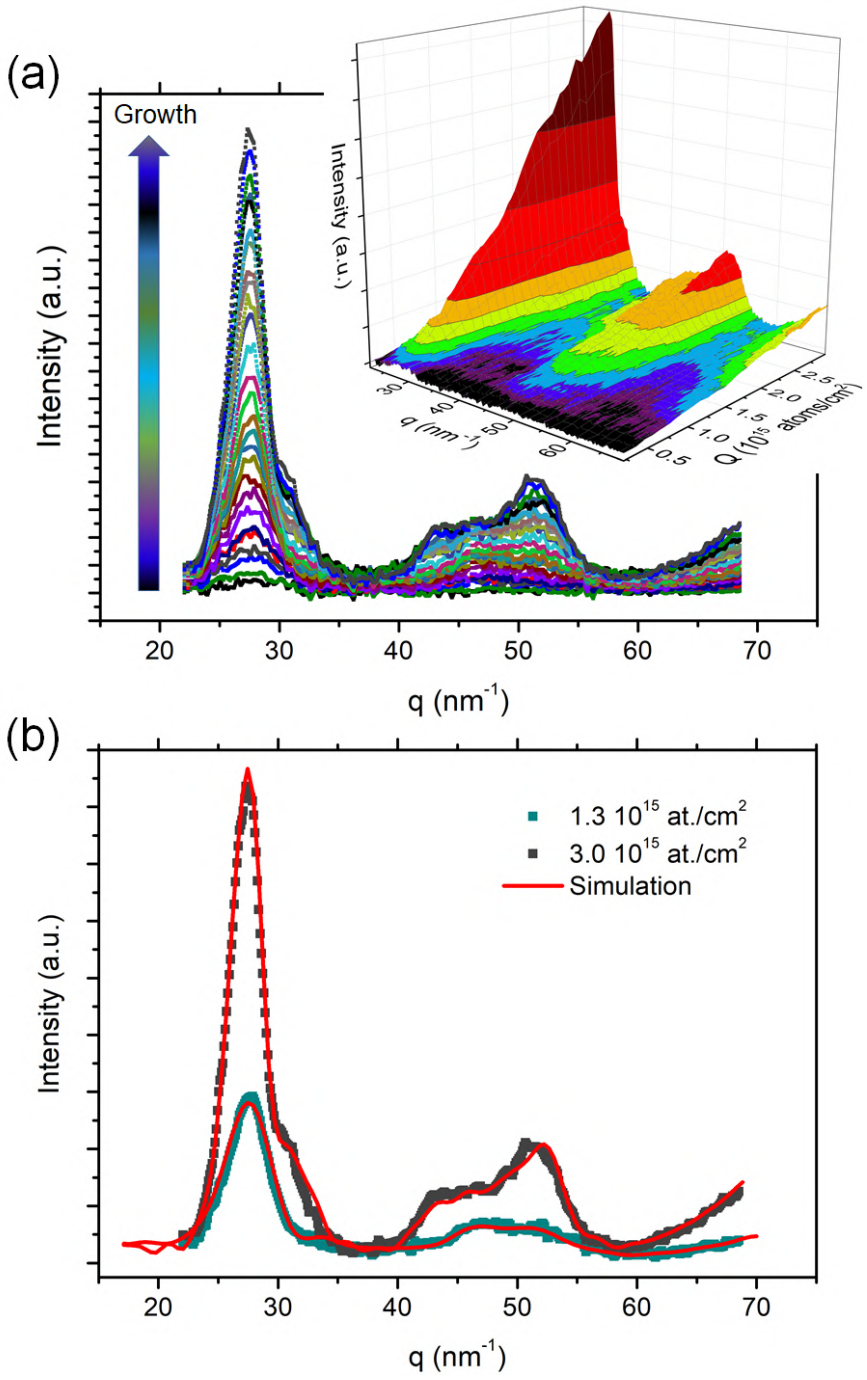

Fig. 6.2 (a) GIWAXS experimental spectrum of Ag nanoparticles assembly during the growth from 0.20 to 3.00·10^{15} deposited Ag atoms/cm^2 which corresponds to clusters from several tens to about 500 atoms, with a step of data collection of 15 atoms per cluster at each spectrum. In inset the 3D graph, (b) two representative GIWAXS experimental spectra obtained during the deposition (dots); with calculated spectra (red line) in a good agreement with experiments corresponding to a distribution of Ih structure models after energy minimization by MC simulation: for 1.3·10^{15} Ag atoms/cm^2 (about 1.5 nm size) from Ag_{55} to Ag_{309} models were used while for 3.0·10^{15} Ag atoms/cm^2 (about 2.5 nm size) from Ag_{309} to Ag_{923} models. Reproduced from Ref. [210] with permission from the Royal Society of Chemistry.

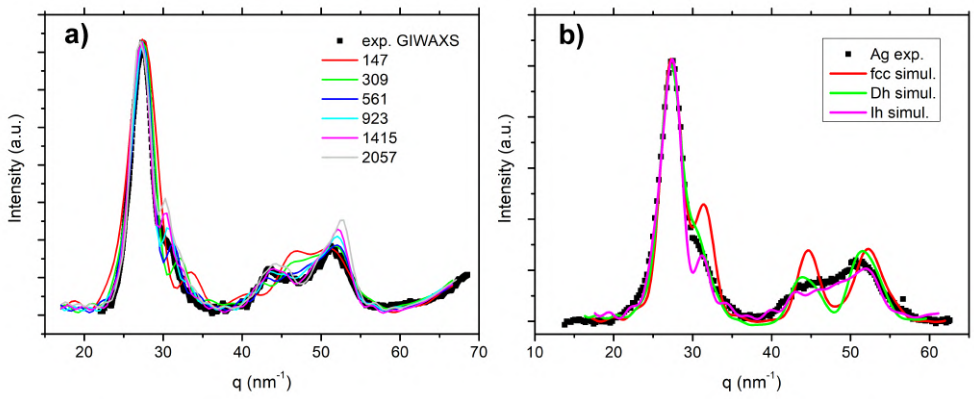

Fig. 6.3 Two GIWAXS experimental spectra of Ag nanoparticle assembly coming from 2 different measurements in the similar range of 2-2.5 nm in size during the UHV growth (dots), with the superimposition of simulations of several simulated spectra: a) from a set of Ih models of sizes from 147 to 2075 atoms, b) from an Ih model of 561 atoms, a Dh model of 585 atoms and a TOh model of 405 atoms (lines). Reproduced from Ref. [210] with permission from the Royal Society of Chemistry.

low magnification HRTEM image of Ag NPs, while Fig. 6.4 (b-d) show high magnification images of selected NPs in the Ih structural configuration, which is the majority structure in this condition. The associated simulated HRTEM images in the two-fold symmetry zone axis (Fig. 6.4 (f)) and in the three-fold zone axis (Fig. 6.4 (e)) correspond to the same orientations, structures of clusters and the same observation conditions than the experimental images of Fig. 6.4 (b,d) and Fig. 6.4 (c), respectively. In summary, both the real-time X-ray data and the HRTEM characterization of the final NPs clearly indicated that the growth at RT is dominated by icosahedral structures in the diameter range from 1 to 3 nm, corresponding to clusters containing from $\sim$100 to a few hundred atoms. The diameters of the ideal icosahedra of 147, 309 and 561 atoms (see section 1.1.2) fall in this range. We also note that the clusters shown in Fig. 6.4 (b,c,d) have almost perfect icosahedral shape, which very nicely agree with the simulated HRTEM images of ideal icosahedra of Fig. 6.4 (e,f).

In our growth simulations we started from the perfect Ih of size 147, which is in the low-size limit of the clusters observed in our experiments. The simulations were made in vacuum without any substrate. This choice, which allows to extend the time scale, is justified by the fact that this type of substrate has been shown to have quite small effects on the growth pathways of AgCo nanoalloys, which produce the same structural motifs as in vacuum [213, 214]. In particular, growth simulations were made by MD using the same type of procedure adopted in Ref. [172]. Atoms were deposited one by one isotropically from random directions on the initial 147-atom icosahedral seed. The deposition rate was set to 1 atom every 10 ns. Simulations were stopped when size 561 was reached. The equations of

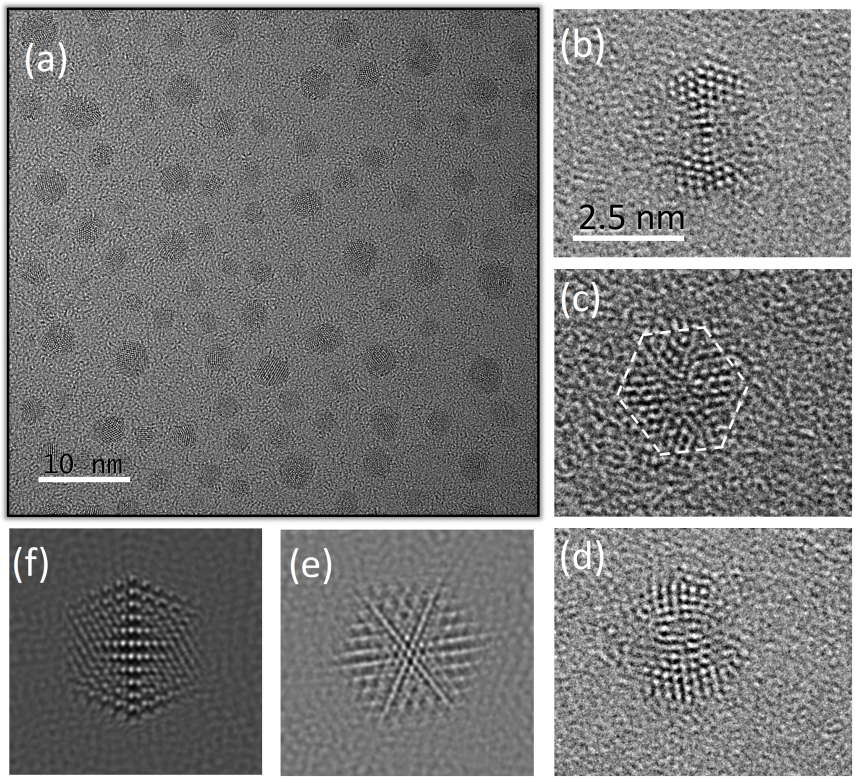

Fig. 6.4 HRTEM images obtained on Ag NPs just after deposition: (a) in a large area; (b),(c), (d) in high magnification with associated Ih simulated HRTEM images: (f) in two-fold symmetry zone axis corresponding to (b), (d) clusters and (e) in three-fold zone axis corresponding to (c) cluster. Reproduced from Ref. [210] with permission from the Royal Society of Chemistry.

motion were solved by the Velocity Verlet algorithm with a time step of 5 fs; temperature was kept constant by an Andersen thermostat, as described in section 2.1.3. For each temperature (300, 400 and 500 K), 5 independent simulations were made. In Fig. 6.5 (a1), (a2), (a3) we show snapshots from representative growth simulations at $T = 300$, 400 and 500 K, taken at the magic sizes 309 and 561, i.e. after depositing 162 and 414 atoms respectively. For every temperature, the clusters kept growing within the Ih motif. Moreover, we note that, even in the limited time scale of our MD simulations of $\sim$5 µs, the growth produced quite smooth structures which well replicated the original Ih template. At 500 K, nearly perfect icosahedra were observed at the magic sizes; at size 561, the second shell was almost completed in all simulations, with just 1-3 atoms on the third shell. At lower temperatures, more atoms were missing from the second shell (8-29 at 400 K and 18-38 at 300 K), which was however very regular and quite close to completion (88-96% at 400 K and 85-93% at 300 K).

In order to better quantify the shell-by-shell character of the template growth of icosahedra, we calculated the number of atoms in the shells as the growth proceeded. The results for the three different growth temperature are shown in Fig. 6.5 (b1), (b2), (b3). Panels (c1), (c2), (c3) report a magnification of the initial stages of the growth. Growth was reasonably shell-by-shell even at 300 K, since the third growing shell began to form when the first growing shell was already fully completed and the second growing shell contained about 170 atoms on a total of 252. At 400 K the shell-by-shell growth was already almost perfect, and at 500 K it essentially matched the ideal behaviour.

The smoothness of the shell-by-shell growth observed in our MD simulations indicates that inter-layer mobility of Ag atoms was activated. This behaviour might be expected, as ES barriers for descending steps on (111) surfaces are low in Ag [215]. However, as we will see in the following, the descent of Ag atoms at steps is not the only factor for achieving a smooth shell-by-shell growth. Other phenomena are even more important. We remark that the good quality of the final outcomes of MD simulations and of the experimentally observed icosahedra were in perfect agreement. We recall that the time scale of MD simulations is much shorter compared to the time scale of the growth experiments; therefore, in light of our very good simulation results, it is not surprising that no defective or amorphous structures were observed in the experiments, in which Ag clusters had much more time to rearrange and to eliminate defects than in simulations. In addition, we note that the time scale of our simulations was sufficient to overcome the rate-limiting step for a smooth and regular icosahedral growth; we expect that longer simulation times would not introduce significant changes or improvements.

A closer inspection of the initial stages of the growth allowed us to single out the occurrence of peculiar growth mechanisms. The non-zero values of yellow line in Fig.

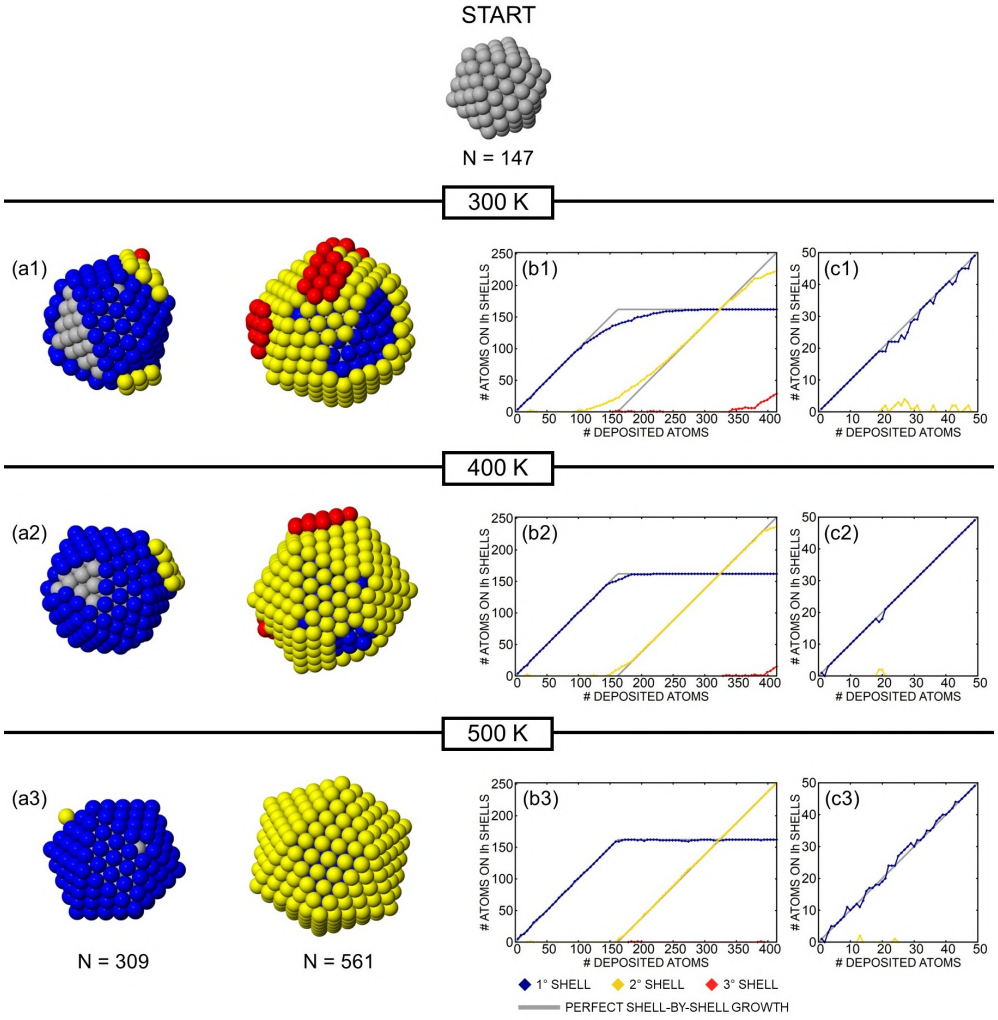

Fig. 6.5 Results from simulations at different temperatures. The snapshots in (a1), (a2) and (a3) are taken at icosahedral magic numbers ($N = 309$ and $N = 561$). Atoms belonging to the original 147-atoms Ih are coloured in grey; atoms in the first, second and third growing shells are coloured in blue, yellow and red, respectively. (b1), (b2), (b3): number of atoms on the first, second and third growing shell during the simulation, as a function of the number of deposited atoms. The behaviour of a perfect shell-by-shell growth is shown for comparison. In (c1), (c2) and (c3) we show the first steps of the growth of the first shell. Reproduced from Ref. [210] with permission from the Royal Society of Chemistry.

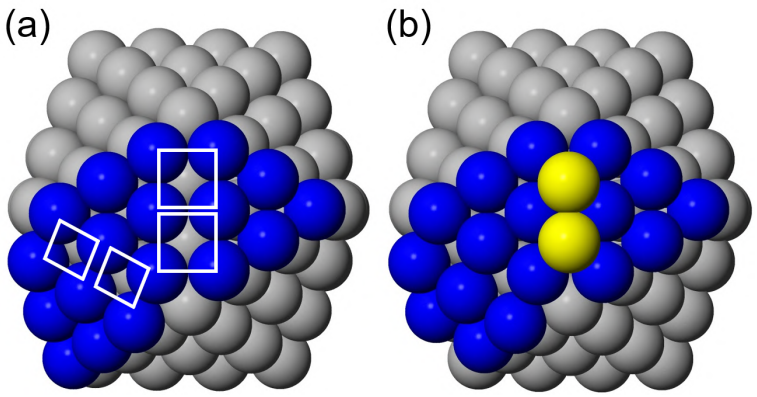

Fig. 6.6 Anti-Mackay incomplete first shell. (a) The shell is formed by three complete triangular islands on hcp stacking. The white squares enclose the fourfold adsorption sites. In (b) two atoms are adsorbed on these fourfold sites, thus belonging to the second growing layer. Reproduced from Ref. [210] with permission from the Royal Society of Chemistry.

6.5 (c1) indicate that a few atoms stayed in the second growing shell for some time, and then they descended down in the first growing shell. This presence of a few atoms in the second shell is due to the formation an anti-Mackay cap (see Fig. 6.6 (a)) in the first shell. Anti-Mackay islands are placed on hcp positions on top of the fcc tetrahedra that form the icosahedron [24]. These triangular faulted islands are energetically favourable on the facets of the icosahedron because on these facets there are more hcp than fcc adsorption sites [216]. When two triangular islands are formed on adjacent facets, they create fourfold sites in between which may act as trapping sites for new deposited atoms in the second shell (as in Fig. 6.6 (b)), especially at 300 K. We have studied the adsorption of one Ag atom on three-fold and four-fold sites above the anti-Mackay island, and we have found that four-fold sites are lower in energy by 0.35 eV. This means that Ag atoms have to cross an additional barrier of 0.35 eV for diffusing from four-fold to three-fold sites, which is considerably larger than the additional ES barrier for step descent, which can be lower than 0.2 eV [215]. Therefore, the rate-limiting step for a smooth shell-by-shell icosahedral growth is not the ES barrier at step borders, but it would be the escape from the four-fold sites of the anti-Mackay islands that are formed during the growth. As we shall see in the following, the arising picture is indeed more complex.

The formation of an incomplete anti-Mackay shell during the growth of nanoparticles was observed in all simulations. The anti-Mackay stacking is energetically favourable over the Mackay stacking only when the shell is incomplete. This point has been verified by calculating the energy difference ΔE between configurations with anti-Mackay and Mackay islands of different sizes, both by the Gupta potential and by DFT calculations, using with three different exchange-correlation functionals: PBE, [192], LDA [66] and PBEsol [217]. In the DFT

Table 6.1 Gupta and DFT values for the energy difference ΔE (in eV) between islands on anti-Macky and Mackay stacking. The corresponding configurations are given in Fig. 6.8. Reproduced from Ref. [210] with permission from the Royal Society of Chemistry..

	$N = 153$	$N = 159$	$N = 165$	$N = 171$
Gupta	-0.326	-0.650	-0.747	0.065
PBE	-0.512	-0.545	-0.291	0.179
LDA	-0.679	-0.796	-0.574	0.231
PBEsol	-0.583	-0.690	-0.451	0.229

calculations, the convergence thresholds for the total energy, total force, and for electronic calculations were set to 10^{-4} Ry, 10^{-3} Ry/a.u. and 5×10^{-6} Ry respectively. We used a periodic cubic cell, whose size was always set to 30 Å. Cutoffs for wavefunction and charge density were set to 45 and 181 Ry, respectively, for all three functionals. In particular we used the following pseudopotentials: Ag.pbe-n-kjpaw_psl.1.0.0.UPF, Ag.pbesol-n-kjpaw_psl.1.0.0.UPF and Ag.pz-n-kjpaw_psl.1.0.0.UPF for PBE, PBEsol and LDA respectively. They are currently available at https://pseudopotentials.quantum-espresso.org/legacy_tables/ps-library/ag. All DFT calculations were made by using the open-source software Quantum Espresso [191]. The results are reported in Table 6.1. All calculations very well agree in predicting that anti-Mackay islands are favourable up to size 165 (18 deposited atoms), and that the Mackay stacking becomes energetically favorable between sizes 165 and 171. This change in energetic stability is the driving force of the anti-Mackay to the Mackay arrangement which is always observed well before the completion of the shell.

Now we closely look at the transition anti-Mackay→Mackay (aM→M) transformation. In Figure 6.7 we report some snapshots from a simulation at 300 K. We note that the size and the shape of the growing shell at which the transformation occurred was different in all simulations. At 300 K, the size of the transforming shell was between 26 atoms (as in Fig. 6.7) and 89 atoms, and it was therefore larger than the size at which the stability reversal between the anti-Mackay and the Mackay arrangement was expected (i.e. between 18 and 24 atoms according to Table 6.1). The aM→M transformation occurred at smaller and smaller sizes with increasing temperature. A rich variety of transformation pathways can be collected. However, the pathways share some common features, that we describe with the help of Fig. 6.7.

In Fig. 6.7 (a), the anti-Mackay shell is made of three complete triangular islands (in red, yellow and blue), an incomplete island (orange), one adatom in an hcp site (white) and two more atoms on the edge (green). At variance with yellow atoms in Fig. 6.6 (b), the two green atoms belong to the first shell, as they are first neighbours of some atoms of the initial

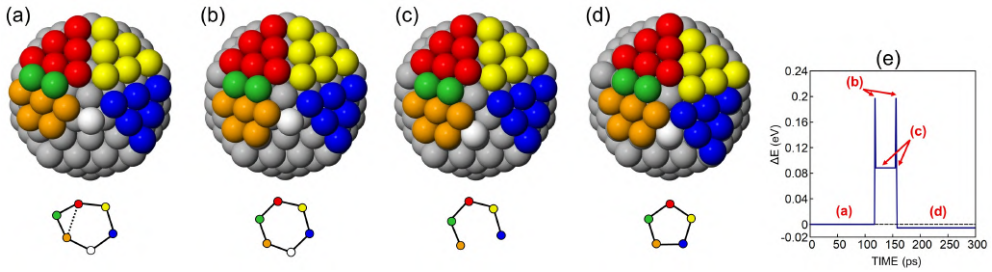

Fig. 6.7 Configurations of the local minima visited during a representative aM→M transformation of an incomplete shell. In (a) the anti-Mackay shell is formed by three complete triangular islands (red, yellow and blue), plus an incomplete islands (orange), one adatom in an hcp site (white) and two more atoms on the edge (green). (b) and (c) are the intermediate configurations of the transformation. In (d) the shell in Mackay stacking. Under each configuration, we show the atoms of the first shell that surround the vertex of the 147-atom icosahedral seed. In (e) we show the evolution of the potential energy after local minimization, taking a snapshot every picosecond. The zero level of the energy is that of configuration (a). The evolution of the potential energy shows that the cluster explores only four local minima with the sequence (a)→(b)→(c)→(b)→(c)→(d). We note that configurations in (c) and (d) are separated by 1 ps in the simulation, therefore the transformation can be only of collective character since there are no local minima visited in between. Reproduced from Ref. [210] with permission from the Royal Society of Chemistry.

seed. These atoms were initially in the second shell (as in Fig. 6.6 (b)) then they sank down to the first shell, slightly distorting the perfect anti-Mackay pattern. This was frequently observed in simulations at 300 K. We note that the presence of atoms in such configuration is not necessary for the aM→M transformation. However, the transformation was never observed when some atoms were placed on fourfold sites as in Fig. 6.6 (b); in order to make the transformation possible, those atoms must either sink down to the position of Fig. 6.7 (a) or leave the fourfold sites to accommodate elsewhere. In Fig. 6.7 (b) we show the first intermediate configuration of the aM→M transformation. This correspond to a very shallow local energy minimum, which is very quickly crossed, in 1-2 ps. We have however verified that (b) is a true local minimum with real vibrational frequencies. In this configuration, the green atoms have moved closer to the vertex, which now has six first neighbours on the surface. At the same time, the red and the orange islands are further shifted away from the anti-Mackay sites. The white atom has become highly compressed, and quickly moves to a nearby site, as in Fig. 6.7 (c). The lifetime of (c) is a little longer, of the order of tens of ps. Atoms around the fivefold vertex now form an open pentagon. In the (c)→(d) transition, the pentagon is closed and becomes regular, due to the displacement of all atoms in the shell, which perform a kind of concerted rotation around the vertex. In this configuration, the Mackay stacking is achieved. The energy in (d) is lower than in (c), and also slightly lower

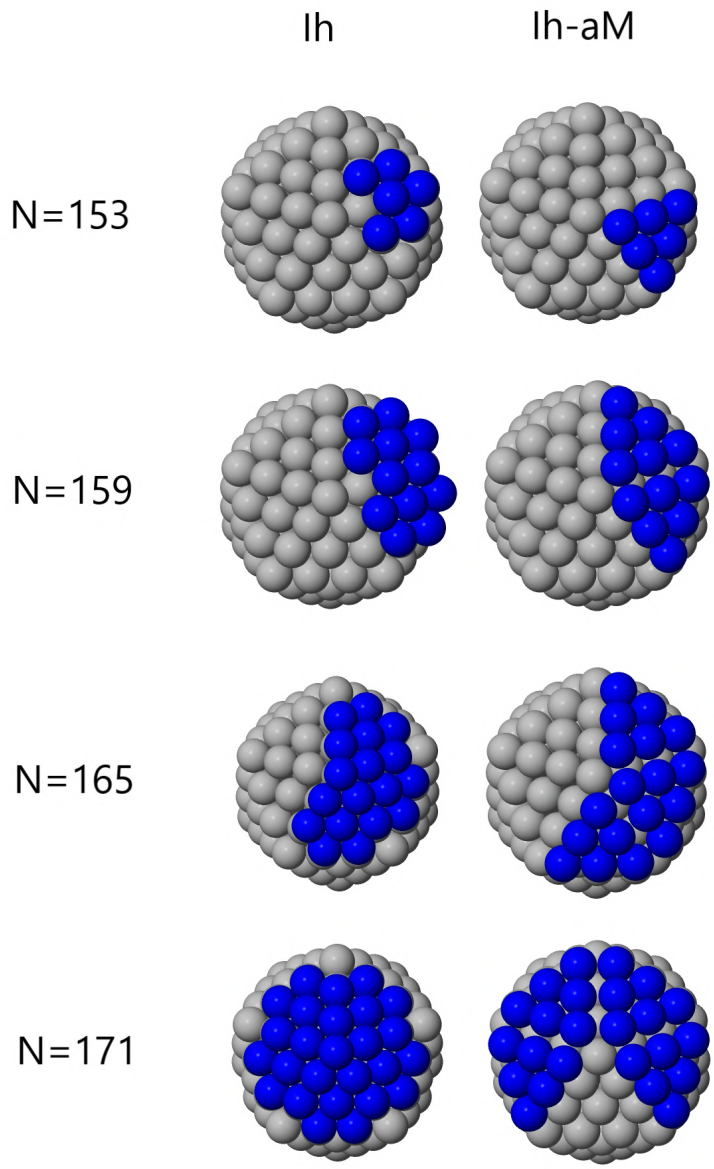

Fig. 6.8 Icosahedra of 147 atoms (grey spheres) covered by Mackay islands (left column) and anti-Mackay islands (right column). The atoms of the islands are coloured in blue. The energy differences between these structures are reported in Table 6.1. Reproduced from Ref. [210] with permission from the Royal Society of Chemistry.

than in (a). From this point on, growth continues within the Mackay stacking, as the newly deposited atoms attach to the Mackay growing shell and reinforce its stability. In the growth of the second shell we observe the same type of aM→M transformation. In this case, the evolution pathways are even more complicated, as disconnected anti-Mackay patches can form in different part of the shell, which may transform to Mackay independently.

To demonstrate that the aM→M transformation shown in Fig. 6.7(c,d) is indeed due to a single collective process, we compared the timescale of such process (of the order of few picoseconds) with the typical time that one Ag atom with thermal velocity would take to cross a nearest-neighbour distance (2.89 Å), which is 2 ps at 300 K. This means that the transitions shown in Fig. 6.7, and especially the transition from (c) to (d), were sudden and collective, because separate and consecutive diffusion processes of so many individual atoms would take much longer times. Therefore, the transition from (c) to (d) corresponds to the crossing of a single saddle point separating two adjacent local minima. The crossing of that saddle point corresponds to the collective displacement of many atoms all together.

Unfortunately, the experimental detection of the aM→M transformation is extremely challenging due to the small differences between the two icosahedral configurations. Specifically, the transformation cannot be detected by the X-ray scattering technique here employed. In fact, the simulated GIWAXS spectra of 165-atom anti-Mackay and Mackay icosahedra are hardly distinguishable (see Fig. 6.9), and the small differences are expected to be blurred by size-distribution effects in the nanoparticle sample. In Fig. 6.9, we compare the simulated GIWAXS spectra of two of the model icosahedral nanoparticles shown in Fig. 6.8. The two nanoparticles have the same size (165 atoms) and they differ for the stacking of the incomplete outer shell (Mackay or anti-Mackay). Differences in the spectra from single size models are weak, and are expected to become even weaker if the size distribution of the nanoparticle sample is taken into account. Therefore, it is is unrealistic to hope to detect the transformation from the anti-Mackay to the Mackay arrangement during the Ag nanoparticle growth by X-ray experimental measurement, as predicted by molecular dynamics simulations.

In summary, the experimental data clearly identified a continuous and regular growth within the icosahedral motif. The simulations very well agreed with the experimental findings. In addition, those simulations showed that a smooth SBS growth, which preserves the icosahedral template with few defects, was possible down to RT even within their time scale, which is much shorter than that of experiments. The MD simulations gave a clear picture of the underlying growth mechanisms at the atomic level. The typical growth pathway emerging from the simulations starts with the formation of faulted atomic islands, which are positioned on hcp (i.e anti-Mackay) stacking. These islands are energetically favourable in the initial stage of the shell formation, as also confirmed by the results of DFT calculations

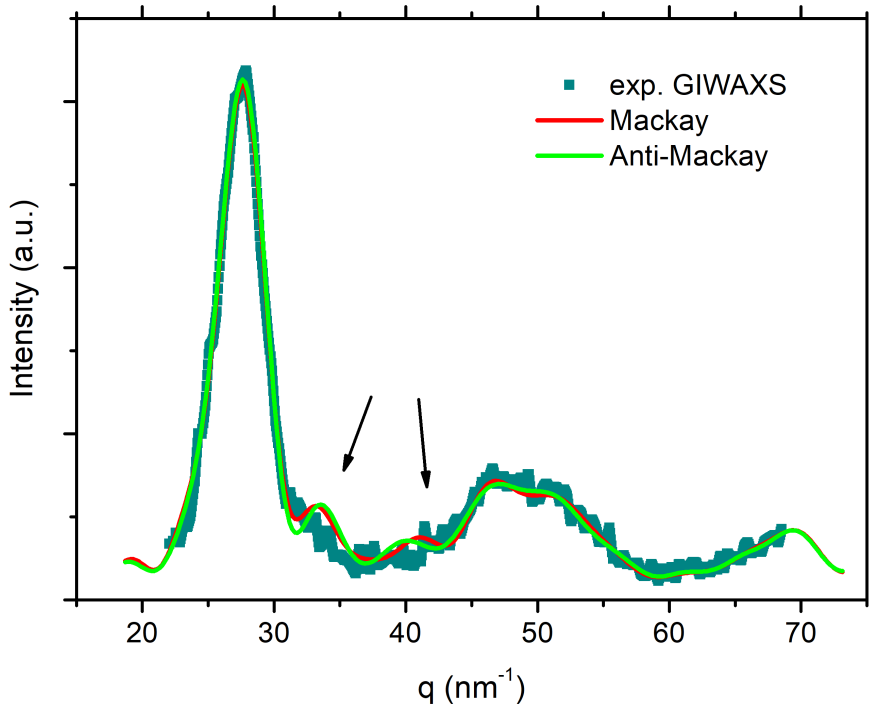

Fig. 6.9 Simulated GIWAXS spectra (lines) of icosahedra models of 165 atoms with Mackay and with Anti-Mackay shell. The main but weak differences are indicated by two arrows in the spectra. A GIWAXS experimental spectrum of Ag nanoparticle assembly measured during the UHV growth (dots) is showed for comparison. The range of 1.7 nm in average size is near the 165 atoms size of cluster models with Mackay and with Anti-Mackay shell used for the GIWAXS simulations. Reproduced from Ref. [210] with permission from the Royal Society of Chemistry.

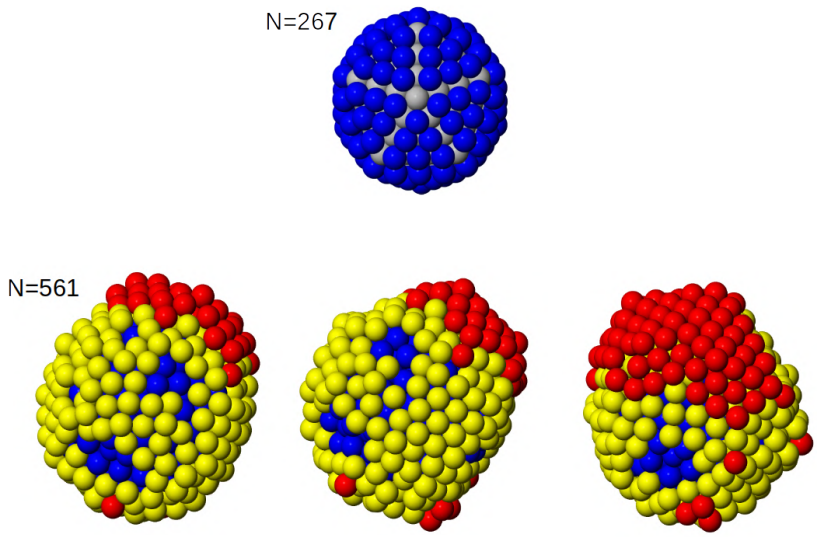

Fig. 6.10 Snapshots from a growth simulations starting from an anti-Mackay seed (top row) and leading to an irregular rough structure at size $N = 561$ (bottom row, the three snapshots show the same structure from different views). Temperature is 500 K and atoms are deposited with a rate of 1 atom every 10 ns. Grey spheres show the Mackay icosahedron of 147 atoms, which is covered by a first shell consisting of 20 perfect triangular islands on anti-Mackay stacking (blue atoms). These islands are not allowed to rearrange by keeping some of their atoms fixed. Yellow and red atoms belong to the second and third grown shell, respectively. Reproduced from Ref. [210] with permission from the Royal Society of Chemistry.

with three different exchange-correlation functionals. When the number of deposited atoms increases, the Mackay shell arrangement becomes energetically favourable instead. The anti-Mackay→Mackay transformation occurs at a glance by a collective displacement of many atoms, in some cases of all atoms in the top shell. These collective motions are not the most common diffusion events on the surface. In fact, the displacements of isolated adatoms are by far more frequent than the crucial collective events. The latter may occur only once before the completion of the shell, but, without them, growth would take a qualitatively different path. In our case, if anti-Mackay islands would persist, the cluster would grow towards a different and much rougher shape. In order to investigate this point, we have simulated the growth on top of an icosahedron with anti-Mackay outer shell whose atoms are kept fixed in order to suppress the aM→M transformation. The results are shown in Fig. 6.10. A perfect smooth regular growth on top of such anti-Mackay structure would lead to a pentakis-dodecahedral shape [148] instead of the experimentally observed Mackay icosahedron. As it is evident, the grown structures are far from being smooth and regular

even at 500 K because the fourfold adsorption sites between anti-Mackay islands act as adatom traps, which strongly slow down atomic mobility.

In the growth mechanism unveiled by our MD simulations, inter-layer mobility of individual adatoms is not sufficient for achieving a smooth and regular SBS growth. If several anti-Mackay islands are present, the rate-limiting process for SBS growth is not adatom descent from steps, as governed by the the ES barrier, but the escape of adatoms from fourfold trapping sites between the islands. As we have seen, the picture is far more complex, since atoms do not escape from such sites, but the anti-Mackay islands transform into a Mackay cap so that all trapping sites are cleared, and growth can proceed smoothly, since interlayer mobility on Mackay caps is quite fast.

In conclusion, our results show that the growth path towards smooth icosahedra is decided by a few rare collective events. Our findings are representative of the kinetics of pure silver clusters growing in the solid state and, as such, they reveal mechanisms that are likely common to other metallic nanoparticles growing in the same conditions. Indications in this sense come from the analysis of other experiments and simulations concerning the growth and evolution of different metallic clusters and nanoparticles [90, 172, 218–220]. If the growth procedure involves ligands that may change the diffusion kinetics of the atoms on the nanoparticle surface, other mechanisms might be activated. On the other hand, if growth takes place in the liquid phase and then metal droplets solidify after the completion of the growth, also in this case the formation processes may be quite different.

Conclusions

In this thesis we presented the development and application of novel computational techniques, especially designed for the study of metal nanoparticles and nanoalloys. The aim of this project was to improve the set of tools already present in order to increase the knowledge about these nanoscale systems, whose interest keeps growing due to their unique properties that are continuously exploited thanks to the combined advances in both theoretical and experimental researches. In this final chapter, we summarize the results obtained and discussed throughout the thesis. Moreover, we list some possible future perspectives for the continuation of this work.

- Development of computational techniques

  In Chapter 3, we stated the problem of the clustering of nanoparticle structures, that we recall briefly here. In many computer simulations that involve atomistic models for the investigation of nanoparticle properties, such as Molecular Dynamics and Global Optimizations, the output consists in a set of several structures described by atomic coordinates. The analysis of these sets of structures, often very large - up to some thousands of structures in some MD simulations - can be very hard and time-consuming to do by hand. In general, the structures can present a large variety of tiny differences that are difficult to detect by only using molecular modelling software. Grouping nanoparticles structures based on their geometric similarities is of fundamental importance because, in the post-processing stage of the above-mentioned numerical simulations, it is at the base of the applications of other algorithms for the extraction of physical and chemical properties. An example, that was used in this thesis more than once, is given by the Harmonic Superposition Approximation, that allows to estimate the probability of a given structural family as a function of temperature thanks to an approximation of the partition function. In the same chapter, we exposed a recipe for the solution of this clustering problem. We proposed a combination of Machine Learning techniques together with a clever description of nanoparticles structures which is derived from geometric principles only, thus being very general. In

particular, this description is based on the Common Neighbour Analysis, and it allows to encode the structural information of the nanoparticles in a high-dimensional vector. Principal Component Analysis is then used to reduce the dimension of these vectors, giving the opportunity to map the points in the data set from a high-dimensional space to a low-dimensional space. Finally, the use of a clustering algorithm based on a mixture of Gaussian probability distributions, subsequently validated by a score, allows to define the optimal subdivision of the data set into a group of structural families that have different geometrical properties. This pipeline was successfully applied to different systems of interest, including data from MD simulations of nanoparticles at high temperature. As a future perspective, the nanoparticle description based on the Common Neighbour Analysis could be enriched by some features that are specifically designed for discriminate between different chemical orderings, something that is missing in our actual method. In addition, different dimensionality reduction techniques could be used, such as autoencoders, which was successfully used in Ref. [221].

In Chapter 4, we presented two new algorithms for the global optimization of nanoalloys. Apart from the pure theoretical interest, the importance of the global optimization problem lies in the fact that the lowest-energy structures obtained as a solution to this problem are those expected to be found in an experiment conducted near thermodynamic equilibrium at low temperatures. Therefore, the results of a global optimization can be used as i) predictions of experimental outcomes and ii) validation of the atomistic model used. The two new algorithms that we propose are based on a variant of the Basin Hopping algorithm. In the standard Basin Hopping algorithm, a single walker is in charge of exploring the space in which the function that needs to be globally optimized is defined. The new algorithms proposed use instead multiple walkers that run in parallel and that exchange the configurations with themselves, by following specific criteria that were described in detail in that chapter. These new schemes perform better than the algorithms already present in the literature when tested on different systems, especially for nanoalloys, in which the full global optimization requires not only the geometry but also the chemical ordering to be optimized as well. In a future perspective, our two new algorithms could be equipped with an even more efficient recipe for the optimization of chemical ordering, such as those described in Ref. [146], from which they could benefit a further boost in the overall performance of exploration of the potential energy surface.

- Applications

In Chapters 5 and 6 we discussed the results obtained by the application of the computational techniques introduced in the previous chapters. In particular, in Chapter 5, we showed that there is a family of nanoalloys having tetrahedral symmetry which can be stabilized by the alloying of two metals. Tetrahedral nanoparticles are rather uncommon with respect to the more frequent structural motifs encountered, such as icosahedral, decahedral and truncated-octahedral ones. Experiments have demonstrated that some catalytic and optical properties are enhanced by the tetrahedral shape. However, metal nanoparticles possessing tetrahedral symmetry are usually grown as out-of-equilibrium structures and therefore their stability is relatively weak and easily perturbed; a fact which reflects the lack of this kind of structures as lowest-energy structures in theoretical calculations, if not for very few cases that are described in that chapter. The novelty of our result stands in the fact that we propose a series of tetrahedral nanoalloys as lowest-energy structures for some sizes and compositions. Thus, these findings suggest, at least in principle, that a class of stable tetrahedral nanoparticles could be produced for experiments in which this particular geometric feature is important to exploit some physical and chemical properties.

Finally, in Chapter 6, we reported the results of a collaboration with an experimental group about the study of the growth of silver nanoparticles. Experimental results supported by X-ray scattering and TEM analysis, suggest that the growth of silver nanoparticles is within the icosahedral motif. Our numerical simulations, consisting of MD runs supported by DFT calculations, show that this kind of growth is possible only when some collective atomic rearrangements take place, a very interesting phenomenon which was never detected in previous simulations.

In conclusion, we believe that the results obtained in this thesis give relevant insights in the research field on metal nanoparticles. We are also convinced that the new numerical techniques presented here will be beneficial in the future for the investigation of the properties of these systems.

References

[1] J. A. Alonso. *Structure and Properties of Atomic Nanoclusters*. Imperial College Press, 2005.

[2] R. L. Johnston. *Atomic and Molecular Clusters*. Taylor and Francis, 2002.

[3] R. Ferrando, J. Jellinek, and R. L. Johnston. "Nanoalloys: From Theory to Applications of Alloy Clusters and Nanoparticles". In: *Chem. Rev.* 108 (2008), pp. 845–910.

[4] D. Nelli, A. Krishnadas, R. Ferrando, and C. Minnai. "One-Step Growth of Core–Shell (PtPd)@Pt and (PtPd)@Pd Nanoparticles in the Gas Phase". In: *The Journal of Physical Chemistry C* 124 (2020), pp. 14338–14349.

[5] P. Andreazza, V. Pierron-Bohnes, F. Tournus, C. Andreazza-Vignolle, and V. Dupuis. "Structure and order in cobalt /platinum-type nanoalloys: from thin films to supported clusters". In: *Surf. Sci. Rep.* 70 (2015), pp. 188–258.

[6] D. Schooss, M. N. Blom, J. H. Parks, B. v. Issendorff, H. Haberland, and M. M. Kappes. "The Structures of Ag_{55}^{+} and Ag_{55}^{-}: Trapped Ion Electron Diffraction and Density Functional Theory". In: *Nano Letters* 5 (2005), pp. 1972–1977.

[7] T. Rapps, R. Ahlrichs, E. Waldt, M. M. Kappes, and D. Schooss. "On the Structures of 55-Atom Transition-Metal Clusters and Their Relationship to the Crystalline Bulk". In: *Angewandte Chemie International Edition* 52 (2013), pp. 6102–6105.

[8] D. M. Wells, G. Rossi, R. Ferrando, and R. E. Palmer. "Metastability of the atomic structures of size-selected gold nanoparticles". In: *Nanoscale* 7 (2015), pp. 6498–6504.

[9] G. Benetti, E. Cavaliere, R. Brescia, S. Salassi, R. Ferrando, A. Vantomme, L. Pallecchi, S. Pollini, S. Boncompagni, B. Fortuni, M. J. Van Bael, F. Banfi, and L. Gavioli. "Tailored Ag–Cu–Mg multielemental nanoparticles for wide-spectrum antibacterial coating". In: *Nanoscale* 11 (2019), pp. 1626–1635.

[10] R. Narayanan and M. A. El-Sayed. "Catalysis with Transition Metal Nanoparticles in Colloidal Solution: Nanoparticle Shape Dependence and Stability". In: *The Journal of Physical Chemistry B* 109 (2005), pp. 12663–12676.

[11] S. Mostafa, F. Behafarid, J. R. Croy, L. K. Ono, L. Li, J. C. Yang, A. I. Frenkel, and B. R. Cuenya. "Shape-Dependent Catalytic Properties of Pt Nanoparticles". In: *Journal of the American Chemical Society* 132 (2010), pp. 15714–15719.

[12] K. L. Kelly, E. Coronado, L. L. Zhao, and G. C. Schatz. "The Optical Properties of Metal Nanoparticles: The Influence of Size, Shape, and Dielectric Environment". In: *J. Phys. Chem. B* 107 (2003), pp. 668–677.

[13] R. Ferrando. *Structure and Properties of Nanoalloys*. Elsevier, 2016.

[14] F. Baletto and R. Ferrando. "Structural properties of nanoclusters: Energetic, thermodynamic, and kinetic effects". In: *Rev. Mod. Phys.* 77 (2005), pp. 371–423.

[15] Y. Wang, S. Xie, J. Liu, J. Park, C. Z. Huang, and Y. Xia. "Shape-Controlled Synthesis of Palladium Nanocrystals: A Mechanistic Understanding of the Evolution from Octahedrons to Tetrahedrons". In: *Nano Letters* 13 (2013), pp. 2276–2281.

[16] Z. W. Wang and R. E. Palmer. "Determination of the Ground-State Atomic Structures of Size-Selected Au Nanoclusters by Electron-Beam-Induced Transformation". In: *Phys. Rev. Lett.* 108 (2012), p. 245502.

[17] Z. Li, N. Young, M. D. Vece, S. Palomba, R. Palmer, A. Bleloch, B. Curley, R. Johnston, J. Jiang, and J. Yuan. "Three-dimensional atomic-scale structure of size-selected gold nanoclusters". In: *Nature* 451 (2008), pp. 46–48.

[18] J. Penuelas, P. Andreazza, C. Andreazza-Vignolle, H. Tolentino, M. D. Santis, and C. Mottet. "Controlling Structure and Morphology of CoPt Nanoparticles through Dynamical or Static Coalescence Effects". In: *Phys. Rev. Lett.* 100 (2008), p. 115502.

[19] D. Nelli, C. Roncaglia, R. Ferrando, and C. Minnai. "Shape Changes in AuPd Alloy Nanoparticles Controlled by Anisotropic Surface Stress Relaxation". In: *The Journal of Physical Chemistry Letters* 12 (2021), pp. 4609–4615.

[20] S. Ino. "Stability of Multiply-Twinned Particles". In: *J. Phys. Soc. Jpn.* 27 (1969), pp. 941–953.

[21] A. Howie and L. D. Marks. "Elastic strains and the energy balance for multiply twinned particles". In: *Phil. Mag. A* 49 (1984), pp. 95–109.

[22] A. L. Mackay. "A dense non-crystallographic packing of equal spheres". In: *Acta Crystallogr.* 15 (1962), pp. 916–918.

[23] I. A. Harris, R. S. Kidwell, and J. A. Northby. "Structure of Charged Argon Clusters Formed in a Free Jet Expansion". In: *Phys. Rev. Lett.* 53 (1984), p. 2390.

[24] D. Bochicchio and R. Ferrando. "Size-Dependent Transition to High-Symmetry Chiral Structures in AgCu, AgCo, AgNi, and AuNi Nanoalloys". In: *Nano Lett.* 10 (2010), pp. 4211–4216.

[25] E. Aprà, F. Baletto, R. Ferrando, and A. Fortunelli. "Amorphization Mechanism of Icosahedral Metal Nanoclusters". In: *Phys. Rev. Lett.* 93 (2004), p. 065502.

[26] N. Khan, A. Uhl, S. Shaikhutdinov, and H.-J. Freund. "Alumina supported model Pd-Ag catalysts: A combined STM, XPS, TPD and IRAS study". In: *Surf. Sci.* 600 (2006), p. 1849.

[27] J. Pirart, A. Front, D. Rapetti, C. Andreazza-Vignolle, P. Andreazza, C. Mottet, and R. Ferrando. "Reversed size-dependent stabilization of ordered nanophases". In: *Nature Communications* 10 (2019), p. 1982.

[28] D. Wang, H. Xin, R. Hovden, H. Wang, Y. Yu, D. Muller, F. DiSalvo, and H. Abruna. "Structurally ordered intermetallic platinum–cobalt core-shell nanoparticles with enhanced activity and stability as oxygen reduction electrocatalysts". In: *Nature Mater.* 12 (2013), p. 81.

[29] F. Cyrot-Lackmann and F. Ducastelle. "Binding Energies of Transition-Metal Atoms Adsorbed on a Transition Metal". In: *Phys. Rev. B* 4 (1971), pp. 2406–2412.

[30] R. P. Gupta. “Lattice relaxation at a metal surface”. In: *Phys. Rev. B* 23 (1981), p. 6265.

[31] V. Rosato, M. Guillopé, and B. Legrand. “Thermodynamical and structural properties of f.c.c. transition metals using a simple tight-binding model”. In: *Phil. Mag. A* 59 (1989), p. 321.

[32] D. Spanjaard and M.-C. Desjonqueres. *Concepts in surface physics*. Springer Verlag, 2002.

[33] F. Cleri and V. Rosato. “Tight-binding potentials for transition metals and alloys”. In: *Phys. Rev. B* 48 (1993), p. 22.

[34] M. J. López and J. Jellinek. “On the problem of fitting many-body potentials. I. The minimal maximum error scheme and the paradigm of metal systems”. In: *J. Chem. Phys.* 110 (1999), pp. 8899–8911.

[35] J. P. K. Doye and D. J. Wales. “Calculation of thermodynamic properties of small Lennard-Jones clusters incorporating anharmonicity”. In: *J. Chem. Phys.* 102 (1995), p. 9659.

[36] D. J. Wales. *Energy Landscapes*. Cambridge University Press, 2003.

[37] J. Zhang and V.-A. Glezakou. “Global optimization of chemical cluster structures: Methods, applications, and challenges”. In: *International Journal of Quantum Chemistry* 121 (2021), e26553.

[38] R. Srivastava. “Application of Optimization Algorithms in Clusters”. In: *Frontiers in Chemistry* 9 (2021).

[39] J. M. C. Marques, F. B. Pereira, J. L. Llanio-Trujillo, P. E. Abreu, M. Albertí, A. Aguilar, F. Pirani, and M. Bartolomei. “A global optimization perspective on molecular clusters”. In: *Philosophical Transactions of the Royal Society A: Mathematical, Physical and Engineering Sciences* 375 (2017), p. 20160198.

[40] R. Ferrando. “Determining the equilibrium structures of nanoalloys by computational methods”. In: *Journal of Nanoparticle Research* 20 (2018), p. 179.

[41] R. L. Johnston. “Evolving better nanoparticles: Genetic algorithms for optimising cluster geometries”. In: *Dalton Transactions* 2003 (2003), p. 4193.

[42] J. M. Dieterich and B. Hartke. “Improved Cluster Structure Optimization: Hybridizing Evolutionary Algorithms with Local Heat Pulses”. In: *Inorganics* 5 (2017).

[43] T.-E. Fan, Y.-R. Zhang, and W. Jiang. “A two-step optimization approach for structures investigation of Pd-Ir bimetallic nanoclusters”. In: *Computational Materials Science* 214 (2022), p. 111680.

[44] W.-H. Yang, Y.-M. Li, J.-X. Bi, R. Huang, G.-F. Shao, T.-E. Fan, T.-D. Liu, and Y.-H. Wen. “An Improved Self-Adaptive Differential Evolution with the Neighborhood Search Algorithm for Global Optimization of Bimetallic Clusters”. In: *Journal of Chemical Information and Modeling* 62 (2022), pp. 2398–2408.

[45] J. M. Dieterich and B. Hartke. “Error-Safe, Portable, and Efficient Evolutionary Algorithms Implementation with High Scalability”. In: *Journal of Chemical Theory and Computation* 12 (2016), pp. 5226–5233.

[46] R. Mikhov, V. Myasnichenko, L. Kirilov, N. Sdobnyakov, P. Matrenin, D. Sokolov, and S. Fidanova. "On the Problem of Bimetallic Nanostructures Optimization: An Extended Two-Stage Monte Carlo Approach". In: *Recent Advances in Computational Optimization: Results of the Workshop on Computational Optimization WCO 2020*. Springer Verlag, 2022, pp. 235–250.

[47] Y.-R. Liu, Y. Jiang, S. Jiang, C.-Y. Wang, and T. Huang. "Global minima optimization via mirror-rotation transformation". In: *Phys. Rev. Res.* 4 (2022), p. L042045.

[48] C. Panosetti, K. Krautgasser, D. Palagin, K. Reuter, and R. J. Maurer. "Global Materials Structure Search with Chemically Motivated Coordinates". In: *Nano Letters* 15 (2015).

[49] D. Schebarchov and D. J. Wales. "Communication: A new paradigm for structure prediction in multicomponent systems". In: *J. Chem. Phys.* 139 (2013), p. 221101.

[50] D. Schebarchov and D. J. Wales. "Structure Prediction for Multicomponent Materials Using Biminima". In: *Phys. Rev. Lett.* 113 (2014), p. 156102.

[51] Z. Li and H. A. Scheraga. "Monte-Carlo-minimization approach to the multiple-minima problem in protein folding". In: *Proc. Natl. Acad. Sci. U.S.A.* 84 (1987), pp. 6611–6615.

[52] J. P. K. Doye and D. J. Wales. "Thermodynamics of Global Optimization". In: *Phys. Rev. Lett.* 80 (1998), p. 1357.

[53] R. H. Byrd, P. Lu, J. Nocedal, and C. Zhu. "A Limited Memory Algorithm for Bound Constrained Optimization". In: *SIAM Journal on Scientific Computing* 16 (1995), pp. 1190–1208.

[54] D. J. Wales and J. P. K. Doye. "Global optimization by Basin-Hopping and the Lowest Energy Structures of Lennard-Jones Clusters Containing up to 110 Atoms". In: *J. Phys. Chem. A* 101 (1997), pp. 5111–5116.

[55] G. Rossi and R. Ferrando. "Global optimization by excitable walkers". In: *Chem. Phys. Lett.* 423 (2006), pp. 17–22.

[56] M. P. Allen and D. J. Tildesley. *Computer Simulation of Liquids*. Clarendon, 1987.

[57] H. C. Andersen. "Molecular dynamics simulations at constant pressure and/or temperature". In: *The Journal of Chemical Physics* 72 (1980), pp. 2384–2393.

[58] F. Baletto, C. Mottet, and R. Ferrando. "Molecular dynamics simulations of surface diffusion and growth on silver and gold clusters". In: *Surf. Sci.* 446 (2000), pp. 31–45.

[59] M. Born and R. Oppenheimer. "Zur Quantentheorie der Molekeln". In: *Annalen der Physik* 389 (1927), pp. 457–484.

[60] D. R. Hartree. "The Wave Mechanics of an Atom with a Non-Coulomb Central Field. Part I. Theory and Methods". In: *Mathematical Proceedings of the Cambridge Philosophical Society* 24 (1928), pp. 89–110.

[61] J. C. Slater. "The Self Consistent Field and the Structure of Atoms". In: *Phys. Rev.* 32 (1928), pp. 339–348.

[62] V. Fock. "„Selfconsistent field" mit Austausch für Natrium". In: *Zeitschrift für Physik* 62 (1930), pp. 795–805.

[63] D. R. Hartree and W. Hartree. “Self-consistent field, with exchange, for beryllium”. In: *Proceedings of the Royal Society of London. Series A - Mathematical and Physical Sciences* 150 (1935), pp. 9–33.

[64] P. Hohenberg and W. Kohn. “Inhomogeneous Electron Gas”. In: *Phys. Rev.* 136 (1964), B864–B871.

[65] W. Kohn and L. J. Sham. “Self-Consistent Equations Including Exchange and Correlation Effects”. In: *Phys. Rev.* 140 (1965), A1133–A1138.

[66] R. Parr and W. Yang. *Density-Functional Theory of Atoms and Molecules*. Oxford University Press, 1994.

[67] J. P. Perdew, J. A. Chevary, S. H. Vosko, K. A. Jackson, M. R. Pederson, D. J. Singh, and C. Fiolhais. “Atoms, molecules, solids, and surfaces: Applications of the generalized gradient approximation for exchange and correlation”. In: *Phys. Rev. B* 46 (1992), pp. 6671–6687.

[68] J. Perdew, K. Burke, and M. Ernzerhof. “Generalized Gradient Approximation Made Simple”. In: *Phys. Rev. Lett.* 78 (1997), pp. 1396–1396.

[69] I. N. Remediakis and E. Kaxiras. “Band-structure calculations for semiconductors within generalized-density-functional theory”. In: *Phys. Rev. B* 59 (1999), pp. 5536–5543.

[70] G.-T. Bae and C. M. Aikens. “Time-Dependent Density Functional Theory Studies of Optical Properties of Ag Nanoparticles: Octahedra, Truncated Octahedra, and Icosahedra”. In: *The Journal of Physical Chemistry C* 116 (2012), pp. 10356–10367.

[71] N. Durante, A. Fortunelli, M. Broyer, and M. Stener. “Optical Properties of Au Nanoclusters from TD-DFT Calculations”. In: *The Journal of Physical Chemistry C* 115 (2011), pp. 6277–6282.

[72] E. Engel and R. Dreizler. *Density Functional Theory – An Advanced Course*. Springer-Verlag, 2011.

[73] E. Kaxiras. *Atomic and Electronic Structure of Solids*. Cambridge University Press, 2003.

[74] J. Thijssen. *Computational Physics*. Cambridge University Press, 2007.

[75] T. Hastie, R. Tibshirani, and J. Friedman. *The Elements of Statistical Learning*. Springer, 2009.

[76] Y. S. Abu-Mostafa, M. Magdon-Ismail, and H.-T. Lin. *Learning From Data*. AML-book.com, 2012.

[77] V. N. Vapnik. *The Nature of Statistical Learning Theory*. Springer, 2000.

[78] J. MacQueen. “Some methods for classification and analysis of multivariate observations”. In: *Proceedings of the fifth berkeley symposium on mathematical statistics and probability*. 1967.

[79] C. M. Bishop. *Pattern Recognition and Machine Learning*. Springer, 2006.

[80] K. P. Murphy. *Machine Learning: A Probabilistic Perspective*. The MIT Press, 2012.

[81] S. Lloyd. “Least squares quantization in PCM”. In: *IEEE Transactions on Information Theory* 28 (1982), pp. 129–137.

[82] D. Arthur and S. Vassilvitskii. “K-Means++: The Advantages of Careful Seeding”. In: *Proceedings of the Eighteenth Annual ACM-SIAM Symposium on Discrete Algorithms*. USA, 2007, pp. 1027–1035.

[83] P. J. Rousseeuw. “Silhouettes: A graphical aid to the interpretation and validation of cluster analysis”. In: *Journal of Computational and Applied Mathematics* 20 (1987), pp. 53–65.

[84] L. Kaufman and P. Rousseeuw. *Finding Groups in Data: An Introduction To Cluster Analysis*. Wiley, 1990.

[85] G. Schwarz. “Estimating the Dimension of a Model”. In: *The Annals of Statistics* 6 (1978), pp. 461–464.

[86] R. Tibshirani, G. Walther, and T. Hastie. “Estimating the number of clusters in a data set via the gap statistic”. In: *Journal of the Royal Statistical Society: Series B (Statistical Methodology)* 63 (2001), pp. 411–423.

[87] K. P. F.R.S. “LIII. On lines and planes of closest fit to systems of points in space”. In: *The London, Edinburgh, and Dublin Philosophical Magazine and Journal of Science* 2 (1901), pp. 559–572.

[88] R. Cangelosi and A. Goriely. “Component retention in principal component analysis with application to cDNA microarray data”. In: *Biology Direct* 2 (2007), p. 2.

[89] I. Jolliffe. *Principal Component Analysis*. Springer, 2002.

[90] E. y. El koraychy, C. Roncaglia, D. Nelli, M. Cerbelaud, and R. Ferrando. “Growth mechanisms from tetrahedral seeds to multiply twinned Au nanoparticles revealed by atomistic simulations”. In: *Nanoscale Horiz.* 7 (2022), pp. 883–889.

[91] El koraychy, El yakout, Nelli, Diana, Roncaglia, Cesare, Minnai, Chloé, and Ferrando, Riccardo. “Growth of size-matched nanoalloys - a comparison of AuAg and PtPd”. In: *Eur. Phys. J. Appl. Phys.* 97 (2022), p. 28.

[92] E. Lavagna, Z. P. Güven, D. Bochicchio, F. Olgiati, F. Stellacci, and G. Rossi. “Amphiphilic nanoparticles generate curvature in lipid membranes and shape liposome–liposome interfaces”. In: *Nanoscale* 13 (2021), pp. 16879–16884.

[93] C. Roncaglia, D. Rapetti, and R. Ferrando. “Regression and clustering algorithms for AgCu nanoalloys: from mixing energy predictions to structure recognition”. In: *Phys. Chem. Chem. Phys.* 23 (2021), pp. 23325–23335.

[94] C. Roncaglia. “Gaussian mixture model for the unsupervised classification of AgCu nanoalloys based on the common neighbor analysis”. In: *Eur. Phys. J. Appl. Phys.* 97 (2022), p. 11.

[95] C. Roncaglia and R. Ferrando. “Machine Learning Assisted Clustering of Nanoparticle Structures”. In: *Journal of Chemical Information and Modeling* 63 (2023), pp. 459–473.

[96] A. J. Parker, G. Opletal, and A. S. Barnard. “Classification of platinum nanoparticle catalysts using machine learning”. In: *Journal of Applied Physics* 128 (2020), p. 014301.

[97] A. J. Parker and A. S. Barnard. “Machine learning reveals multiple classes of diamond nanoparticles”. In: *Nanoscale Horiz.* 5 (2020), pp. 1394–1399.

[98] F. Pedregosa, G. Varoquaux, A. Gramfort, V. Michel, B. Thirion, O. Grisel, M. Blondel, P. Prettenhofer, R. Weiss, V. Dubourg, J. Vanderplas, A. Passos, D. Cournapeau, M. Brucher, M. Perrot, and E. Duchesnay. "Scikit-learn: Machine Learning in Python". In: *Journal of Machine Learning Research* 12 (2011), pp. 2825–2830.

[99] F. Baletto, C. Mottet, and R. Ferrando. "Growth of Three-Shell Onionlike Bimetallic Nanoparticles". In: *Phys. Rev. Lett.* 90 (2003), p. 135504.

[100] F. Baletto, R. Ferrando, A. Fortunelli, F. Montalenti, and C. Mottet. "Crossover among structural motifs in transition and noble-metal clusters". In: *J. Chem. Phys.* 116 (2002), p. 3856.

[101] F. Pittaway, L. O. Paz-Borbón, R. L. Johnston, H. Arslan, R. Ferrando, C. Mottet, G. Barcaro, and A. Fortunelli. "Theoretical Studies of Palladium-Gold Nanoclusters: Pd-Au Clusters with up to 50 Atoms". In: *The Journal of Physical Chemistry C* 113 (2009), pp. 9141–9152.

[102] M. Turner, V. B. Golovko, O. P. H. Vaughan, P. Abdulkin, A. Berenguer-Murcia, M. S. Tikhov, B. F. G. Johnson, and R. M. Lambert. "Selective oxidation with dioxygen by gold nanoparticle catalysts derived from 55-atom clusters". In: *Nature* 454 (2008), pp. 981–983.

[103] G. J. Hutchings. "Nanocrystalline gold and gold palladium alloy catalysts for chemical synthesis". In: *Chem. Commun.* (2008), pp. 1148–1164.

[104] E. Cottancin, G. Celep, J. Lermé, M. Pellarin, J. R. Huntzinger, J. L. Vialle, and M. Broyer. "Optical Properties of Noble Metal Clusters as a Function of the Size: Comparison between Experiments and a Semi-Quantal Theory". In: *Theoretical Chemistry Accounts* 116 (2006), pp. 514–523.

[105] M. Pellarin, I. Issa, C. Langlois, M.-A. Lebeault, J. Ramade, J. Lermé, M. Broyer, and E. Cottancin. "Plasmon Spectroscopy and Chemical Structure of Small Bimetallic $Cu_{(1-x)}Ag_x$ Clusters". In: *The Journal of Physical Chemistry C* 119 (2015), pp. 5002–5012.

[106] D. Faken and H. Jónsson. "Systematic analysis of local atomic structure combined with 3D computer graphics". In: *Comput. Mater. Sci.* 2 (1994), p. 279.

[107] G. Rossi and R. Ferrando. "Searching for low-energy structures of nanoparticles: a comparison of different methods and algorithms". In: *J. Phys. Cond. Mat.* 21 (2009), p. 084208.

[108] G. Rossi and R. Ferrando. "Combining shape-changing with exchange moves in the optimization of nanoalloys". In: *Computational and Theoretical Chemistry* 1107 (2017), pp. 66–73.

[109] D. Nelli and R. Ferrando. "Core-shell vs. multi-shell formation in nanoalloy evolution from disordered configurations". In: *Nanoscale* 11 (2019), pp. 13040–13050.

[110] M. Settem. "Novel structural motifs: Chiral AgCu nanoalloys with chiral Cu core". In: *Journal of Alloys and Compounds* 844 (2020), p. 155816.

[111] M. Settem and A. K. Kanjarla. "On the nature of the structural transitions between anti-Mackay stacking, chiral stacking and their thermal stability in AgCu nanoalloys". In: *Computational Materials Science* 184 (2020), p. 109822.

[112] G. Rossi, A. Rapallo, C. Mottet, A. Fortunelli, F. Baletto, and R. Ferrando. "Magic Polyicosahedral Core-Shell Clusters". In: *Phys. Rev. Lett.* 93 (2004), p. 105503.

[113] C. Langlois, Z. Y. Li, J. Yuan, D. Alloyeau, J. Nelayah, D. Bochicchio, R. Ferrando, and C. Ricolleau. "Transition from core-shell to Janus chemical configuration for bimetallic nanoparticles". In: *Nanoscale* 4 (2012), pp. 3381–3388.

[114] R. Ferrando. "Symmetry breaking and morphological instabilities in core-shell metallic nanoparticles". In: *J. Phys. Condens. Matter* 27 (2015), p. 013003.

[115] M. Pellarin, M. Broyer, J. Lermé, M.-A. Lebeault, J. Ramade, and E. Cottancin. "Plasmon resonances tailored by Fano profiles in silver-based core–shell nanoparticles". In: *Phys. Chem. Chem. Phys.* 18 (2016), pp. 4121–4133.

[116] M. Sharma, R. Buchner, W. Scharmach, V. Papavassiliou, and M. Swihart. "Creating Conductive Copper–Silver Bimetallic Nanostructured Coatings Using a High Temperature Reducing Jet Aerosol Reactor". In: *Aerosol Science and Technology* 47 (2013), pp. 858–866.

[117] M. Taner Camci, N. Sayar Atasoy, I. Yulug, and S. Suzer. "Synthesis, characterization and antibacterial investigation of silver–copper nanoalloys". In: *J. Mater. Chem.* 21 (2011), pp. 13150–13154.

[118] S. Piccinin, S. Zafeiratos, C. Stampfl, T. W. Hansen, M. Hävecker, D. Teschner, V. I. Bukhtiyarov, F. Girgsdies, A. Knop-Gericke, R. Schlögl, and M. Scheffler. "Alloy Catalyst in a Reactive Environment: The Example of Ag-Cu Particles for Ethylene Epoxidation". In: *Phys. Rev. Lett.* 104 (2010), p. 035503.

[119] N. Bahremandi Tolou, M. Fathi, A. Monshi, V. Mortazavi, and F. Shirani. "Preparation and corrosion behavior evaluation of amalgam/titania nano composite". In: *Dental research journal* 8 (2011), S43–S50.

[120] D. Bansal, J. Sekhon, and S. Verma. "Scattering Efficiency and LSPR Tunability of Bimetallic Ag, Au, and Cu Nanoparticles". In: *Plasmonics* (2013), pp. 143–150.

[121] S. Nunez and R. L. Johnston. "Structures and Chemical Ordering of Small Cu-Ag Clusters". In: *J. Phys. Chem. C* 114 (2010), pp. 13255–13266.

[122] J. P. K. Doye and F. Calvo. "Entropic Effects on the Size Dependence of Cluster Structure". In: *Phys. Rev. Lett.* 86 (2001), pp. 3570–3573.

[123] Nelli, Diana. "Central vacancy creation in icosahedral nanoparticles induced by the displacement of large impurities". In: *Eur. Phys. J. Appl. Phys.* 97 (2022), p. 18.

[124] M. Settem, R. Ferrando, and A. Giacomello. "Tempering of Au nanoclusters: capturing the temperature-dependent competition among structural motifs". In: *Nanoscale* 14 (2022), pp. 939–952.

[125] D. Rapetti, C. Roncaglia, and R. Ferrando. "Optimizing the Shape and Chemical Ordering of Nanoalloys with Specialized Walkers". In: *Advanced Theory and Simulations* 6 (2023), p. 2300268.

[126] M. S. Jørgensen, U. F. Larsen, K. W. Jacobsen, and B. Hammer. "Exploration versus Exploitation in Global Atomistic Structure Optimization". In: *The Journal of Physical Chemistry A* 122 (2018), pp. 1504–1509.

[127] M. Iwamatsu and Y. Okabe. "Basin hopping with occasional jumping". In: *Chem. Phys. Lett.* 389 (2004), pp. 396–400.

[128] D. J. Wales. "Surveying a complex potential energy landscape: Overcoming broken ergodicity using basin-sampling". In: *Chemical Physics Letters* 584 (2013), pp. 1–9.

[129] C.-A. Roth, T. Dreyfus, C. H. Robert, and F. Cazals. “Hybridizing rapidly exploring random trees and basin hopping yields an improved exploration of energy landscapes”. In: *Journal of Computational Chemistry* 37 (2016), pp. 739–752.

[130] S. Yang and G. M. Day. “Exploration and Optimization in Crystal Structure Prediction: Combining Basin Hopping with Quasi-Random Sampling”. In: *Journal of Chemical Theory and Computation* 17 (2021), pp. 1988–1999.

[131] M. Goodridge, J. Moriarty, J. Vogrinc, and A. Zocca. “Hopping between distant basins”. In: *Journal of Global Optimization* 84 (2022), pp. 465–489.

[132] M. N. Bauer, M. I. J. Probert, and C. Panosetti. “Systematic Comparison of Genetic Algorithm and Basin Hopping Approaches to the Global Optimization of Si(111) Surface Reconstructions”. In: *The Journal of Physical Chemistry A* 126 (2022), pp. 3043–3056.

[133] F. H. Stillinger and T. A. Weber. “Hidden structure in liquids”. In: *Phys. Rev. A* 25 (1982), p. 978.

[134] F. H. Stillinger and T. A. Weber. “Packing structures and transitions in liquids and solids.” In: *Science* 225 (1984), pp. 983–989.

[135] F. H. Stillinger. “Exponential multiplicity of inherent structures”. In: *Phys. Rev. E* 59 (1999), p. 48.

[136] J. Jellinek and E. B. Krissinel. “Ni_nAl_m alloy clusters: analysis of structural forms and their energy ordering”. In: *Chem. Phys. Lett.* 258 (1996), pp. 283–292.

[137] E. B. Krissinel and J. Jellinek. “13-atom Ni-Al alloy clusters: Structures and dynamics”. In: *Int. J. Quantum Chem.* 62 (1997), pp. 185–197.

[138] C. Langlois, D. Alloyeau, Y. Le Bouar, A. Loiseau, T. Oikawa, C. Mottet, and C. Ricolleau. “Growth and structural properties of CuAg and CoPt bimetallic nanoparticles”. In: *Faraday Disc.* 138 (2008), pp. 375–391.

[139] T. Momin and A. Bhowmick. “Nanoscale alloying: A study in free Cu–Ag bimetallic clusters”. In: *J. Alloy Compounds* 559 (2013), pp. 24–33.

[140] M. Tchaplyguine, T. Andersson, C. Zhang, and O. Björneholm. “Core-shell structure disclosed in self-assembled Cu-Ag nanoalloy particles”. In: *J. Chem. Phys.* 138 (2013), p. 104303.

[141] X. Wu, F. Chen, Y. Jin, N. Zhang, and R. L. Johnston. “Silver–Copper Nanoalloy Catalyst Layer for Bifunctional Air Electrodes in Alkaline Media”. In: *ACS Applied Materials & Interfaces* 7 (2015), pp. 17782–17791.

[142] X. Gao, C. Zou, H. Zhou, C. Yuan, J. He, and X. Luo. “Enhanced nonlinear optical properties of alloyed AgCu glassy nanoparticles”. In: *Journal of Alloys and Compounds* 819 (2020), p. 153003.

[143] L. Yang, L. Chen, Y.-C. Chen, L. Kang, J. Yu, Y. Wang, C. Lu, T. Mashimo, A. Yoshiasa, and C.-H. Lin. “Homogeneously alloyed nanoparticles of immiscible Ag–Cu with ultrahigh antibacterial activity”. In: *Colloids and Surfaces B: Biointerfaces* 180 (2019), pp. 466–472.

[144] A. Rapallo, G. Rossi, R. Ferrando, A. Fortunelli, B. C. Curley, L. D. Lloyd, G. M. Tarbuck, and R. L. Johnston. “Global optimization of bimetallic cluster structures. I. Size-mismatched Ag-Cu, Ag-Ni, and Au-Cu systems”. In: *J. Chem. Phys.* 122 (2005), p. 194308.

[145] G. Barcaro, L. Sementa, and A. Fortunelli. "A grouping approach to homotop global optimization in alloy nanoparticles". In: *Phys. Chem. Chem. Phys* 16 (2014), pp. 24256–24265.

[146] D. Fioravanti, G. Barcaro, and A. Fortunelli. "An augmented (multi-descriptor) grouping algorithm to optimize chemical ordering in nanoalloys". In: *Phys. Chem. Chem. Phys.* 23 (2021), pp. 23075–23089.

[147] L. D. Marks. "Experimental studies of small-particle structures". In: *Rep. Prog. Phys.* 57 (1994), pp. 603–649.

[148] K. Laasonen, E. Panizon, D. Bochicchio, and R. Ferrando. "Competition between Icosahedral Motifs in AgCu, AgNi, and AgCo Nanoalloys: A Combined Atomistic-DFT Study". In: *J. Phys. Chem. C* 117 (2013), pp. 26405–26413.

[149] C. J. Heard and R. L. Johnston. "A density functional global optimisation study of neutral 8-atom Cu-Ag and Cu-Au clusters". In: *The European Physical Journal D* 67 (2013), p. 34.

[150] M. Molayem, V. G. Grigoryan, and M. Springborg. "Global Minimum Structures and Magic Clusters of Cu_m Ag_n Nanoalloys". In: *J. Phys. Chem. C* 115 (2011), pp. 22148–22162.

[151] W. Li, L. Ding, K. Wang, W. Wang, and S. Zhang. "A density functional theory study of structural, electronic and optical properties of 9-atom silver–copper clusters". In: *Materials Today Communications* 25 (2020), p. 101248.

[152] F. d. S. Leite, A. C. A. Silva, C. V. Caetano, A. L. P. Silva, and J. d. J. G. Varela Júnior. "A Detailed Theoretical Study of Cu_3Ag_m Bimetallic Clusters". In: *Orbital: The Electronic Journal of Chemistry* 13 (2021), pp. 212–218.

[153] R. Hultgren, P. D. Desai, D. T. Hawkins, M. Gleiser, and K. K. Kelley. *Values of the Thermodynamic Properties of Binary Alloys*. American Society for Metals, Berkeley, 1981.

[154] D. Nelli, C. Roncaglia, and C. Minnai. "Strain engineering in alloy nanoparticles". In: *Advances in Physics: X* 8 (2023), p. 2127330.

[155] C. Goyhenex. "Rationalization of the sub-surface segregation in nanoalloys of weakly miscible metals". In: *Nanoscale* 14 (2022), pp. 16627–16638.

[156] D. Bochicchio and R. Ferrando. "Morphological instability of core-shell metallic nanoparticles". In: *Phys. Rev. B* 87 (2013), p. 165435.

[157] D. Nelli, E. Y. El Koraychy, M. Cerbelaud, B. Crespin, A. Videcoq, A. Giacomello, and R. Ferrando. "Two-Steps Versus One-Step Solidification Pathways of Binary Metallic Nanodroplets". In: *ACS Nano* 17 (2023), pp. 587–596.

[158] C. L. Cleveland, U. Landman, T. G. Schaaff, M. N. Shafigullin, P. W. Stephens, and R. L. Whetten. "Structural Evolution of Smaller Gold Nanocrystals: The Truncated Decahedral Motif". In: *Phys. Rev. Lett.* 79 (1997), pp. 1873–1876.

[159] T. Teranishi, R. Kurita, and M. Miyake. "Shape Control of Pt Nanoparticles". In: *Journal of Inorganic and Organometallic Polymers* 10 (2000), pp. 145–156.

[160] F. Norimatsu, Y. Mizokoshi, K. Mori, T. Mizugaki, K. Ebitani, and K. Kaneda. "Shape- and size-controlled synthesis of tetrahedral Pd nanoparticles using tetranuclear Pd cluster as precursor". In: *Chemistry Letters* 35 (2006), pp. 276–277.

[161] M. Á. Gracia-Pinilla, E. Pérez-Tijerina, J. Antúnez-García, C. Fernández-Navarro, A. Tlahuice-Flores, S. Mejía-Rosales, J. M. Montejano-Carrizales, and M. José-Yacamán. "On the Structure and Properties of Silver Nanoparticles". In: *The Journal of Physical Chemistry C* 112 (2008), pp. 13492–13498.

[162] A.-X. Yin, X.-Q. Min, Y.-W. Zhang, and C.-H. Yan. "Shape-Selective Synthesis and Facet-Dependent Enhanced Electrocatalytic Activity and Durability of Monodisperse Sub-10 nm Pt-Pd Tetrahedrons and Cubes". In: *Journal of the American Chemical Society* 133 (2011), pp. 3816–3819.

[163] Y. Li, J. Petroski, and M. A. El-Sayed. "Activation Energy of the Reaction between Hexacyanoferrate(III) and Thiosulfate Ions Catalyzed by Platinum Nanoparticles". In: *The Journal of Physical Chemistry B* 104 (2000), pp. 10956–10959.

[164] R. Narayanan and M. A. El-Sayed. "Shape-Dependent Catalytic Activity of Platinum Nanoparticles in Colloidal Solution". In: *Nano Letters* 4 (2004), pp. 1343–1348.

[165] C. Burda, X.-B. Chen, R. Narayanan, and M. A. El-Sayed. "Chemistry and properties of nanocrystals of different shapes". In: *Chem. Rev.* 105 (2005), pp. 1025–1102.

[166] H. M. Lu and X. K. Meng. "Theoretical Model to Calculate Catalytic Activation Energies of Platinum Nanoparticles of Different Sizes and Shapes". In: *The Journal of Physical Chemistry C* 114 (2010), pp. 1534–1538.

[167] G. Zheng, E. Carbó-Argibay, E. González-Romero, I. Pastoriza-Santos, and J. Pérez-Juste. "Pd–Au Heteropentamers: Selective Growth of Au on Pd Tetrahedral Nanoparticles with Enhanced Electrocatalytic Activity". In: *Crystal Growth & Design* 20 (2020), pp. 5863–5867.

[168] P. Zheng, D. Paria, H. Wang, M. Li, and I. Barman. "Optical properties of symmetry-breaking tetrahedral nanoparticles". In: *Nanoscale* 12 (2020), pp. 832–842.

[169] M. Tabatabaei, A. Sangar, N. Kazemi-Zanjani, P. Torchio, A. Merlen, and F. Lagugné-Labarthet. "Optical Properties of Silver and Gold Tetrahedral Nanopyramid Arrays Prepared by Nanosphere Lithography". In: *The Journal of Physical Chemistry C* 117 (2013), pp. 14778–14786.

[170] P. Das, T. K. Chini, and J. Pond. "Probing Higher Order Surface Plasmon Modes on Individual Truncated Tetrahedral Gold Nanoparticle Using Cathodoluminescence Imaging and Spectroscopy Combined with FDTD Simulations". In: *The Journal of Physical Chemistry C* 116 (2012), pp. 15610–15619.

[171] J. Li, X. Li, H.-J. Zhai, and L.-S. Wang. "Au_{20}: A Tetrahedral Cluster". In: *Science* 299 (2003), pp. 864–867.

[172] Y. Xia, D. Nelli, R. Ferrando, J. Yuan, and Z. Y. Li. "Shape control of size-selected naked platinum nanocrystals". In: *Nature Communications* 12 (2021), p. 3019.

[173] R. H. Leary and J. P. K. Doye. "Tetrahedral global minimum for the 98-atom Lennard-Jones cluster". In: *Phys. Rev. E* 60 (1999), R6320–R6322.

[174] L. O. Paz-Borbón, T. V. Mortimer-Jones, R. L. Johnston, A. Posada-Amarillas, G. Barcaro, and A. Fortunelli. "Structures and energetics of 98 atom Pd-Pt nanoalloys: potential stability of the Leary tetrahedron for bimetallic nanoparticles". In: *Phys. Chem. Chem. Phys.* 9 (2007), pp. 5202–5208.

[175] A. Bruma, R. Ismail, L. Oliver Paz-Borbón, H. Arslan, G. Barcaro, A. Fortunelli, Z. Y. Li, and R. L. Johnston. "DFT study of the structures and energetics of 98-atom AuPd clusters". In: *Nanoscale* 5 (2013), pp. 646–652.

[176] C. Roncaglia and R. Ferrando. "Tetrahedral Clusters Stabilized by Alloying". In: *The Journal of Physical Chemistry A* 128 (2024), pp. 89–96.

[177] H. Zhang, M. Jin, and Y. Xia. "Enhancing the catalytic and electrocatalytic properties of Pt-based catalysts by forming bimetallic nanocrystals with Pd". In: *Chem. Soc. Rev.* 41 (2012), pp. 8035–8049.

[178] B. Lim, M. Jiang, P. H. C. Camargo, E. C. Cho, J. Tao, X. Lu, Y. Zhu, and Y. Xia. "Pd-Pt Bimetallic Nanodendrites with High Activity for Oxygen Reduction". In: *Science* 324 (2009), pp. 1302–1305.

[179] Z. Peng and H. Yang. "Synthesis and Oxygen Reduction Electrocatalytic Property of Pt-on-Pd Bimetallic Heteronanostructures". In: *Journal of the American Chemical Society* 131 (2009), pp. 7542–7543.

[180] L. Wang, Y. Nemoto, and Y. Yamauchi. "Direct Synthesis of Spatially-Controlled Pt-on-Pd Bimetallic Nanodendrites with Superior Electrocatalytic Activity". In: *Journal of the American Chemical Society* 133 (2011), pp. 9674–9677.

[181] J. P. K. Doye, D. J. Wales, and R. S. Berry. "The effect of the range of the potential on the structures of clusters". In: *J. Chem. Phys.* 103 (1995), p. 4234.

[182] K. Manninen and M. Manninen. "Stacking faults in close-packed clusters". In: *The European Physical Journal D - Atomic, Molecular, Optical and Plasma Physics* 20 (2002), pp. 243–249.

[183] A. D. Clercq, S. Giorgio, and C. Mottet. "Pd surface and Pt subsurface segregation in $Pt_{1-c}Pd_c$ nanoalloys". In: *Journal of Physics: Condensed Matter* 28 (2016), p. 064006.

[184] D. Nelli, C. Roncaglia, S. Ahearn, M. Di Vece, R. Ferrando, and C. Minnai. "Octahedral Growth of PtPd Nanocrystals". In: *Catalysts* 11 (2021).

[185] V. Samsonov, A. Romanov, I. Talyzin, A. Lutsay, D. Zhigunov, and V. Puytov. "Puzzles of Surface Segregation in Binary Pt-Pd Nanoparticles: Molecular Dynamics and Thermodynamic Simulations". In: *Metals* 13 (2023), p. 1269.

[186] J. L. Rousset, A. M. Cadrot, F. J. Cadete Santos Aires, A. Renouprez, P. Mélinon, A. Perez, M. Pelarin, J. L. Vialle, and M. Broyer. "Study of bimetallic Pd-Pt clusters in both free and supported phases". In: *J. Chem. Phys* 102 (1995), pp. 8574–8585.

[187] J. L. Rousset, A. J. Renouprez, and A. M. Cadrot. "Ion-scattering study and Monte Carlo simulations of surface segregation in Pd-Pt nanoclusters obtained by laser vaporization of bulk alloys". In: *Phys. Rev. B* 58 (1998), pp. 2150–2156.

[188] L. Fiermans, R. De Gryse, G. De Doncker, P. A. Jacobs, and J. A. Martens. "Pd Segregation to the Surface of Bimetallic Pt-Pd Particles Supported on H-β Zeolite Evidenced with X-Ray Photoelectron Spectroscopy and Argon Cation Bombardment". In: *Journal of Catalysis* 193 (2000), pp. 108–114.

[189] F. Bernardi, M. C. M. Alves, A. Traverse, D. O. Silva, C. W. Scheeren, J. Dupont, and J. Morais. "Monitoring Atomic Rearrangement in Pt_xPd_{1-x} (x = 1, 0.7, or 0.5) Nanoparticles Driven by Reduction and Sulfidation Processes". In: *The Journal of Physical Chemistry C* 113 (2009), pp. 3909–3916.

[190] G. Rossi, R. Ferrando, A. Rapallo, A. Fortunelli, B. C. Curley, L. D. Lloyd, and R. L. Johnston. “Global optimization of bimetallic cluster structures. I. Size-matched Ag-Pd, Ag-Au, and Pd-Pt systems”. In: *J. Chem. Phys.* 122 (2005), p. 194309.

[191] P. Giannozzi, S. Baroni, N. Bonini, M. Calandra, R. Car, C. Cavazzoni, D. Ceresoli, G. L. Chiarotti, M. Cococcioni, I. Dabo, A. D. Corso, S. de Gironcoli, S. Fabris, G. Fratesi, R. Gebauer, U. Gerstmann, C. Gougoussis, A. Kokalj, M. Lazzeri, L. Martin-Samos, N. Marzari, F. Mauri, R. Mazzarello, S. Paolini, A. Pasquarello, L. Paulatto, C. Sbraccia, S. Scandolo, G. Sclauzero, A. P. Seitsonen, A. Smogunov, P. Umari, and R. M. Wentzcovitch. “QUANTUM ESPRESSO: a modular and open-source software project for quantum simulations of materials”. In: *Journal of Physics: Condensed Matter* 21 (2009), p. 395502.

[192] J. P. Perdew, K. Burke, and M. Ernzerhof. “Generalized gradient approximation made simple”. In: *Phys. Rev. Lett.* 77 (1996), pp. 3865–3868.

[193] H. Brune. “Microscopic view of epitaxial metal growth: nucleation and aggregation”. In: *Surface Science Reports* 31 (1998), pp. 125–229.

[194] X. Wang, S. Zheng, S. Shinzato, Z. Fang, Y. He, L. Zhong, C. Wang, S. Ogata, and S. X. Mao. “Atomistic processes of surface-diffusion-induced abnormal softening in nanoscale metallic crystals”. In: *Nature Communications* 12 (2021), p. 5237.

[195] P. Z. Chen, A. Skirzynska, T. Yuan, O. Voznyy, and F. X. Gu. “Asymmetric Interfacet Adatom Migration as a Mode of Anisotropic Nanocrystal Growth”. In: *Journal of the American Chemical Society* 144 (2022), pp. 19417–19429.

[196] W. Dachraoui, M. I. Bodnarchuk, and R. Erni. “Direct Imaging of the Atomic Mechanisms Governing the Growth and Shape of Bimetallic Pt–Pd Nanocrystals by In Situ Liquid Cell STEM”. In: *ACS Nano* 16 (2022), pp. 14198–14209.

[197] W. Dachraoui, M. I. Bodnarchuk, A. Vogel, M. V. Kovalenko, and R. Erni. “Unraveling the shell growth pathways of Pd-Pt core-shell nanocubes at atomic level by in situ liquid cell electron microscopy”. In: *Applied Physics Reviews* 8 (2021), p. 041407.

[198] K. A. Fichthorn and T. Yan. “Shapes and Shape Transformations of Solution-Phase Metal Particles in the Sub-nanometer to Nanometer Size Range: Progress and Challenges”. In: *The Journal of Physical Chemistry C* 125 (2021), pp. 3668–3679.

[199] S. F. Tan, S. W. Chee, G. Lin, M. Bosman, M. Lin, U. Mirsaidov, and C. A. Nijhuis. “Real-Time Imaging of the Formation of Au–Ag Core–Shell Nanoparticles”. In: *Journal of the American Chemical Society* 138 (2016), pp. 5190–5193.

[200] N. Ahmad, M. Bon, D. Passerone, and R. Erni. “Template-Assisted in Situ Synthesis of Ag@Au Bimetallic Nanostructures Employing Liquid-Phase Transmission Electron Microscopy”. In: *ACS Nano* 13 (2019), pp. 13333–13342.

[201] W. Gao, A. O. Elnabawy, Z. D. Hood, Y. Shi, X. Wang, L. T. Roling, X. Pan, M. Mavrikakis, Y. Xia, and M. Chi. “Atomistic insights into the nucleation and growth of platinum on palladium nanocrystals”. In: *Nature Communications* 12 (2021), p. 3215.

[202] J. Wu, W. Gao, J. Wen, D. J. Miller, P. Lu, J.-M. Zuo, and H. Yang. “Growth of Au on Pt Icosahedral Nanoparticles Revealed by Low-Dose In Situ TEM”. In: *Nano Letters* 15 (2015), pp. 2711–2715.

[203] Q. Zhang, J. Xie, J. Yang, and J. Y. Lee. "Monodisperse Icosahedral Ag, Au, and Pd Nanoparticles: Size Control Strategy and Superlattice Formation". In: *ACS Nano* 3 (2009), pp. 139–148.

[204] H. Wang, S. Zhou, K. D. Gilroy, Z. Cai, and Y. Xia. "Icosahedral nanocrystals of noble metals: Synthesis and applications". In: *Nano Today* 15 (2017), pp. 121–144.

[205] A. Pimpinelli and J. Villain. *Physics of Crystal Growth*. Cambridge University Press, 1998.

[206] T. Ala-Nissila, R. Ferrando, and S. C. Ying. "Collective and single particle diffusion on surfaces". In: *Advances in Physics* 51 (2002), pp. 949–1078.

[207] K. C. Lai, Y. Han, P. Spurgeon, W. Huang, P. A. Thiel, D.-J. Liu, and J. W. Evans. "Reshaping, Intermixing, and Coarsening for Metallic Nanocrystals: Nonequilibrium Statistical Mechanical and Coarse-Grained Modeling". In: *Chemical Reviews* 119 (2019), pp. 6670–6768.

[208] G. Ehrlich and F. Hudda. "Atomic View of Surface Self-Diffusion: Tungsten on Tungsten". In: *J. Chem. Phys* 44 (1966), pp. 1039–1049.

[209] R. L. Schwoebel. "Step motion on crystal surfaces. II". In: *J. Appl. Phys.* 40 (1968), pp. 614–618.

[210] D. Nelli, C. Roncaglia, R. Ferrando, Z. Kataya, Y. Garreau, A. Coati, C. Andreazza-Vignolle, and P. Andreazza. "Sudden collective atomic rearrangements trigger the growth of defect-free silver icosahedra". In: *Nanoscale* 15 (2023), pp. 18891–18900.

[211] M. Zinke-Allmang, L. C. Feldman, and M. H. Grabow. "Clustering on surfaces". In: *Surface Science Reports* 16 (1992), pp. 377–463.

[212] J. Penuelas, P. Andreazza, C. Andreazza-Vignolle, C. Mottet, M. De Santis, and H. C. N. Tolentino. "Real-time icosahedral to fcc structure transition during CoPt nanoparticles formation". In: *The European Physical Journal Special Topics* 167 (2009), pp. 19–25.

[213] P. Andreazza, A. Lemoine, A. Coati, D. Nelli, R. Ferrando, Y. Garreau, J. Creuze, and C. Andreazza-Vignolle. "From metastability to equilibrium during the sequential growth of Co–Ag supported clusters: a real-time investigation". In: *Nanoscale* 13 (2021), pp. 6096–6104.

[214] A. Hizi, G. D. Forster, R. Ferrando, Y. Garreau, A. Coati, C. Andreazza-Vignolle, and P. Andreazza. "Combined atomistic simulations to explore metastability and substrate effects in Ag–Co nanoalloy systems". In: *Faraday Discuss.* 242 (2023), pp. 35–51.

[215] R. Ferrando and G. Tréglia. "Step-descent mechanisms on Ag and Au(111)". In: *Surface Science* 377-379 (1997), pp. 843–846.

[216] F. Baletto and R. Ferrando. "Island adsorption and adatom diffusion on 3D non-crystalline silver nanoclusters". In: *Surf. Sci.* 490 (2001), p. 361.

[217] J. P. Perdew, A. Ruzsinszky, G. I. Csonka, O. A. Vydrov, G. E. Scuseria, L. A. Constantin, X. Zhou, and K. Burke. "Restoring the Density-Gradient Expansion for Exchange in Solids and Surfaces". In: *Phys. Rev. Lett.* 100 (2008), p. 136406.

[218] F. Baletto. "Structural properties of sub-nanometer metallic clusters". In: *Journal of Physics: Condensed Matter* 31 (2019), p. 113001.

[219] K. A. Fichthorn. “Theory of Anisotropic Metal Nanostructures”. In: *Chemical Reviews* 123 (2023), pp. 4146–4183.

[220] P. N. Plessow. “The transformation of cuboctahedral to icosahedral nanoparticles: atomic structure and dynamics”. In: *Phys. Chem. Chem. Phys.* 22 (2020), pp. 12939–12945.

[221] E. Telari, A. Tinti, M. Settem, L. Maragliano, R. Ferrando, and A. Giacomello. “Charting Nanocluster Structures via Convolutional Neural Networks”. In: *ACS Nano* 17 (2023), pp. 21287–21296.

[222] J. Q. Goh, J. Akola, and R. Ferrando. “Geometric structure, chemical ordering and electronic properties of large AuCu clusters – A computational study”. In: *J. Phys. Chem. C* 121 (2017), pp. 10809–10816.

[223] R. L. Chantry, I. Atanasov, W. Siriwatcharapiboon, B. P. Khanal, E. R. Zubarev, S. L. Horswell, R. L. Johnston, and Z. Y. Li. “An atomistic view of the interfacial structures of AuRh and AuPd nanorods”. In: *Nanoscale* 5 (2013), pp. 7452–7457.

Appendix A

CNA signatures

In the following table the list of all the 63 different combinations of signatures that was used in Chapter 3 is given.

Table A.1 List of our 63 possible atom classifications. In the first column named "NN" it is written the number of nearest neighbors of the classified atom.

NN	list of signatures	name
14	444 444 444 444 444 444 666 666 666 666 666 666 666 666	inner bcc
14	433 433 433 433 433 433 555 555 555 555 555 555 666 666	disclination polyIh
13	444 444 444 444 444 544 544 544 544 666 666 666 666	bcc subsurface 100
13	433 433 433 433 433 433 555 555 555 555 555 555 666	disclination polyIh end
12	421 421 421 421 421 421 421 421 421 421 421 421	inner fcc
12	421 421 421 421 421 421 422 422 422 422 422 422	inner hcp
12	555 555 555 555 555 555 555 555 555 555 555 555	inner central Ih
12	422 422 422 422 422 422 422 422 422 422 555 555	inner 5-axis
12	422 422 422 422 422 422 433 433 544 544 555 555	subsusrface Ih chiral type 1
12	421 421 421 421 422 422 422 422 433 433 544 544	subsusrface Ih chiral type 2
12	421 421 422 422 422 422 433 433 544 544 555 555	subsusrface Ih chiral type 3
12	300 300 311 311 422 422 433 433 544 544 555 555	central atom rosette without vertex

11	311 311 311 311 421 421 421 421 421 421 421	subsurface 110 & stepB 111 fcc
11	311 311 311 311 421 421 421 422 422 422 422	stepB 111 hcp
11	300 300 300 300 300 422 422 422 422 422 555	around central & noncentral in Ih
11	300 311 311 322 421 421 421 421 422 422 422	around noncentral hole in Ih
11	311 311 311 311 421 421 421 421 421 422 422	around noncentral hole in Ih
11	211 300 300 311 311 421 421 422 422 422 422	around noncentral hole in Ih
11	200 300 300 300 300 322 422 422 422 422 555	around noncentral hole in Ih
11	433 433 433 433 433 555 555 555 555 555 555	missing 5-fold vertex am central atom
10	211 311 311 311 311 421 421 421 421 421	stepA 111 fcc
10	211 311 311 311 311 421 421 421 422 422	stepA 111 hcp
10	322 322 433 433 433 433 444 444 666 666	terrace 110 bcc
10	300 300 311 311 311 311 421 421 422 422	reentrance middle dh
10	311 311 311 311 422 422 422 422 433 433	edge fcc sharp between hcp islands
10	311 311 311 311 433 433 433 433 544 544	edge 111-111 chiral Ih
10	200 200 300 300 322 422 422 422 422 555	around multiholes in Ih
10	200 300 300 311 422 422 422 433 433 555	around multiholes in Ih
10	200 300 300 300 322 322 422 422 422 555	around multiholes in Ih

9	311 311 311 311 311 311 421 421 421	terrace 111 fcc & 0001 hcp
9	211 311 311 322 322 421 421 422 422	terrace hcp 10m11
9	211 211 211 211 444 544 544 544 544	terrace 100 bcc
9	311 311 311 311 322 421 433 433 544	edge 111-111 chiral Ih
9	311 311 322 322 433 433 433 544 555	edge 111-111 chiral Ih
9	322 322 322 433 433 433 555 555 555	polyIh around vertex
9	200 200 200 200 200 200 211 211 211	around multiholes in Ih
8	211 211 211 211 421 421 421 421	terrace 100 fcc
8	200 200 211 311 311 421 422 422	terrace hcp 10m11 & edge anti-Mackay
8	311 311 311 311 322 322 422 422	edge 111-111 twin
8	200 200 322 322 322 422 422 555	edge anti-Mackay close to vertex
8	311 311 311 311 322 322 422 422	edge 111-111 chiral close to vertex
8	322 322 322 322 433 433 444 666	edge 110-110 bcc
8	211 211 211 433 433 444 544 544	edge 110-100 bcc
8	322 322 322 322 433 433 555 555	polyIh side
7	200 200 311 311 311 311 421	edge 111-111 row 110 fcc & 0001_10m11 hcp
7	211 211 211 311 311 421 421	edge 111-100 fcc & 0001_10m11 hcp
7	200 211 211 311 322 421 422	edge 10m11_10m11 hcp
7	200 211 211 311 322 421 422	edge 10m11_10m11 hcp
7	200 200 300 311 311 322 422	missing 5-fold vertex surrounding atoms
7	200 200 211 211 422 422 433	missing 5-fold vertex am surrounding atoms
7	200 200 300 311 311 322 422	vertex 111-111 reentrance dh
7	322 322 322 322 322 322 666	vertex 110-110 bcc wide & vertex rosette
7	211 211 322 433 433 444 544	vertex 110-100 bcc
6	211 211 311 311 311 311	edge 111-111 sharp fcc
6	100 100 211 211 422 422	edge 100-100 twin
6	200 211 211 311 311 421	vertex 111-100 fcc & 0001-10m11 hcp
6	322 322 322 322 322 555	vertex 111-111 5-fold Ih dh
5	322 322 322 322 444	vertex 110-110 bcc sharp
5	100 211 211 322 422	vertex 111-100 twin dh
5	200 200 211 311 311	vertex 111_111 fcc sharp-wide
4	200 200 200 200	vertex 111-111 fcc 4-fold
4	211 211 322 322	vertex 111-111 perimeter dh
3	211 211 211	vertex 111-111 fcc 3-fold

Appendix B

Gupta potential parameters

Table B.1 Parameters of the AgCu interaction potential. From Ref. [99]

	p	q	A (eV)	ξ (eV)	r^0 (Å)	r^c (Å)	r^e (Å)
Ag-Ag	10.85	3.18	0.1031	1.1895	2.89	4.08707719	5.00562683
Cu-Cu	10.55	2.43	0.0894	1.2799	2.56	3.62038672	4.43405007
Ag-Cu	10.70	2.805	0.0977	1.2275	2.725	4.08707719	4.43405007

Table B.2 Parameters of the AuCu interaction potential. From Ref. [222].

	p	q	A (eV)	ξ (eV)	r^0 (Å)	r^c (Å)	r^e (Å)
Au-Au	10.139	4.033	0.210120	1.8200	2.88	4.0729350596345	4.988306325798
Cu-Cu	10.700	2.452	0.088784	1.2785	2.56	3.6203867196751	4.434050067376
Au-Cu	11.590	3.280	0.108500	1.4400	2.72	4.0729350596345	4.434050067376

Table B.3 Parameters of the AuRh interaction potential. From Ref. [223].

	p	q	A (eV)	ξ (eV)	r^0 (Å)	r^c (Å)	r^e (Å)
Au-Au	12.500	3.5500	0.129097	1.522199	2.8843	4.9957541443	5.768600000000
Rh-Rh	18.450	1.8670	0.062891	1.660162	2.6891	6.0130709733	6.586989223995
Au-Rh	9.529	1.7893	0.120341	1.516005	2.7867	6.0130709733	6.586989223995

Table B.4 Parameters of the PtNi interaction potential. From Ref. [44], except for the values of $r^c_{\alpha\beta}$ and $r^e_{\alpha\beta}$, that we increased in order to obtain the same energies of that reference.

	p	q	A (eV)	ξ (eV)	r^0 (Å)	r^c (Å)	r^e (Å)
Pt-Pt	10.6120	4.0040	0.2975	2.6950	2.7746	30	31
Ni-Ni	16.9990	1.1890	0.0376	1.0700	2.4900	30	31
Pt-Ni	13.8055	2.5965	0.1058	1.6980	2.6323	30	31

Table B.5 Parameters of the Au interaction potential. From Ref. [100].

	p	q	A (eV)	ξ (eV)	r^0 (Å)	r^c (Å)	r^e (Å)
Au-Au	10.5300	4.3000	0.2197	1.8550	2.8779	4.07	4.984711

Table B.6 Parameters of the AuPd interaction potential. From Ref. [101].

	p	q	A (eV)	ξ (eV)	r^0 (Å)	r^c (Å)	r^e (Å)
Au-Au	10.1390	4.0330	0.2096	1.8153	2.8840	4.07859	4.99523
Pd-Pd	11.0000	3.7940	0.1715	1.7019	2.7506	3.88999	4.76425
Au-Pd	10.5690	3.9130	0.2764	2.0820	2.8173	4.07859	4.76425

Table B.7 Parameters of the PtPd interaction potential. From Ref. [190].

	p	q	A (eV)	ξ (eV)	r^0 (Å)	r^c (Å)	r^e (Å)
Pt-Pt	10.612	4.004	0.2975	2.695	2.770	3.91737	4.79778
Pd-Pd	10.867	3.742	0.1746	1.718	2.750	3.88909	4.76314
Pt-Pd	10.7395	3.873	0.2361	2.2065	2.760	3.9032	4.78046